The University of Southern Mississippi

The Aquila Digital Community

Development and Utilization of Digital Image Correlation Techniques for the Study of Structural Isomerism Effects on Strain Development in Epoxy Network Glasses

Stephen Robert Heinz
University of Southern Mississippi

Follow this and additional works at: https://aquila.usm.edu/dissertations

Part of the Polymer Chemistry Commons

Recommended Citation

The University of Southern Mississippi

DEVELOPMENT AND UTILIZATION OF DIGITAL IMAGE CORRELATION

TECHNIQUES FOR THE STUDY OF STRUCTURAL ISOMERISM EFFECTS ON

STRAIN DEVELOPMENT IN EPOXY NETWORK GLASSES

by

Stephen Robert Heinz

A Dissertation
Submitted to the Graduate School
of The University of Southern Mississippi
in Partial Fulfillment of the Requirements
for the Degree of Doctor of Philosophy

Approved:

_____
Director

_____

_____

_____

_____

_____

_____
Dean of the Graduate School

December 2011

The University of Southern Mississippi

DEVELOPMENT AND UTILIZATION OF DIGITAL IMAGE CORRELATION

TECHNIQUES FOR THE STUDY OF STRUCTURAL ISOMERISM EFFECTS ON

STRAIN DEVELOPMENT IN EPOXY NETWORK GLASSES

by

Stephen Robert Heinz

Abstract of a Dissertation
Submitted to the Graduate School
of The University of Southern Mississippi
in Partial Fulfillment of the Requirements
for the Degree of Doctor of Philosophy

December 2011

ABSTRACT

DEVELOPMENT AND UTILIZATION OF DIGITAL IMAGE CORRELATION

TECHNIQUES FOR THE STUDY OF STRUCTURAL ISOMERISM EFFECTS ON

STRAIN DEVELOPMENT IN EPOXY NETWORK GLASSES

by Stephen Robert Heinz

December 2011

The specific aim of this dissertation is to present the findings regarding the effects

of molecular structure on macroscopic mechanical performance and strain development

in epoxy networks. Network molecular structure was altered through monomer

isomerism and crosslink density/molecular weight between crosslinks. The use of

structural isomerism provided a pathway for altering mechanical performance while

maintaining identical chemical composition within the network. Isomerism was

investigated primarily by the curing of diglycidyl ether of bisphenol A (DGEBA) using

either the para- or meta-substituted derivatives of diaminodiphenyl sulfone (DDS).

Additional insights into isomerism were gained through the investigation of networks

composed of either para- or meta-triglycidyl aminophenol (TGAP) cured with 3,3'- or

4,4'-DDS. Crosslink density of the network was varied through two different methods:

(a) increasing the equivalent weight of the linear DGEBA epoxy resin and (b) increasing

the functionality of the epoxy resin through the use of TGAP.

The effects of molecular structure on mechanical properties and strain

development were monitored using a relatively new strain measurement technique known

as digital image correlation (DIC). Strain measurement via DIC was particularly useful

for the development of strain recovery procedures, which provided key insights to the

deformation of epoxy network glasses of varying molecular structure by providing full field analysis of the epoxy specimens.

Specific findings of this research revealed that network isomerism plays an important role in the deformation of epoxy network glasses. Networks containing meta-substituted monomers possessed higher modulus and yield stress values and lower yield strains. On the contrary, networks with para-substituted monomers displayed lower modulus and yield stress values, but increased ability to store energy through anelastic strain mechanisms, thereby delaying the onset of yielding. The increased energy storage of these networks was related to sub-Tg molecular motions and the ability for para-substituted phenyl rings to rotate along an axis of symmetry, thus creating more cooperative motion within the network. Insights into post-yield deformation of epoxy glasses were also gained where networks with meta-substitution were able to dissipate more stress post-yield through large segmental rearrangements.

DEDICATION

This dissertation is dedicated to my family for their endless support and encouragement.

For everyone, I am truly grateful.

ACKNOWLEDGMENTS

TABLE OF CONTENTS

CHAPTER

Research Motives
Background
Research Preview
References

Matrix Formulation
Testing and Analysis
Digital Image Correlation
References

Introduction
Tensile
Compression
Strain Recovery with DIC
Conclusions
References

Introduction
Results
Conclusions
References

LIST OF ILLUSTRATIONS

x

LIST OF TABLES

CHAPTER I

INTRODUCTION

Research Motives

The proliferation of composite materials in aerospace structures has led to a renewed interest in thermoset epoxy polymers. Amorphous epoxy glasses are often used as the polymeric matrix for transferring loads into the carbon fiber reinforcement, providing composites with excellent strength and stiffness with drastic weight reductions over metals. Epoxy matrices possess great advantages over other polymers due to their balance of excellent modulus, strength, thermal capacity, solvent resistance, etc., while maintaining affordability. However, epoxy resins are inherently brittle and often require the use of a second phase toughening agent in composite applications. Improvements in the ability of epoxy matrices to deform without brittle failure would result in increased composite performance.

Over the last decade advancements in computational chemistry have led to renewed interest in structure-property relationships as materials can be rapidly screened for performance based properties. Where previously new chemistries had to be synthesized to determine performance, a process that could take months to years, now numerous variations can be explored with predicted performance determined in a matter of hours or days. One of the leaders in screening composite matrix materials with computational techniques is the Boeing Co. who has invested significant time and efforts into the development of protocols for prediction of molecular level architectural changes on macro-scale performance. Successful implementation of these predictive techniques will allow for rapid analysis of different chemistries and drastically reduce the time and cost for implementing new materials into composite structures.

Carbon fiber based composites designed for aerospace applications will face extreme environments during a service life that is expected to last for decades. Therefore, a plethora of properties must be considered for screening of polymer matrices. An optimum material will possess the following properties:

- Superior mechanical performance through high modulus and excellent strength;

- Maintenance of mechanical properties over a vast temperature range;

- High resistance to small organic penetrants (i.e., solvents, oils, and water)

- Low amounts of creep;

- Excellent fatigue life (i.e., no ratcheting); and

- Little to no aging/degradation (UV and thermal).

Prediction of all of the above properties proves difficult. However, epoxy materials inherently possess many of these traits, leaving prediction of ultimate performance as the main focus of computational prediction. Boeing engineers have developed a failure prediction theory known as Onset Theory (formerly known as SIFT, Strain Invariant Failure Theory), which focuses on the prediction of the critical strain values associated with the onset of composite failure. This failure theory focuses on the prediction of both matrix critical and fiber critical strain invariants. Failure initiates when one component (either fiber or matrix) reaches the critical value at some point during a deformation event. The matrix critical invariants are associated with the dilational and distortional critical values and can be predicted for different materials using molecular dynamic simulation techniques.

With the success of these simulation techniques, numerous promising formulations have been developed. However, the use of MD techniques requires human

interaction through selection of thermoset monomers and the building of matrix structures. A better understanding of how molecular structure affects ultimate composite performance will increase efficiency of modeling programs by allowing for a more educated approach to monomer selection. The focus of efforts in the Wiggins Research Group has been to gain a better understanding of structure-property relationships of epoxy network glasses. The specific aim of this dissertation is to present the findings regarding the effects of molecular structure on macroscopic mechanical performance and strain development in epoxy networks.

<div align="center">Background</div>

Understanding Composite Failure

By definition, composite materials are engineered materials made from two or more constituents that posses significantly different physical or chemical properties. It is due to these significantly different properties that composite specimens are difficult to model as they can fail from numerous mechanisms. Currently, most failure theories are formulated for homogeneous isotropic solids, such as metals, which typically fail in a single manner. These theories are difficult to apply to fiber reinforced polymer composites due to their heterogeneous nature.[1,2]

Examples of modes of composite failure include fiber breakage, fiber pullout, inter-ply delamination, matrix cracking, fiber-matrix de-bonding, etc. In order to simplify these complexities, composite failure can be broken up into two distinct categories of fiber failure and matrix failure, each of which can be defined by specific failure events. Fiber failure can occur in three ways: (a) brittle fracture due to the tension; (b) shear failure due to compression; and (c) by a stress concentration when the matrix failure eliminates the pathway for load transfer between neighboring fibers.[2]

Matrix failure can occur from (a) dilatational and (b) distortional deformation mechanisms.

Matrix resins are exposed to a multi-axial stress state within a composite due to orientation of the fibers. Fibers arrange in a random nature, but for the purpose of multi-scale models, are often represented in simple form. Two common packing arrangements for fibers within a unidirectional composite are the square and hexagonal arrays depicted in Figure 1. These simple representations are used to illustrate the distribution of fibers and resin within the composite in order to provide a basis for prediction of composite performance.[3,4]
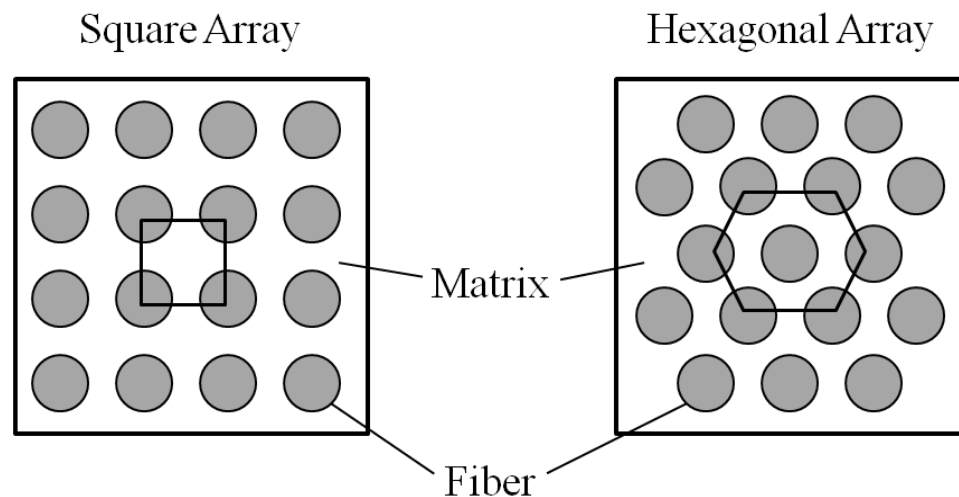
Figure 1. Simple representation of fiber arrangements in a unidirectional composite.

Based on the packing arrangements depicted above, micromechanical models can be used to predict the strain values at various points within a single cell or representative volume element (RVE) of the above array.[5] A single cell is the simplest representation of the infinite periodic arrangement of the inhomogeneous composite material.[1] Figure 2 shows a single cell from the square array, where 20 critical positions have been labeled. Positions F1-8 represent the fiber at the fiber-matrix interface, while M1-8 represent the

matrix at the fiber-matrix interface. F9 represents the center of the fiber with IF1-2 and

IS representing the matrix at the inter-fiber and interstitial positions. The inter-fiber

position is located between fibers in their closest point, and the interstitial position is in

between fibers where they are furthest from one another. During mircro-mechanics

simulations, the local strain at each of these positions is monitored, and failure is

predicted to occur when one of these points reaches a critical strain value.
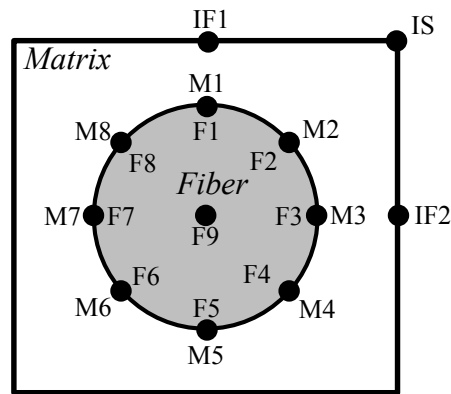
Figure 2. RVE of a polymer matrix composite.

The square array representation is only a partial representation of the complexity

of modeling composite failure. Hexagonal, diamond, and random arrays must also be

considered along with the fiber volume fraction, v_f. All of these factors emphasize the

complex stress and strain state of a polymer matrix composite. The Strain Invariant

Failure Theory (now known as Onset Theory), was developed by researchers at the

Boeing Co. to accurately predict failure through analysis of strain values at the critical

positions within the composite material.[6] SIFT focuses on the prediction of both matrix

critical and fiber critical strain invariants. Failure initiates when one component (either

fiber or matrix) reaches the critical value at some point during a deformation event.

SIFT was developed on the basis that deformation of solids can be decoupled into

two distinct portions: purely volumetric (dilational) and purely deviatoric (distortional).[6]

Depending on the load orientation, the relative amounts of dilational or distortional deformation will vary. Figure 3 shows a typical failure envelope for a brittle material, such as an epoxy, where the ellipse is truncated in quadrant I to represent failure due to microcavitation or crazing.[7] This representation explains why high-modulus matrix resins used in composites are relatively brittle, leading to failure prior to full utilization of carbon fiber load bearing capabilities.
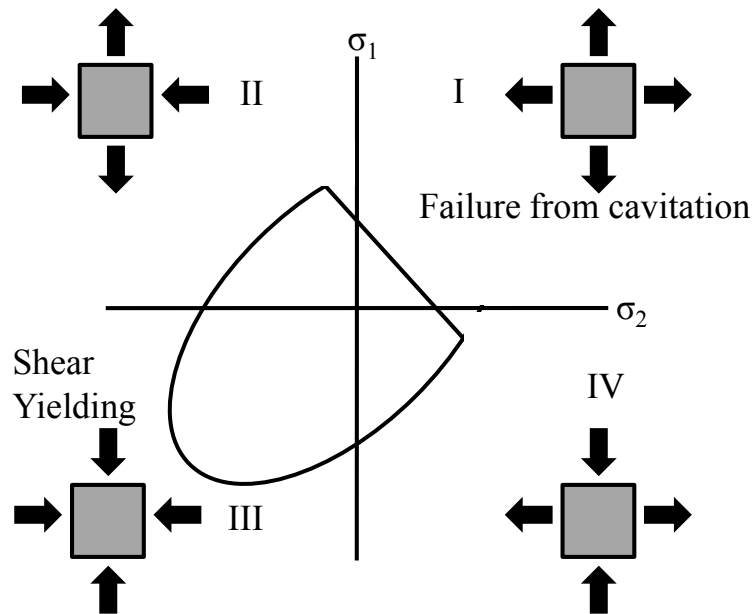
Figure 3. Failure envelope for a brittle material.

According to SIFT, matrix failure initiates when the strain invariant exceeds a dilational or distortional critical value. The volumetric strain invariant, or J_1, is a sum of the three components:

$$J_1 = \varepsilon_{xx} + \varepsilon_{yy} + \varepsilon_{zz} \qquad \text{Equation 1}$$

Failure initiates when J1 exceeds a critical value ($J_{1\text{-crit}}$). The critical deviatoric strain, or distortional strain, is determined based on the von Mises strain, ε_{vm}, which is calculated from the strain deviatoric tensor J_2':

$$\varepsilon_{vm} = \sqrt{3J_2'} = \sqrt{\frac{1}{2}[(\varepsilon_1 - \varepsilon_2)^2 + (\varepsilon_1 - \varepsilon_3)^2 + (\varepsilon_2 - \varepsilon_3)^2]} \qquad \text{Equation 2}$$

Polymer Deformation

Now that the complexity of composite failure has been discussed, polymer deformation can be introduced, focusing primarily on the deformation aspects of polymer network glasses. Polymer glasses behave in a complicated manner, displaying the multiple modes of deformation seen in Figure 4. Initially polymer glasses display a linear viscoelastic response that for short times is governed by the time-independent Hookean linear elasticity[8]:

$$\sigma = E\varepsilon \qquad\qquad\qquad \text{Equation 3}$$

where the relationship between stressv(σ) and strain (ε) is directly related by the modulus (E) of the system. As load increases, the material behavior becomes progressively nonlinear. The nonlinear viscoelastic region is not as easily explained as a time-dependent component must be considered. Following yield, irrecoverable deformation is placed on the material in the form of stress-induced plastic flow. During flow, the stress becomes time-dependent according to Newton's law:

$$\sigma = \eta \frac{d\varepsilon}{dt} \qquad\qquad\qquad \text{Equation 4}$$

where η is the viscosity of the material.[9] Strain softening occurs post-yield, as the force to maintain flow is less than the force required to induce it. Finally, molecular orientation occurs, increasing the material's stress response in what is known as strain hardening.
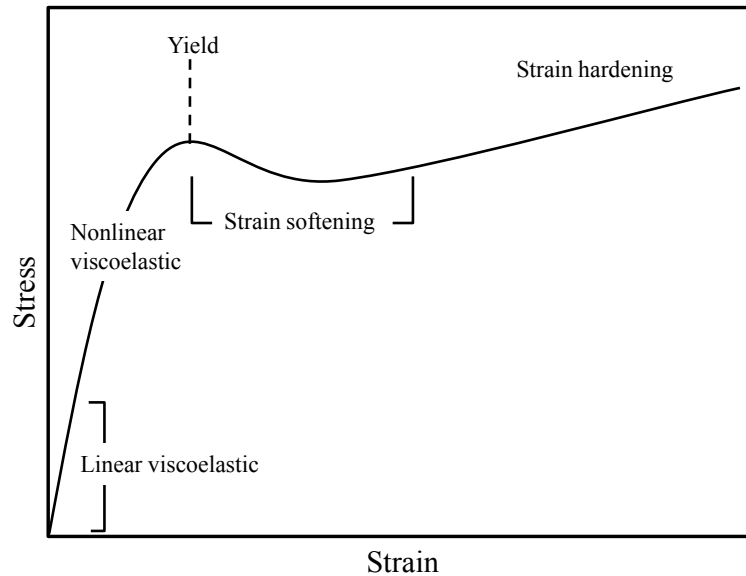
Figure 4. Typical deformation behavior of a polymer glass.

Dilation and distortion. The terms dilation and distortion have been mentioned as the primary modes of deformation/failure in polymer matrices used in composites. Therefore, it is important to discuss the nature of distortional and dilational deformation in more detail. In polymers, dilation occurs when an applied stress causes deformation by a change in critical volume within the material. Dilation occurs due to a lack of chain mobility where the net result is void growth between polymer chains. In some thermoplastic materials a visible craze will form.[10] Figure 5 depicts pure dilation, in which volume expansion occurs without a change in shape of the material. If the volume expansion is small, cohesion will prevail and the material returns to its initial volume. However, if cohesive forces are overcome, nanoscopic cavities and disclinations will form and will eventually coalesce, leading to the onset of crack propagation and catastrophic failure.[11]
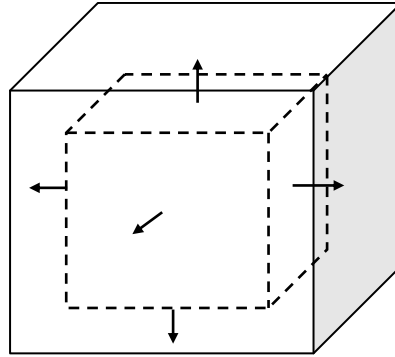
Figure 5. Dilational deformation.

Distortional deformation, depicted in Figure 3, is molecular deformation in which cavitation is avoided by a change in shape without a change in volume. Although intermolecular forces of attraction may be overcome during distortional events, the net result is a molecular rearrangement of the material followed by reforming of the attractive forces that hold the molecules intact. Yielding of a polymer material is a distortional deformation event.
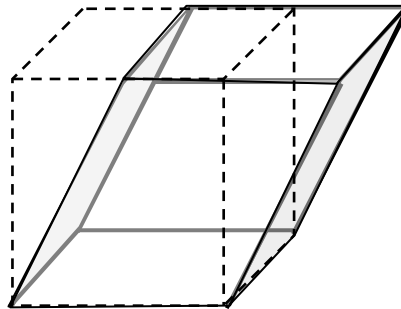
Figure 6. Distortional deformation.

Yield. The polymer matrix provides a medium for transfer of stress to the surrounding fibers. The yielding properties of the resin play an essential role in this process.[12,13] Research to understand this relationship has been conducted by Behzadi et al. in which they have shown that matrix yielding helps offset failure by dissipating stress in regions surrounding broken fibers.[14] Therefore, accurate determination of this point is fundamental in understanding how a composite will react to a high stress event.[12]

However, determination of a specific yield point of a polymer is difficult due to the numerous complexities and factors influencing yield.[15, 16] The term yield is defined as the "onset of plastic deformation" in a material, i.e., exceeding the yield point of a material will result in some sort of permanent deformation.[17] Determination of yield point in metals is relatively simple as permanent plastic deformation is easily associated with a change in slop of the stress-strain curve. However, polymers often do not display a clear yield point (as seen in Figure 4), and even when they do, the specific value of this point can be questioned based on the test method and parameters employed.[15]

Tests used to determine the specific yield point of a material can be conducted in either tension or compression. Yield in tensile deformation is often accompanied by the development of a geometrical instability from which a neck will form.[18] However, not all glassy materials yield in tension due to brittle fracture from material dilation. Brittle fracture occurs in some glassy polymers and most epoxy networks due to the tensile yield stress being greater than the fracture stress.[19] In situations such as these, compression is used for analysis of deformation behavior. In compression, brittle fracture is suppressed (as indicated in the failure envelope of Figure 3), allowing for observation of yielding and subsequent post-yield behavior.[20,21] Compression testing was the primary method for mechanical analysis of epoxy materials in this research.

It has been found that a peak in the stress-strain curve does not always coincide with the onset of plastic deformation. Methods based on the measurement of residual strain on compression specimens unloaded at various points in the stress-strain curve have been employed for determination of yield points of materials. These strain recovery techniques determine the yield point of the material as the onset of residual deformation, which is determined by extrapolation of the residual strain curves back to a value of zero

stress.[22,23,24] Strain recovery techniques are also useful for investigation of the overall strain development in materials, and were a fundamental part of this research.

Deformation theories. Crosslinked epoxy networks can realize relatively high strain values prior to yield and plastic deformation. However, pre-yield deformations of epoxy networks undergo elastic and viscoelastic deformations, making them susceptible to fatigue failures. Since the deformations of amorphous polymer glasses follow nonlinear viscoelastic behavior prior to yield, the prediction of their strain behavior is complicated. Extensive research has been conducted to study the pre- and post-yield nonlinearity of crosslinked polymer glasses. However, a general model that applies to all materials has not been realized.[25,26]

The most commonly known theories of yield are based on the Eyring theory[27] and Argon's double kink theory.[28] These theories were able to successfully predict yield behavior of glassy materials, taking into account the strain rate and temperature dependence of yield. However, these theories were not capable of prediction of the post-yield strain softening and strain hardening of glassy polymers. Therefore, most present approaches to prediction of behavior are based on the work of Haward and Thackray.[29] They proposed the addition of a rubber spring in parallel to a Erying dashpot to represent the time-dependent nature of deformation (Figure 7). This theory has since been the basis for many other constitutive models.[30, 31] However, the success of a predictive model is often tied to a specific material (mostly amorphous thermoplastic glasses) and faces complications when extended to others. A better understanding of the connection between molecular structure and macroscopic deformation is needed to facilitate improved modeling capabilities.[32,33]
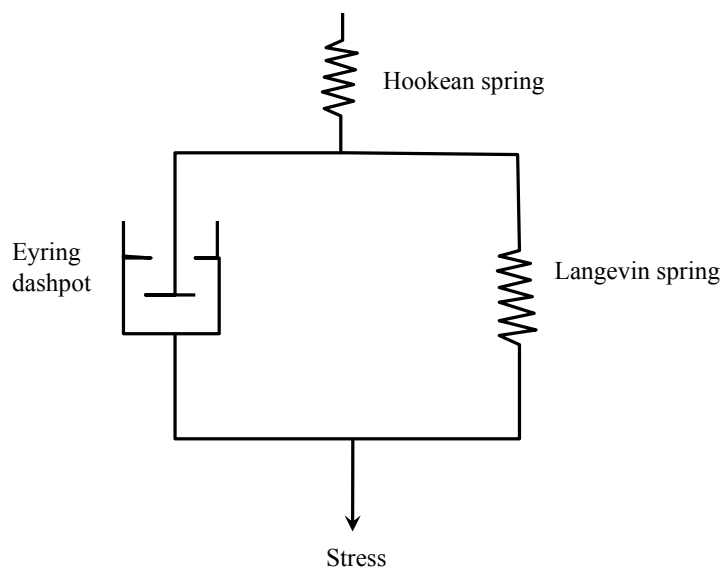
Figure 7. Haward and Thackray based model of strain response to stress.

Connecting Molecular Motions to Deformation

Macroscopic deformation of a material is governed by motions that occur on a significantly smaller scale.[34] Molecular motions of different varieties dominate the performance of a polymer material. Polymers in the glassy state possess some small dynamic motion even in a static environment. As stress builds within a system, the time-scale of these motions is drastically reduced, resulting in cooperative deformation. Eventually, large segmental flow is induced, culminating in yield of the polymer material. Deformation, or strain, on a polymer specimen occurs in three distinct forms: elastic, anelastic, and plastic. These modes of strain development are distinguishable based on their recovery. Elastic strain recovers instantaneously upon removal of load, while anelastic strain has a time-dependent recovery, and plastic strain is irrecoverable at temperatures below the polymer's glass transition point.[35,36,37] Anelastic strain is responsible for the non-linear nature of polymer glasses through the introduction of time-dependent motions. In other words, stress applied to the system accelerates the time-scale of deformation through activation of motion. A Kelvin-Voight model can be used

to explain the recovery of a typical polymer glass. This model is based on the use of springs and dashpots in parallel, as proposed by Haward and Thackray, to represent the time-dependency of anelasic strain.[38] In the Kelvin-Voight model depicted in Figure 8, the elastic, anelastic, and plastic strain components are labeled where multiple parallel springs and dashpots in series represent the multitude of motions associated with polymer deformation.
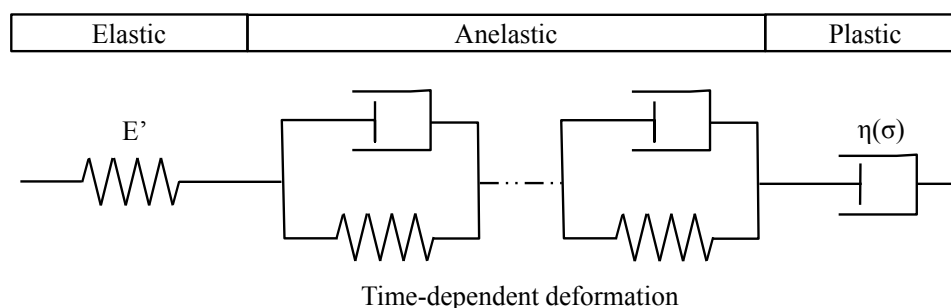
Figure 8. Kelvin-Voight model for nonlinear viscoelasticity

The motions associated with the individual strain components are not completely understood. However, general conclusions about the contributing factors can be made. Elastic strain is associated with the intermolecular interactions between neighboring chains/segments. A material's initial response to an applied load is controlled by the intermolecular attractions arising from Van der Waals forces from nearest neighboring chains.[39] Van der Waals forces are responsible for the attraction between neighboring chains of a material and include Keesom forces, Debye forces, and London dispersion forces, which create instantaneous attractions between molecules.[40,41,42]

Anelastic strain is associated with intramolecular motions of individual segments or groups along the polymer chain. These motions become increasingly available upon exceeding the forces required to break the intermolecular interactions discussed above. Motions associated with anelastic strain include bond rotations, gauche- to trans-

conformation changes, ring rotations, crankshaft motions, etc. Motions such as these are associated with molecular level energy absorption. Anelastic strain has been attributed to the sub-T_g molecular motions for glassy polymer networks,[43] a relationship that will be explored in more detail in a later section.

The development of plastic strain is attributed to long range segmental motion, which occurs once the forces required to induce segmental flow have been overcome. Plastic deformation results from abrupt shear transformations involving multiple degrees of freedom.[44,45] These motions are often associated with those which create the α-transition in polymer materials, revealing that the molecular response of stress induced flow is related to temperature induced flow.

Dynamic mechanical analysis. Investigation of molecular motions in glassy polymers can be conducted through dynamic mechanical analysis (DMA) where the ratio of the loss to storage modulus, or Tan δ, shows transitions associated with thermal activation of molecular motions of a polymer.[38] The primary transition, or α-transition, is associated with the activation of long-range segmental motions within the polymer chains. The temperature at which this transition occurs is very commonly known as the glass transition temperature, or T_g. After this temperature is exceeded, materials are in the rubbery state.[46] Yield of a polymer has been associated with activation of these α-type motions, allowing for chains to flow past one another as a stress/energy dissipation event.

DMA Tan δ curves also show presence of lower temperature, or sub-T_g transitions. It has been shown that pre-yield behavior of glassy polymers, in the form of anelastic strain, is governed by motions associated with these sub-T_g transitions.[43] The specific molecular motions associated with the sub-T_g transitions of glassy polymers are

not fully understood, but most certainly are associated with phenyl ring flips, ring librations, methylene vibrations, etc.[43,47] Furthermore, it has also been debated as to whether or not the sub-T_g transitions are a response of cooperative motions within the glassy state, with those such as Starkweather declaring that sub-T_g motions involve small segments independent of one another.[48,49] However, it has been shown by various techniques that motion associated with the sub-T_g transition can be facilitated or restricted, thereby indicating that motions can exhibit cooperativity.[50,51]

Epoxy networks possess a large degree of sub-T_g motion and often display two separate transitions. Motions associated with the sub-T_g transitions of epoxy networks have been reported to be associated with phenyl-ring re-orientations within the epoxy[52,53,54] and crankshaft motions of the hydroxylpropyl ether (HPE) groups.[55,56,57] However, solid state NMR and dielectric analysis has revealed that the sub-T_g transition is likely a composite result of both types of motions.[58,59,60] The amount of available motion can be altered through structural changes within the network. This work presents the effects of structure on molecular motions by elimination of the symmetry needed for phenyl ring rotations to occur and by altering the number of HPE segments in the network through changes in crosslink density.

Strain Recovery Analysis. A better understanding of the glassy state deformation of polymers can be obtained by conducting the fore-mentioned strain recovery experiments. While not a common form of material analysis, strain recovery analysis provides particular insights into deformation by allowing for quantification of the individual elastic, anelastic, and plastic strain components.[35,36,37] Research on the strain recovery of amorphous glassy polymers has shown complete anelastic strain recovery occurs at a temperature of approximately 20°C below T_g, and all strain is recovered

above T_g.[23,61,62,63] Most strain recovery research has been conducted on linear amorphous polymer glasses, such as PC, PMMA, and PS, but glassy polymer networks have been reported to behave in a similar manner.[64] This work employed strain recovery techniques to analyze the effects of epoxy network structure on strain development.

Structure-Property Relationships of Epoxy Networks

The main goal of this research was to gain further insights into the relationship of molecular structure and macro-scale mechanical performance and strain development of epoxy networks. These so called structure-property relationships have been studied extensively in polymer glasses for many years. However, interest in structure-property relationships of epoxy networks has been renewed due to the growth of the polymer composites industry where epoxy glasses are placed in structurally demanding applications. A better understanding of how molecular structure affects the mechanical deformation of these materials will lead to better composite design criteria, resulting in improved performance over the lifetime of a structure.

The concepts associated with polymer glass deformation have been reviewed. Now, the modes of network architecture alteration employed in this research will be discussed. The primary focus of this document is to reveal the effects that structural isomerism and crosslink density/molecular weight between crosslinks have on mechanical properties and strain development in epoxy networks. The use of structural isomerism provides a pathway for altering mechanical performance while maintaining identical chemical composition. Isomerism will be investigated while varying the crosslink density through two different methods: (a) increasing the equivalent weight of the linear DGEBA epoxy resin and (b) increasing the functionality of the epoxy resin.

The effects of varying crosslink density on epoxy network properties have been studied extensively. Crosslink density can be modified in multiple ways, including changing monomer functionality,[19,43,65,66] changing monomer molecular weight,[67] changing the stoichiometric ratio,[68,69] or altering the network cure profile.[70,71] Trends that have been shown include increased modulus and yield stress with increased crosslink density.[19,65] It has also been shown that as M_c increases, the T_g of the network decreases, leading to a tougher resin system described as having an "increase in deformability."[67,72] The crosslink density of epoxy networks has also been shown to affect sub-T_g motions with higher crosslink densities, resulting in more cooperativity between neighboring segments.[73]

Network isomerism has been studied to a significantly lower extent, and results are not well documented. In diphenol based epoxies of ortho-, meta-, and para-substitutions, it was shown that the glass transition temperature was highest in the para-substituted network and lowest in the ortho-substituted network.[74] Mobility of the three isomers was studied, indicating the meta-substituted isomer to have the most restricted mobility due to a lower free volume.[75] This work will present findings of the effects of network isomerism on deformation characteristics of epoxy networks through relation of network connectivity to molecular motions.

Digital Image Correlation

In order to gain new insights into glassy network deformation, a relatively new full-field strain analysis technique, known as digital image correlation, was employed for strain analysis in this research. Digital image correlation (DIC), also referred to as photogrammetry, was developed in the early 1980s at the University of South Carolina as a method for the full-field analysis of surface strain. This method is based on the

calculation of surface deformation using a set of digital images from un-deformed and deformed states.[76,77,78] The technique consists of capturing gray-scale images of a random or regular surface pattern using one or two CCD cameras. The surface pattern is typically applied in the form of dark speckles on top of a white/high contrast base, providing patterns that can be easily recognized from image to image. This surface pattern deforms during loading and surface coordinates and deformation is tracked from image-to-image. Upon conclusion of processing, a complete strain map of the specimen surface is obtained.[79,80,81] Originally developed as a 2D technique, measurements utilized a single camera focused directly on the surface of a planar specimen undergoing planar deformation as seen in Figure 9A. This technique is limited by the requirement that the specimen must undergo only planar motion. Out of plane motion and lack of parallel positioning introduces error into the measurement, making 2D digital image correlation impractical to apply to cylinders in uniaxial compression.[79,82] Therefore, a relatively new 3D DIC technique applied to uniaxial compression of glassy polymer cylinders was employed in this research. The three dimensional technique involves the use of two digital CCD cameras. The cameras are placed so the specimen surface is viewed from two different angles (Figure 9B), creating a full field three-dimensional measurement of the specimen shape and displacements.
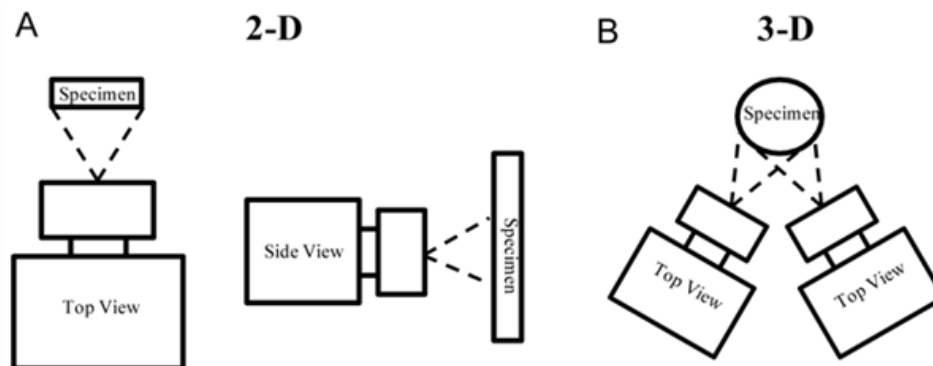
Figure 9. Pictorial representation of 2-D and 3-D digital image correlation.

Use of DIC as an analytical technique has grown rapidly in recent years as hardware and software advancements have improved its viability. A large amount of research has been conducted on tensile behavior of materials using this technique, including the necking behavior of thermoplastics[82,83,84,85,] and failure mechanisms of composite coupons.[86,87] Within this work, DIC techniques were developed and utilized for the analysis of glassy polymer networks. Specifically, techniques were developed for the deformation of epoxy networks to allow for accurate determination of network modulus, yield strain, and Poisson's ratio. Strain recovery analysis was also conducted with DIC, generating data for the complete anelastic strain recovery of the networks, which allowed for direct comparison of recovery rates. The use of DIC also provided a direct perspective for analysis and comparison of strain localization within epoxy networks.

<div align="center">Research Preview</div>

The goals of this dissertation are to reveal the findings on the effects of epoxy network structure on macroscopic mechanical deformation properties. Relationships between network structure and properties will be developed. The relationships will not solely be presented as cause and effect findings, but will be related to molecular motions

of the individual network segments. This work is a niche within a large compass of research in which the effects of network structure are being investigated for a multitude of aspects of composite performance. As research continues, a better understanding of the relationships of molecular scale changes on macroscopic performance will be gained, leading to improved confidence in epoxy matrix selection.

The specific findings of this research are presented in the subsequent chapters with the goals to:

1. Introduce the digital image correlation techniques developed to study the strain behaviors of composite matrices under load.

2. Reveal findings of structural isomerism on mechanical properties and deformation of DGEBA based epoxies cured with 3,3'- or 4,4'-diamnodiphenylsulfone.

3. Investigate the influence of matrix crosslink density and isomerism on mechanical properties and deformation through use of higher equivalent weight DGEBA resins cured with either 3,3'- or 4,4'-diamnodiphenylsulfone.

4. Further study the influence of network isomerism on matrix deformation capability through the investigation of high crosslink density networks based on triglycidyl ether of meta- or para-aminophenol cured with 3,3'- or 4,4'-diaminodiphenylsulfone.

References

1. Tay, T.; Tan, V.B.C.; Liu, G. *Mater. Sci. Eng. B.* **2006,** *132*, 138-142.
2. Hart-Smith, L.J. *AIAA Conf and Exhibi*t. **2001,** *42*, 1-11.
3. Yudhanto, A. Effects of Micromechanical Factors in the Strain Invariant Failure Theory for Composites. Ph.D.Thesis. National University of Singapore, Singapore, 2005.
4. Aboudi, J. *Compos. Sci. Technol.* **1988,** *33,* 79-96.
5. Sun, C.T.; Vaidya. R.S. *Compos. Sci. Technol.* **1996,** *56,* 171-179.
6. Gosse, J.H.; Christensen, S. *AIAA Conf and Exhibit.* **2001,** 1184.
7. Asp, L.E.; Berglund, L.A.; Talreja, R. *Compos. Sci. Technol.* **1996,** *56*, 1291-1301.
8. Ferry, J.D. *Viscoelastic Properties of Polymers,* John Wiley & Sons: New York, 1980.
9. Sperling, L.H. *Introduction to Physical Polymer Science,* Wiley-Interscience: New York, 2001.
10. Sternstein, S.S.; Ongchin, L., *ACS Poly. Prepr.* **1969,** *10,* 1117.
11. Zebarjad, S.M.; Bagheri, R.; Seyed Reihani, M.; Lazzeri, A. *J. Appl. Poly. Sci.* **2003,** *90,* 3767.
12. Behzadi, S.; Jones, F.R. *J. Macromol. Sci. B.* **2005,** *44,* 993-1005.
13. Behzadi, S.; Jones, F.R. *Compos. Sci. Technol.* **2008,** *68,* 2690-2696.
14. Behzadi, S.; Curtis, P.T.; Jones, F.R. *Compos. Sci. Technol.* **2009,** *69,* 2421-2427.
15. Bowden, P.B. In *The Physics of Glassy Polymers.* 2nd ed. Haward. R.N., Eds.; Chapman and Hall: London, 1997; Chapter 5.
16. Marano, C.; Rink, M. *Polymer.* **2001,** *42*, 2113-2119.
17. Young, R.J. Polymer Glasses, Mechanical Properties of: Yielding; In *Encyclopedia of Materials: Science and Technology.* Elsevier: 2001, 7330-7341.
18. Crist, B. In *The Physics of Glassy Polymers.* 2nd ed. Haward. R.N., Eds.; Chapman and Hall: London, 1997; Chapter 4
19. Mayr, A.E.; Cook, W.D.; Edward, G.H. *Polymer*, **1998,** *39,* 3719-3724.
20. Fiedler, B.; Hojo, M.; Ochiai, S.; Schulte, K.; Ando, M. *Compos. Sci. Technol.* **2001,** *61,* 1615-1624.
21. Capaldi, F.M.; Boyce, M.C.; Rutledge, G.C. *Phys. Rev. Lett.,* **2002,** *89*, 1755051-4.
22. Rose, J.; Duckett, R.A.; Ward, I.M. *J. Mater. Sci.* **1995,** *30,* 5328-5334.
23. Quinson, R; Perez, J; Rink, M; Pavan, A. *J. Mater. Sci.* **1996,** *31,* 4387-4394.
24. Quinson, R; Perez, J; Rink, M; Pavan, A. *J. Mater. Sci.* **1997,** *32,* 1371-1379.
25. Perez, J. *Physics and Mechanics of amorphous polymers.* A.A. Balkema, Rotterdam, 1998.
26. Stachurski, Z.H. *Prog. Polym. Sci.* **1997,** *22,* 407-474.
27. Eyring, H. *J. Chem. Phys.* **1936,** *4,* 283-295.
28. Argon, A.S. *Phil. Mag.* **1973,** *28*, 839-865.
29. Haward, R.N.; Thackray, G. *Proc. Roy. Soc. A.* **1968,** *302,* 453-472.
30. Boyce, M.C.; Parks, D.M.; Argon, A.S. *Mech. Mat.* **1988,** *7,* 15-33.
31. Buckley, C.P.; Jones, D.C. *Polymer* **1995,** *36,* 3301-3312.
32. Lee, H.N.; Riggleman, R.A.; de Pablo, J.J.; Ediger, M.D. *Macromolecules* **2009,** *42,* 4328-4336.
33. Schapery, R.A. *Int. J. Solids. Struct.* **2000,** *37,* 359-366.

34. Kabele, P. *Eng. Fract. Mech.* **2007,** *74,* 194-209.

35. Gauthier. C. In *Mechanical properties and testing of polymers: an A-Z reference.* Swallowe, G.M. Ed. Kluwer Academic Publishers: Dordrecht, 1999, p. 191.

36. Pegoretti, A.; Pandini, S.; Ricco. T. *Polymer* **2006**, *47,* 5862-5870.

37. Bendler, J.T.; LeGrand, D.G.; Olszewski, W.V. *Polymer* **2002,** *43,* 389-394.

38. Wunderlich, B. *Thermal Analysis.* Academic Press: San Diego, 1990.

39. Hou, Y.; Bai, X.; Gao, J.; Pang, T. *Heilongjiang Daxue Ziran Kexue Xuebao.* **2002**, *22,* 781.

40. Morrison, R.T.; Boyd, R.N. *Organic Chemistry, 5th ed.* Newton, MA: Allyn and Bacon, Inc, 1987.

41. Brown, T.L., LeMay, H.E., and Bursten, B.E. *Chemistry the Central Science, 6th ed.* Englewood Cliffs, NJ: Prentice Hall, 1994.

42. Atkins, P. and de Paula, J. *Atkin's Physical Chemistry, 8th ed.* New York, NY: W.H. Freeman and Company, 2006.

43. Sindt, O.; Perez, J.; Gerard, J.F. *Polymer,* **1996,** *37,* 2989-2997.

44. Mott, P.; Argon, A.S.; Suter, U. *Philos. Mag.* **1993,** *67,* 931.

45. Chui, C.; Boyce, M.C. *Macromolecules,* **1999,** *32*, 3795-3808.

46. Prime, R.B. In *Thermal Characterization of Polymeric Materials,* Turi, E.A. Ed. Academic Press: New York, 1981.

47. Ochi, M.; Shimbo, M.; Takaskima, N. *J. Polym. Sci.* **1986,** *23,* 2185.

48. Starkweather, H.W.J. *Polymer* **1991,** *32,* 2443.

49. Starkweather, H.W.J. *Macromolecules* **1990,** *23,* 328.

50. Ragosta, G.; Musto, P.; Abbate, M.; Scarinzi. G. *Polymer* **2009,** *50,* 5518-5532.

51. Becker, O.; Varley, R. Simon, G. *Polymer* **2002,** *43,* 4365-4373.

52. Cuddihy, E.F.; Monacanin, J. *J. Polym. Sci. PartA-2,* **1970,** *8,* 1627.

53. Lin, Q.; Yee, A.F.; Sue, H.J.; Earls, J.D.; Hefner Jr, R.E. *J. Polym. Sci. Polym. Phys.* **1997,** *35,* 2363.

54. Garroway, A.N.; Ritchey, W.N.; Moniz, W.B. *Macromolecules,* **1982,** *15,* 1051.

55. Chang, T.D.; Carr, S.H.; Brittain, J.O.; *Polym. Eng. Sci.* **1982,** *22,* 1205.

56. Dammont, F.R.; Kwei, T.K. *Polym. Sci.* **1967,** *5,* 761.

57. Delatycki, O.; Shaw, J.C.; Williams, J.G. *J. Polym. Sci. Part A-2,* **1969,** *7,* 753.

58. Shi, J.F.; Inglefield, P.T.; Jones, A.A. *Macromolecules* **1996,** *29,* 605-609.

59. Heux, L.; Halary, J.L.; Laupretre, F.; Monnerie, L. *Polymer,* **1997,** *38,* 1767-1778.

60. Lee, J.Y.; Song, Y.W.; Kim, S.W.; Lee, H.K. *Mater. Chem. Phys.* **2002,** *77,* 455-460.

61. David, L.; Quinson, R.; Gauthier, C.; Perez, J. *Polym. Eng. Sci.* **1997,** *37,* 1633-1640.

62. Oleinik, E.F.; Rudnev, S.N.; Salamatina, O.B.; Shenogin, S.V.; Kotelyanskii, M.I.; Paramzina, T.V.; Nazarenko, S.I. *e-Polymers* **2006,** no. 029.

63. Kawakami, H.; Yamanaka, H.; Nanzai, Y. *Polymer* **2005,** *46,* 11806-11813.

64. Oleinik, E.F. *Adv. Polym. Sci.* **1986,** *80,* 49-99.

65. Cook, W.D.; Mayr, A.E.; Edward, G.H. *Polymer* **1998,** *39,* 3725-3733.

66. Lesser, A.J.; Calzia, K.J.; *J. Polym. Sci. Pol. Phys.* **2004,** *42,* 2050-2056.

67. Glad, M.D.; Kramer, E.J. *Journal of Materials Science*, **1991,** *26,* 2273-2286.

68. Lin, C.J.; Bell, J.P. *J. Appl. Polym. Sci.* **1972,** *16,* 1721-1733.

69. Murayama, T.; Bell, J.P. *J. Polym. Sci. A2.* **1970,** *8,* 437-445.

70. Meyer, F.; Sanz, G.; Eceiza, A.; Mondragon, I.; Mijovic, J. *Polymer,* **1995,** *36,* 1407-1414.
71. Barton, J.M.; Hamerton, I.; Howlin, B.J.; Jones, J.R.; Liu, S. *Polymer* **1998,** 1929-1937.
72. Lee, J.; Yee, A.F. *Polymer* **2000,** *41*, 8375-8385.
73. Tarasov, V.P.; Smirnov, Y.N.; Yerofeyev, L.N.; Irzhak, V.I.; Rozenberg, B.A. *Polymer Science USSR,* **1983,** *24,* 2732-2736.
74. Yurenko, N.A.; Yevtushenko, G.T.; Yermilova, Y.Y.; Shologon, I.M.; Rozenberg, B.A. *Polymer Science USSR* **1984,** *26,* 2867-2874.
75. Yurechko, N.A.; Yevtushenko, G.T.; Lipskaya, V.A.; Shologon, I.M.; Irzhak, V.I.; Rozenberg, B.A. *Polymer Science USSR,* **1978,** *20,* 2616-2671.
76. Chu, T.C.; Ranson, W.F.; Sutton, M.A.; Peters. W.H. *Exp. Mech.* **1985,** *25,* 232-244.
77. Bruck, H.A.; McNeill, S.R.; Sutton, M.A.; Peters III, W.H. *Exp. Mech.* **1989,** *29,* 261-267.
78. Peters, W.H.; Ranson, W.F. *Opt. Eng.* **1982**, *21,* 427-431.
79. Jin, H.; Lu, W.; Scheffel, S.; Hinnerichs, T.D.; Neilsen, M.K. *Int. J. Solids. Struct.* **2007,** *44,* 6930-6944.
80. Tyson, J.; Schmidt, T.; Galanulis, K. *Exp. Tech. Part I.* **2003,** *27,* 47-50.
81. Tyson, J.; Schmidt, T.; Galanulis, K. Proceedings of SEM 2002 Annual Conference, Milwaukee, WI, June 2002.
82. Grytten, F.; Daivan, H.; Polanco-Loria, M.; Dumoulin, S. *Polym. Test.* **2009,** *28,* 653-660.
83. Jerabek, M.; Major, Z.; Lang, R.W. *Polym Test* **2010,** *29,* 407-416.
84. Parsons, E.; Boyce, M.C.; Parks, D.M. *Polymer* **2004,** *45,* 2665-2684.
85. Parsons, E.M.; Boyce, M.C.; Parks, D.M.; Weinberg, M. *Polymer* **2005,** *46,* 2257-2265.
86. Godara, A.; Raabe, D. *Compos. Sci. Technol.* **2007,** *67*, 2417–2427.
87. Godara, A.; Raabe, D.; Bergmann, I.; Putz, R.; Muller, U. *Compos. Sci. Technol.* **2009,** *69,* 139–146.
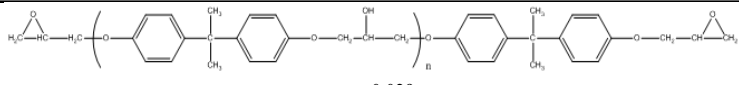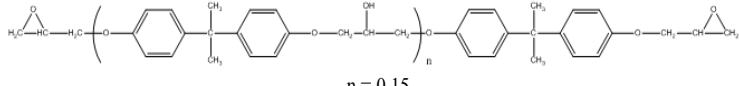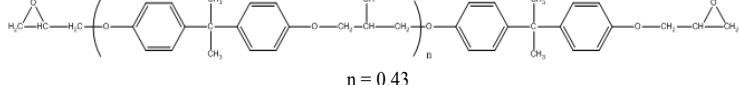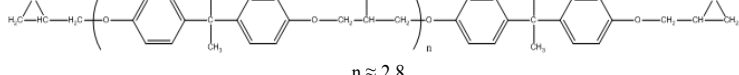
CHAPTER II

EXPERIMENTAL

Matrix Formulation

Materials
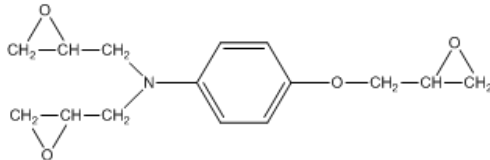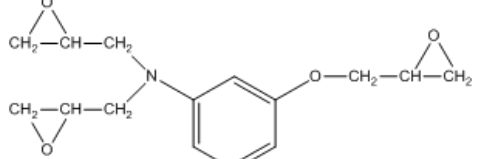
Numerous epoxy-amine systems are investigated throughout this document. Linear difunctional epoxy resins used consist of four differing equivalent weights of diglycidyl ether of Bisphenol A (DGEBA: EW175, EW195, EW245, EW540) acquired from Hexion Specialty Chemicals Co. (recently acquired by Momentive Performance Materials). This research also investigates properties of the tri-functional Araldite MY0510 and MY0610, synthesized from para- or meta-aminophenol. The triglycidyl aminophenol (TGAP) resins were acquired from Huntsman Advanced Materials. Structures, trade names, abbreviations and molecular weights for epoxy resins can be found in Tables 1 and 2.

For this research, epoxy resins were cured with aromatic based amine curatives. The two primary curatives were that of 4,4'-diaminodiphenyl sulfone and 3,3'-diaminodiphenyl sulfone. The structures and weights for these monomers are found in Table 3.
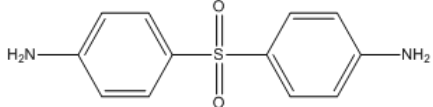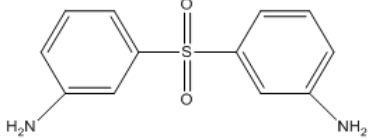
Table 1. Linear Epoxy Resins

Trade name	Structure	Abbreviation	Molecular Weight (g/mol)
Epon 825	n = 0.029	DGEBA/ EW175	350-360
Epon 830	n = 0.15	EW195	380-396
Epon 834	n = 0.43	EW245	460-560
Epon 1001F	n ≈ 2.8	EW540	1050-1100

Table 2. Multifunctional Epoxy Resins

Trade name	Structure	Abbreviation	Molecular Weight (g/mol)
Araldite MY 0510		p-TGAP	285-318
Araldite MY 0610		m-TGAP	285-318

Table 3. Aromatic Amine Curatives

Name	Structure	Abbreviation	Molecular Weight (g/mol)
4,4'-diaminodiphenyl sulfone		4,4'-DDS	248.30
3,3'-diaminodiphenyl sulfone		3,3'-DDS	248.30

Matrix Mixing and Casting

In order to ensure homogeneity throughout the cured network, the epoxy-amine system must be appropriately mixed and b-staged. Epoxy resins range from medium viscosity liquids (DGEBA EW175) to high viscosity liquids (EPON 834), with higher molecular weight systems even being solid (EPON 1001F). Aromatic amine curatives are highly crystalline solids with melting points nearing 200°C. The easiest method for mixing would be to simply add molten amine to a preheated epoxy resin. However, following this method would result in minimal pot-life of the mixed resin system. Epoxy-amine systems, such as DGEBA and 44DDS, begin to react at ~110-120°C. This reaction accelerates to an even more rapid rate as the temperature increases. Therefore, mixing at temperatures above the melting point of 44DDS (~175°C) would not provide adequate time to appropriately cast the resin into molds of the desired final shape. This has led to the development of a mixing procedure that consists of a slow temperature ramp to adequately dissolve the solid amine curative into the liquid epoxy resin.

In a typical reaction, 200.0g (571.4 mmol) DGEBA (EW175) was charged to a 500mℓ Erlenmeyer flask equipped with a vacuum fitting and magnetic stirring device. The epoxy prepolymer was pre-heated to 80°C under vacuum in order to prevent large amounts of air dissolution into the epoxy and to appropriately remove any H_2O that may have been absorbed by the epoxy resin. Vacuum was then removed, and 70.9g (285.7mmol) 4,4'-DDS ground powder was slowly added over a 5-10 minute period to avoid agglomeration. Upon addition, vacuum was slowly applied to a level of ~10^{-3} Torr when the temperature was slowly ramped at 5°C increments toward 120°C. Upon reaching 120°C, the mixture was stirred until complete dissolution of the solid amine was observed. Upon dissolution, stirring was stopped, and vacuum was removed from the

system. The clear, slightly yellowed solution was then poured into preheated (125°C)
molds with the desired specimen shapes.

All networks were developed using formulations that provided a 1:1 ratio of
epoxide:amino-hydrogen. A 1:1 ratio was used in order to ensure the highest conversion
of epoxide groups. Other ratios of functional groups are common in epoxy network
formulations, but the effects of off stoichiometric values are not the scope of this
research.

Cure Schedules

Once cast, the b-staged polymer was cured in a programmable oven with a cure
schedule that depended on the specific network. Linear epoxy systems were typically
cured in two stages, a cure and a postcure. For example, DGEBA and 44DDS systems
were cured for 5h at 125°C and postcured for 1h at 200°C. This type of cure schedule
provides optimum conversion as the cure stage promotes linear growth through the
conversion of mostly primary amines, and the postcure results in final network
development through the conversion of secondary and all remaining primary amines.
Tri-functional epoxy resins were cured by an extended cure schedule in order to avoid
excessive exothermic heat release and subsequent charring. Systems and their respective
cure times can be found in Table 4.

Table 4: Cure Schedules for Differing Resin Systems

Network	Cure	Post Cure
DGEBA (all equivalent weights) / 3,3'- or 4,4'-DDS	5 hours @ 125°C	1 hour @ 200°C
p-TGAP / 3,3'- or 4,4'-DDS	3 hours @ 115°C, 3 hours @ 150°C, 3 hours @ 180°C	1 hour @ 200°C
m-TGAP / 3,3'- or 4,4'-DDS	3 hours @ 115°C, 3 hours @ 150°C, 3 hours @ 180°C	1 hour @ 200°C

Testing and Analysis

Compression Testing

Compression testing procedures followed ASTM 695-02a. Cylinders of 2:1 length to diameter ratios were compressed at a displacement controlled test rate of 0.05in/min (1.27mm/min) on a MTS Systems Corporation Model 810 servo-hydraulic universal test frame equipped with a low friction compression sub-press pictured in Figure 10 (Wyoming Test Fixtures Model CU-SP). Displacement was measured by linear variable differential transformer (LVDT), and load was measured using a MTS 20 kip load cell. Data was recorded at a sampling rate of 10Hz using MTS Testworks® software.
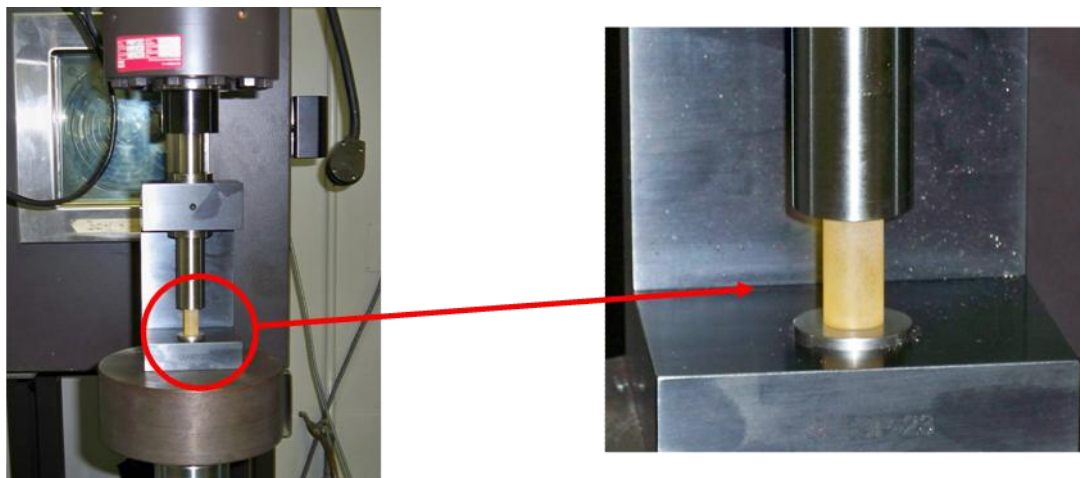
Figure 10. Low-friction compression sub-press.

Tensile Testing

Tensile testing procedures followed ASTM 638-10. Type IV dog bone shaped specimen were cast and cured in thermoset silicone molds. Specimens were deformed at a displacement controlled test rate of 0.05in/min (1.27mm/min) on a MTS Systems Corporation Insight electromechanical universal test frame equipped with mechanical wedge grips. Displacement was measured by linear variable differential transformer (LVDT), and load was measured using a MTS 10kN load cell. Data was recorded at a sampling rate of 10Hz using MTS Testworks® software.

Differential Scanning Calorimetry

Differential scanning calorimetry (DSC) experiments were conducted on a Thermal Analysis (TA) Q200 differential scanning calorimeter. Varying temperature experiments were used in order to determine glass transition temperatures (T_g) of individual resin systems. Glass transition temperatures were determined from the inflection point of the endothermic step transition in heat capacity for a 10°C/min heating ramp. T_g's are reported based on first scan results, negating the effects of thermal history, as thermal history has proved to have a less significant effect on T_g than

subsequent curing that occurs when samples are ramped to temperatures above T_g. The increase in T_g on subsequent scans is used to qualitatively approximate the cure state of the system.

Isothermal DSC was conducted in order to investigate exothermic heat release upon cure. DSC runs were set up to mimic cure conditions. For these tests pans containing b-staged resin were heated to 125°C using the "jump to" command in the TA Q200 control software. Heat capacity was monitored for 5 hours. Following the cure stage, the resin was heated to 200°C, again using the "jump to" command, and exothermic heat release was measured. This procedure allows for qualitative analysis of extent of cure.

DMA Testing

Dynamic mechanical analysis (DMA) experiments were conducted on a Thermal Analysis (TA) Q800 instrument using either a tensile test fixture. A strain amplitude of 0.05%, and a frequency of 1Hz were used. DMA specimens were formed by casting of b-staged resin into silicone molds with rectangular cavities of 5.0mm width by 1.5mm depth and 60.0mm length. A temperature sweep was used to develop E' and Tan δ vs. temperature relationships.

Density Measurement

Density values for epoxy networks were determined using the hydrostatic weighing method, in which the weights of a specimen were recorded in and out of water. The Archimedes principle was then used to calculate density. Particular care was taken in selecting resin specimens as internal voids or bubbles will drastically affect the density values. Density was calculated using the following equation:

$$\rho = \frac{m_{dry}}{m_{dry}-m_{immersed}} * \rho_{water} \qquad \text{Equation 5}$$

where m_{dry} is the mass of the specimen prior to immersion, $m_{immersed}$ is the weight of the specimen in water, and ρ_{water} is the density of water.   The average of 5 is reported.

Positron Annihilation Lifetime Spectroscopy

The positron annihilation lifetime spectroscopy (PALS) experiments were conducted with custom built fast-fast coincidence system having a time resolution of 220 ps. To conduct the measurements [22]Na positron source with radioactivity 30µCi was sandwiched between two 1mm thick sample disks with the diameter 8mm. All the measurements were taken over an hour for a total of $1x10^6$ counts in each PALS spectrum. Temperature measurements were taken by first decreasing the temperature to -30°C and waiting for about two hours to allow for equilibrium before the experiments began. The temperature was then sequentially increased to 200°C in 5°C steps, collecting a spectrum each step, after waiting 15 minutes to allow for equilibrium.

The PALS spectra were tested against three- and four-components fits using the PATFIT software package. Optimal fits were obtained to three components with variances smaller than 1.1. The free volume hole radius, R, was calculated from the o-Ps life time, τ_3, using the semi-empirical equation:

$$\tau = \frac{1}{2}\left[1 - \frac{R}{R+\Delta R} + \frac{1}{2\pi}\sin\left(\frac{2\pi R}{R+\Delta R}\right)\right]^{-1} \qquad \text{Equation 6}$$

where ΔR has been empirically determined to be ΔR=0.1656nm by fitting equation 6 to o-Ps annihilation data for molecular solids of known pore sizes. The hole volume was calculated from

$$V_h = \frac{4}{3}\pi R^3 \qquad \text{Equation 7}$$

Digital Image Correlation

Advanced strain analysis using digital image correlation (DIC) was conducted using a GOM Optical Measuring Techniques ARAMIS 3D Deformation Analysis System (Trilion Quality Systems). DIC requires specimens be "speckle coated" to create a non-uniform surface pattern, which is tracked by the ARAMIS software between digital images captured during the deformation test. Speckle patterns were created on the glassy polymer network cylinder surfaces using white and black aerosol paints. A solid white basecoat was first applied and then followed by a misted black paint, which created black speckles in the size range of 2-5 pixels.[1] A typical speckle pattern and experimental setup for compression cylinders are shown in Figure 11. Digital gray scale images were captured via two 2M digital CCD cameras equipped with 50mm lenses at a frame (capture) rate specific to the deformation event. The CCD cameras possessed a maximum capture rate of 11fps, a speed that is only needed during rapid deformation events. Prior to testing, the capture volume was calibrated using calibration panels provided from the software manufacturer. A wide range of capture volumes can be used; however, for the purpose of this research only calibration volumes of 10mm x 8mm, 15mm x 12mm, 25mm x 20mm, 35mm x 28mm, 55mm x 44mm, and 90mm x 72mm were used. Calibrations were performed to obtain a resolution deviation of less than 0.03 pixels. Digital images were stored for post-test processing and analysis.
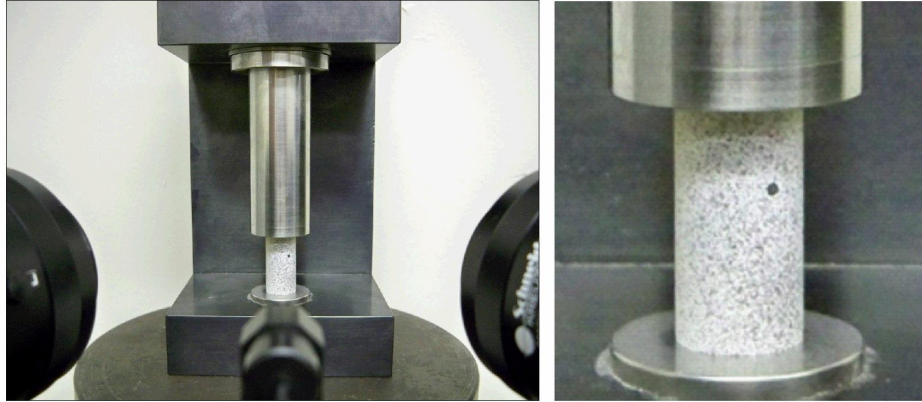
Figure 11. DIC set-up with speckle coated cylinder.

As previously mentioned, DIC allows for the calculation of surface strain through tracking of a non-uniform surface pattern in a series or subset of digital images. The analysis can either be 2-dimensional or 3-dimensional depending on the number of cameras used. 2-D DIC is based on the use of a single camera system and is only capable of measuring motion and shapes that are in the same plane as the camera itself. This unfortunately limits its applicability to many common mechanical tests. Therefore, the current research employs the use of a two camera, 3-D based, DIC system. The use of two cameras allows for the calculation of out of plane deformation, and for the measurement of more complex shapes, such as cylindrical specimens.[2]

Experimental Process

There are numerous steps for preparing and carrying out a digital image correlation experiment:

1. Specimen Preparation;

2. System Calibration;

3. Data Collection;

4. Data Processing; and

5. Data Analysis.

While there is clear distinction between each of the individual processes all steps are interconnected and require extensive planning and execution in order to obtain accurate and reliable data. Each step is discussed at length below.

1. Specimen preparation. Specimens for use in DIC experiments were prepared according to the resin mixing and casting procedures presented above. Once specimens were cured, machined, and inspected for irregularities/defects, non-uniform speckle patterns were applied to the surface of each specimen. The primary method for speckle pattern application consisted of the use of white and black aerosol based paints. Digital images are grayscale; thus, white and black paints provide the most contrast between one another, allowing the software to easily recognize the barrier between speckled and non-speckled regions. The first step in the application process was to apply a solid white base coat to the surface of the specimen that is going to be in view of the cameras. The second step was the application of the black speckles to the already white surface. This is done in a misting fashion in order to obtain speckles with a size range of 2-5 pixels. Pixel size changes depending on the capture volume, requiring the speckle size to change as well. It has been determined that the quality of the speckle pattern is an important influencing factor for the accurate measurement of displacement.[3] Precise control of speckle size is difficult to obtain, especially at smaller size scales. Methods for altering speckle size include fluttering the spray valve, altering the quality or type of paint, or spraying through a porous medium. Upon successful application, the specimen speckle patterns were allowed to dry and were subsequently tested.

2. System calibration. Pre-experimentation procedures also include camera set-up and capture volume calibration. Like the specimen speckle size, camera set-up is highly dependent on the size of the specimen being tested. In order to measure strain on

the entire specimen surface, it is necessary to have the specimen in full view of both cameras and a calibration standard that closely represents the size of the test specimen. For example, compression test specimens typically have a length of 1.00" (25.7mm). In order to have a full field view of the test specimen, a calibration standard with dimensions similar to that of the cylinder was selected (25mm x 20mm standard). Figure 12 shows a typical speckled cylinder and similar sized calibration standard.
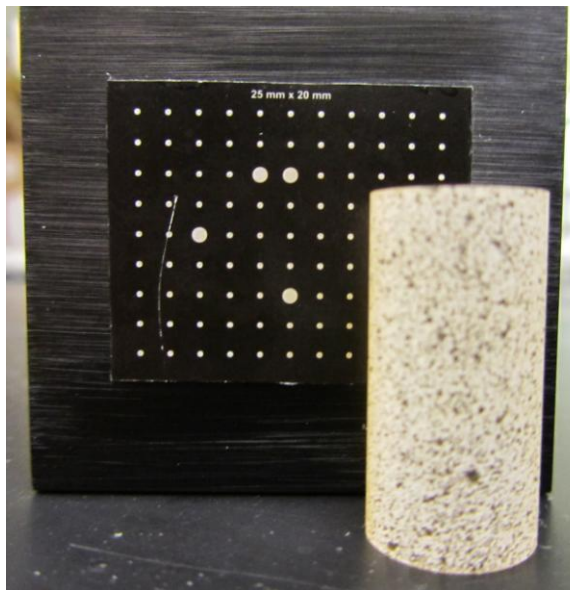
Figure 12. Compression cylinder and similar sized calibration standard.

After appropriate calibration standard selection, the camera span and camera angles were adjusted in order to obtain the optimum measuring distance and appropriate viewing angle. A proper set up is depicted in Figure 13 with the camera span and angle labeled. For accurate data collection, the angle should be approximately 25°. Once positioned correctly, the cameras were focused on the calibration standard. This was best done with a fully opened camera iris at a high shutter speed. Cameras were then focused to provide the maximum amount of overexposure.
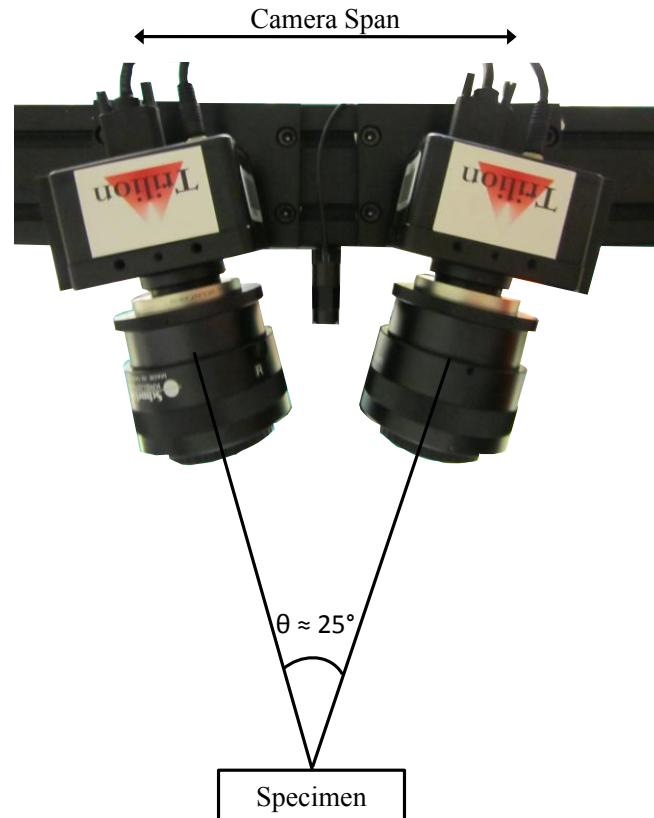
Figure 13. Camera set up with appropriate span and viewing angle.

Calibration was conducted to ensure dimensional consistency of the system. This process was conducted with a reduced camera iris, low shutter speed, and high intensity lighting. The calibration process consisted of collection of a series of images of varying calibration object depths, angles, and rotations. Within each set of images, the computer software locates each landmark on the calibration object and determines its location in 3-dimensional space. Calibration results were accepted based on a calibration deviation between 0.01 and 0.04 pixels.

3. Data collection. Upon completion of the set-up and calibration process, experimental data was collected. The number and frequency of images was dependent on the type of test and the information that was desired. Capture rates ranged from a maximum rate of 11 frames per second to an undefined minimum as delay times between

successive image sets was user defined. Higher image capture rates can be obtained with the use of different camera types. The maximum capture rate of 11fps was sufficient for the types of tests conducted for this dissertation. Images were captured by either a single prescribed rate or through the use of a triggerlist, which can be written to alter the capture rate throughout the duration of the test.

Prior to starting the image capture sequence, the specimen was centered in the capture volume, and final adjustments to the shutter speed and specimen lighting were made. It was important that no over-exposed regions existed as deformation measurements cannot be made in these areas. Finally, before starting the capture sequence, an image set of the unstrained specimen was acquired. This was done by capturing an image set just prior to beginning the loading sequence.

4. Data processing. Post test, stored images are nothing more than sets of grayscale digital pictures. Image sets must be processed in order to obtain deformation data and ultimately surface strain maps. Processing of captured image sets consisted primarily of three steps followed by computer processing during which deformation data was computed. The three essential steps were the definition of a processing area, creation of the facet field, and the assignment of a start point. The purpose of these steps was to increase the accuracy of deformation data while also decreasing the overall computation time. The first step was to define the processing area. The primary goal of this step was to reduce the size of the area to be computed by removing areas of images that did not contain the speckled specimen surface. Facet fields were computer generated and represent the area in which deformation was tracked. Facets, defined by pixel size and step length, were generated in grid patterns across the optimized areas of the digital images. Facet size is the true dimension of the defined area in pixels. Step length is the

distance between adjacent facet centers, with smaller steps leading to increased spatial resolution.[4] Upon facet definition, a start point was defined for the initial image set. The start point provides a reference for the software to recreate the initial facet field on subsequent image sets to quantify three dimensional deformations.[5] It is important to note that start points are not reference points from which deformations/displacements are measured; they are merely user selected arbitrary points that are used by the computer software to recreate the facet field in the appropriate location. Multiple start points are sometimes used in an event that brittle fracture occurs leaving a non-continuous specimen.

In addition to the three steps above, occasionally there was a need to mask image imperfections. Image sections, typically edges that do not display optimum contrast due to shadows or low light artifacts, were eliminated to enhance computational analysis. These steps were sometimes required for analyzing compression specimens as cylindrical surfaces create unique edge effects associated with shadowing and pixel mapping. There were also instances where reflections near instrument fixtures distort the specimen edges at the fixture/specimen interface.

Following data preparation, images were processed using the ARAMIS software. During computer computation the gray scale speckle pattern was tracked within each rectangular facet from image-to-image. A three-dimensional displacement gradient tensor field was calculated based on the change in facet coordinates with respect to the facet center. Using this displacement field, strain tensors were calculated to create strain distribution profiles capable of displaying both major and minor strains of the specimen during loading.[4,6,7]

5. Data analysis. At the completion of processing a visualization of the specimen

surface was displayed. This visualization was used to display numerous values including

displacements, strains, and even calculated quantities, such as Poisson's Ratio. An

example visualization of a cylindrical specimen showing minor strain (a description of

minor strain is included below) is seen in Figure 14 with the origin denoted by the

intersection of green lines and strain scale shown in the legend on the right.
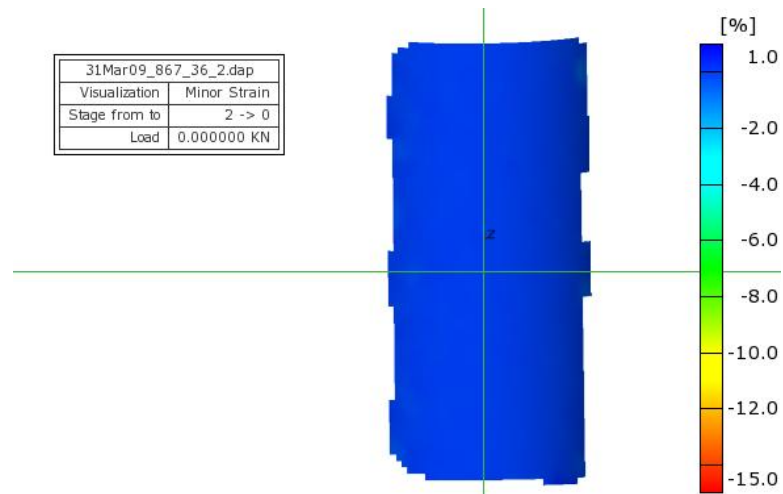
Figure 14. Minor strain map of a cylindrical specimen.

After computation, further corrections were made to improve both accuracy and

visual aesthetics. These corrections included the proper placement of the specimen origin

and orientation of the x- and y-axes.   In some cases, imperfections in specimen speckle

patterns, reflections, or over exposed regions sometimes resulted in an incomplete strain

map. Depending on the size of these defects, the surrounding area can be used to

approximate the numerical value for this absent region. This method of approximation

was especially useful in high strain or long term tests as regions of the speckle pattern

sometimes failed creating holes in the data.

Recall that surface maps, or visualizations, are based solely on displacement

within each individual facet. This creates the ability to display and analyze numerous

quantities. Table 5 displays the quantities that can be generated from DIC data along with a brief description of each.[1] Major and minor strain values were primarily used in this research as they are determined automatically by the computer software independently of the user defined coordinate system. Tensile tests employed the use of major strain while minor strain was used for compression tests as the applied strain is negative.

Table 5. Available Visualizations in the ARAMIS Software.

Visualization	Description
Displacement X	Displacement in the x direction. Dependent on orientation of axes.
Displacement Y	Displacement in the y direction. Dependent on orientation of axes.
Displacement Z	Displacement in the z direction. Dependent on orientation of axes.
Displacement E	Euclidean displacement or displacement from the origin.
Epsilon X	Calculated strain in the x direction. Dependent on orientation of axes.
Epsilon Y	Calculated strain in the y direction. Dependent on orientation of axes.
Epsilon XY	Representation of shear strain on the specimen.
Major Strain	Calculated strain with the directionality determined by the software as the direction of the larger strain.
Minor Strain	Calculated strain with directionality determined by the software as the direction of the smaller strain.

One of the distinct advantages of digital image correlation over traditional strain measurement techniques is the ability to analyze and manipulate data post test. This technique is a full-field technique, meaning that the entire specimen can be analyzed. When deformation is uniform strain can be reported simply by taking the average surface strain of the specimen. However, when deformation is not uniform, several techniques and manipulations can be applied to gain a better understanding of the non-uniformity. Figure 15 highlights two of the most common techniques used to investigate strain

variances in this research. Stage points (labeled as Stage point 1 and Stage point 2) can be applied to a specific location on the specimen surface and are used to track strain at that specific point. Alternatively, strain can be tracked along the length or width of the specimen using section lines. These lines, seen as the black and green lines along the x- and y-axes below, allow the user to observe and plot differences in strain along the length of segment.
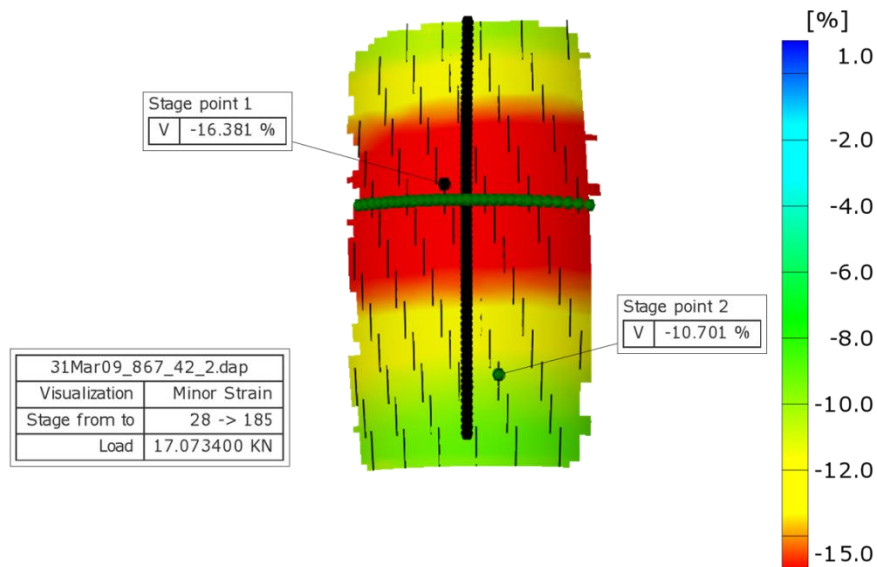
Figure 15. Cylinder strain map showing stage points and section lines on the specimen surface.

REFERENCES

1. ARAMIS User Manual by GOM mbH. April 2007 version. Braunschweig, Germany.
2. Sutton, M.A.; Yan, J.H.; Tiwari, V.; Schreier, H.W.; Orteu, J.J. *Opt. Las. Eng.* **2008,** *46,* 746-757.
3. Hua, T.; Xie, H.; Wang, S.; Hu, Z.; Chen, P.; Zhang, Q. *Opt. Las. Technol.* **2011,** *43,* 9-13.
4. Godara, A.; Raabe, D. *Compos. Sci. Technol.* **2007,** *67,* 2417-2427.
5. Sachs, C.; Fabritius, H.; Raabe, D. *J. Struct. Biol.* **2006,** *155,* 409-425.
6. Parsons, E.; Boyce, M.C.; Parks, D.M. *Polymer* **2004,** *45,* 2665-2684.
7. Godara, A.; Raabe, D.; Bergmann, I.; Putz, R.; Muller, U. Compos. Sci.Technol. **2009,** 69, 139-146.

CHAPTER III

DEVELOPMENT OF DIGITAL IMAGE CORRELATION TECHNIQUES FOR

GLASSY NETWORK ANALYSIS

Introduction

Due to the relatively new nature of digital image correlation, a large amount of

information was learned by the application of DIC techniques to standard mechanical

testing procedures. DIC research has been conducted on various thermoplastic materials

in order to see the strain behavior of materials that display necking phenomena.[1,2,3] Other

research has been conducted to investigate failure of composite structures.[4,5] However,

no research has been conducted to investigate the glassy strain response of cured epoxy

networks. This section discusses the DIC methods developed for analysis of epoxy

glasses in both tensile and compressive loading scenarios. The information obtained,

specifically in compressive loading, provides insights into the strain behavior of these

networks. Further analysis of epoxy networks was conducted through the use of DIC to

measure strain recovery. Strain recovery procedures allowed for quantification of

amounts of elastic, anelastic and plastic strain placed on specimens during loading.

Tensile

Accurate tensile properties are often difficult to obtain for brittle networks as tests

require very precise small strain measurements. This is often hindered by gripping issues

and requires the use of extensometers or strain gauges. The use of DIC for strain

measurement is a non-contact alternative that provides full-field accurate strain

measurement. It is especially more accurate than LVDT measured strain in the small

strain region as the DIC measured strain is independent of grip slippage and machine

slack. This allows for accurate determination of tensile modulus values and Poisson's ratios for polymer networks.

Methods

As previously discussed in Chapter II, tensile testing procedures followed ASTM 638-10. Type IV dog bone shaped specimens were cast and cured in thermoset silicone molds. Appropriately speckled specimens can be seen in Figure 16. The speckled dog bone shaped specimens were deformed at a displacement controlled test rate of 0.05in/min (1.27mm/min) on a MTS Systems Corporation Insight electromechanical universal test frame. Specimens were gripped using 10 kN capacity mechanical wedge grips with serrated inserts. Displacement was measured simultaneously by linear variable differential transformer (LVDT) and DIC. Load was measured using a MTS 10kN load cell at a sampling rate of 10Hz using MTS Testworks® software. Load data was exported and recorded simultaneously within the ARAMIS software using an A/D connection.

Figure 16. Speckled tensile specimens.

The DIC capture volume was calibrated using a 25mm x 20mm calibration object to a deviation of less than 0.03 pixels. Digital image sets were captured using a triggerlist program that included a rapid capture rate for small strain deformation and a slower rate for large strains. The images were captured with the 2M digital cameras using a 50mm lens at a rapid rate of 5fps for the first 200 images. Subsequent images were captured at a rate of 1fps until specimen failure occurred. Load data was imported using an A/D connection and recorded and coupled with each image set. Images were stored and processed post test for complete analysis.

Results

In the case of tensile tests of glassy polymers, deformation is almost always uniform within the gauge section of the specimen. Failure occurs prior to the occurrence of any yielding phenomena, which would create deviation of strain across the length of the specimen. Non-uniform strain can only occur due to anomalies within the specimen, such as voids, or due to erroneous DIC data that can result from faulty speckle patterns or lighting complications. Therefore, strain values are reported from average surface strains along the gauge length of the specimen. Visualizations are only used to verify uniform loading and as a method for ensuring tests were conducted on high-quality specimens.

Figure 17 shows major strain maps for a DGEBA EW175 epoxy cured with 4,4'-DDS for various points during tensile loading. The map to the far right represents the image set immediately preceding failure. As the applied stress increased, the strain increased in a uniform manner across the entire surface. Uniform strain distribution was verified by the sharp peak in the histogram connected to the legend for each point during the test. It was not until late in the test that a slight broadening of the strain distribution was seen.
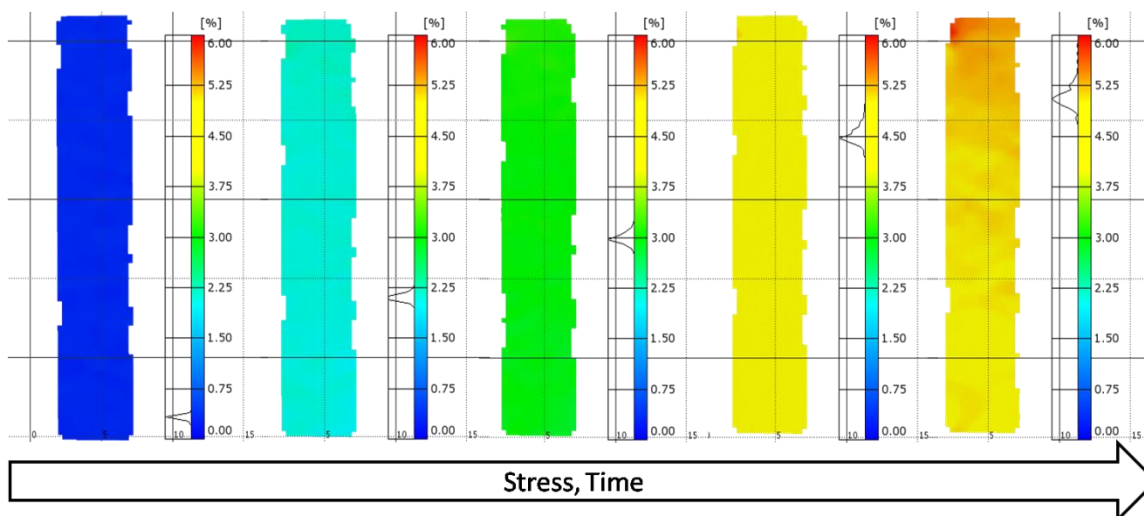
Figure 17. Major Strain maps for a tensile test of a dog bone specimen.

Resulting stress vs. strain curves for three tensile tests of DGEBA cured with

3,3'-DDS are seen in Figure 18, with strain values calculated from DIC measurements.

The plot shows the reproducibility of DIC strain data as all curves track uniformly with

one another throughout the small strain region and into the non-linear viscoelastic region.

The only noticeable difference in curves is the point of fracture, with the stress and strain

values at failure varying significantly. This difference is a common trait of glassy

crosslinked networks as failure propagates from defects within the specimen.

Concentration and size of defects is difficult to control when casting and curing these

epoxy networks, leading to significant deviation in stress and strain at failure.
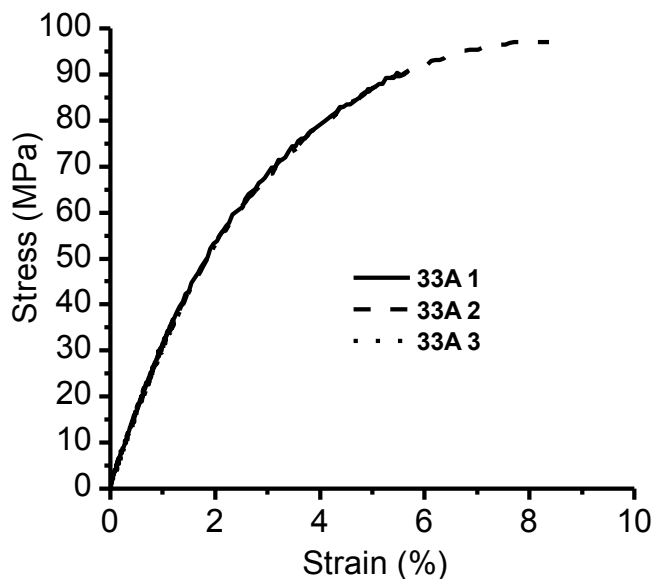
Figure 18. Repeatability of stress-strain curves using DIC

Comparative analysis of stress vs. strain curves generated from machine measured LVDT data to the stress vs. strain curves generated from DIC calculated strain indicates a significant deviation in both modulus values and failure strain. Figure 19 displays both types of stress vs. strain curves for DGEBA EW 175 cured with 3,3'-DDS (33A) and 4,4'-DDS (44A). Initial slopes indicated a vast difference in the calculated modulus values of the two methods. Table 6 lists the calculated modulus values and failure strains as determined by each method. This data shows a modulus increase of ~900 MPa when DIC calculated strain values were used. The failure strain was also significantly lower when DIC calculated strain was used. Even though the stress-strain curves generated using LVDT based strain showed no noticeable slippage, these results indicate that they still contained a large amount of erroneous strain data.
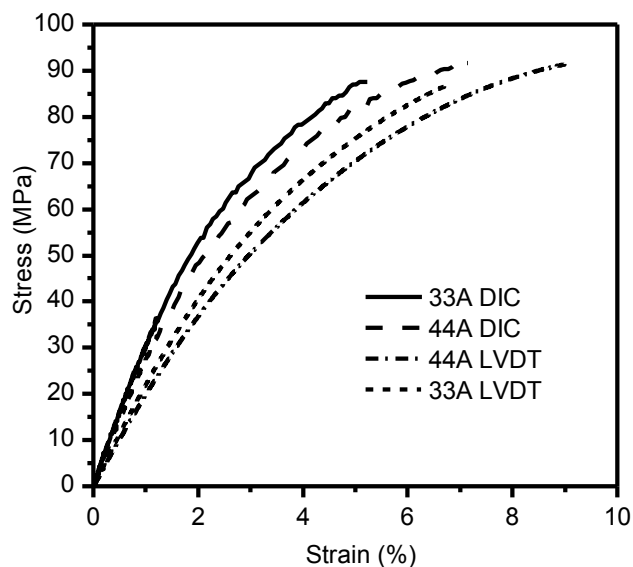
Figure 19. Comparison of stress-strain curves with DIC vs. LVDT measured strain

Table 6. Comparison of Modulus and Failure Strain Determined by DIC and LVDT

	Modulus (MPa)		Failure Strain (%)	
	DIC	LVDT	DIC	LVDT
33A	3320	2400	6.434	7.952
44A	3003	2108	6.126	7.986

While it is well known that LVDT measured displacement is not an accurate method for strain calculation, typical solutions require the use of contact extensometers or clip-on strain gauges. However, these devices provide accurate strain data only for the area in which they are connected and require contact with the specimen. These methods are appropriate only for tests in which the specimen strains uniformly, making these techniques adequate for tensile testing of neat polymer samples. However, DIC still provides an advantage due to the fact that it is non-contact and provides full-field strain measurement across the entire specimen surface. Additionally, DIC can be used to produce both axial and transverse strains. Simultaneous measurement of the axial and transverse strains allows for computation of the Poisson's ratio of the material, a feat that

cannot be accomplished by a single strain gauge or extensometer. The ability to obtain Poisson's ratio and capture full-field strain make DIC useful for even the simplest tests, such as uniaxial tension.

Poisson's ratios were calculated within the ARAMIS software by running a software script, which divided the minor strain by the major strain for the specimen surface. The resulting visualization shows the Poisson's ratio across the surface of the specimen. Figure 20 shows the average Poisson's ratio vs. total strain for tensile tests of the 44A and 33A systems. Three runs of each sample are displayed in order to show the reproducibility of the results. The initial portion of each curve contains a significant amount of noise due to both a high sample rate and the relatively low strains. At low strains the noise associated with DIC was a higher percentage of the total strain. As strain increased, the fluctuation decreased due to a higher signal to noise ratio. The Poisson's ratio for epoxy specimens was determined from the temporary dwell region that occured immediately following the high noise region. This method resulted in calculated Poisson's ratio values of 0.395 for the 33A system and 0.405 for 44A. This value is typical of epoxy systems and similar to values reported by the similar technique of moiré interferometry.[6]
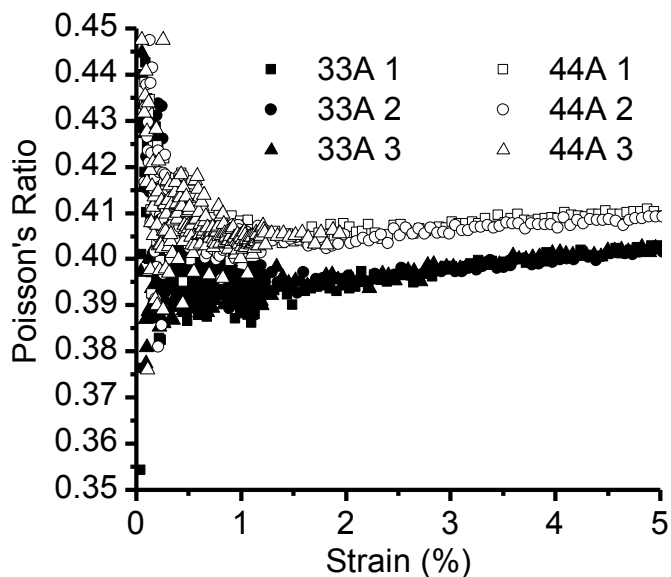
Figure 20. Calculated Poisson's ratio vs. total strain for 33A and 44A networks.

The difference in Poisson's ratio of the 33A and 44A systems, while only 1/100, is significant and was clearly reproducible as seen in Figure 20. As the Poisson's ratio increased at higher total strains, the Poisson's ratios of the two materials increased at the same rate. Poisson's ratio increased with strain as the higher stress on the system decreased the local time scale of molecular motions. As more motions became available, the amount of transverse contraction increased. The increase in Poisson's ratio would continue to a maximum near 0.50, which occurs post yield as the material behaves as a rubber.

<div align="center">Compression</div>

The tensile testing of epoxy matrices provided useful information in the form of tensile modulus and Poisson's ratio, but fell short in providing a complete deformation description of epoxy networks as failure occurred well before macroscopic yield of the specimen. Matrix yield characteristics cannot be obtained using tensile tests due to the tensile yield stress being greater than the fracture stress for highly crosslinked epoxies.

This leads to brittle failure before macroscopic yielding during tension.[7] This inherent brittleness is not an issue in uniaxial compression tests, allowing for loading through the yield point of the matrix, and subsequent acquisition of important yield criteria along with the small strain properties.

Proper uniaxial compression testing of glassy networks is complex. Uniform load is critical since platen or specimen surface misalignment creates non-linear force-displacements at low strain levels, and pre-mature specimen failure at high strain.[8] Accurate strain measurement in compression is particularly difficult since test specimens are relatively small cylinders, which require special extensometers or bonded-on strain gauges, which are cumbersome to handle, providing limited test data and requiring high skill for accuracy. Compression testing sub-press fixtures, which maintain appropriate platen alignment, are also restricting as they reduce the amount of work area around the specimen to affix strain measurement devices. For these reasons non-contact strain measurement devices, such as video or laser extensometers, are useful for compressive testing; however, they are limited to a fixed gauge length and only measure strain between extensometer edges (contact) or specimen surface marks (non-contact).[8] In the case of strain gauges, only the specific points of bonding are measured.

Methods

Compression testing procedures followed ASTM 695-02a. Cylinders were compressed at a displacement controlled test rate of 1.27mm/min on a MTS Systems Corporation Model 810 servo-hydraulic universal test frame equipped with a low friction compression sub-press (Wyoming Test Fixtures Model CU-SP). Linear variable differential transformer (LVDT) compression data was recorded from MTS Testworks®

software using a MTS 20 kip load cell at a sampling rate of 10Hz. Compression strain

measurements were recorded simultaneously using digital image correlation methods.

Advanced strain analysis using digital image correlation (DIC) was conducted

using a GOM Optical Measuring Techniques ARAMIS 3D Deformation Analysis System

(Trilion Quality Systems). Digital gray scale images of speckle coated cylinders were

captured via two 2M digital CCD cameras equipped with 50mm lenses at a frame

(capture) rate of 5fps for small strain analysis and 1fps for large strain analysis.

Calibration was performed using a 25mm x 20mm standard to obtain a resolution

deviation of less than 0.03 pixels.

Results

Small strain analysis. Digital image correlation provides a non-contact method to

analyze surface strains of material properties under deformation and compliments

traditional measurement techniques. When studying the compression behavior of glassy

polymer solids, the advantage of DIC is enhanced accuracy of small strain measurements.

The compression sub-press used for studying these materials is space constrained,

making it quite difficult to apply an extensometer or strain gages. As a result, the test

often relies on LVDT measurements which generate accuracy concerns. Figure 21A

compares the compressive stress-strain curves for the DGEBA-DDS cylinders generated

from LVDT and DIC measured strain. Although the curves have similar shapes and yield

stresses, significant differences in the small strain regions (Figure 21B) are observed as

the DIC data displays a larger initial slope and calculated modulus.
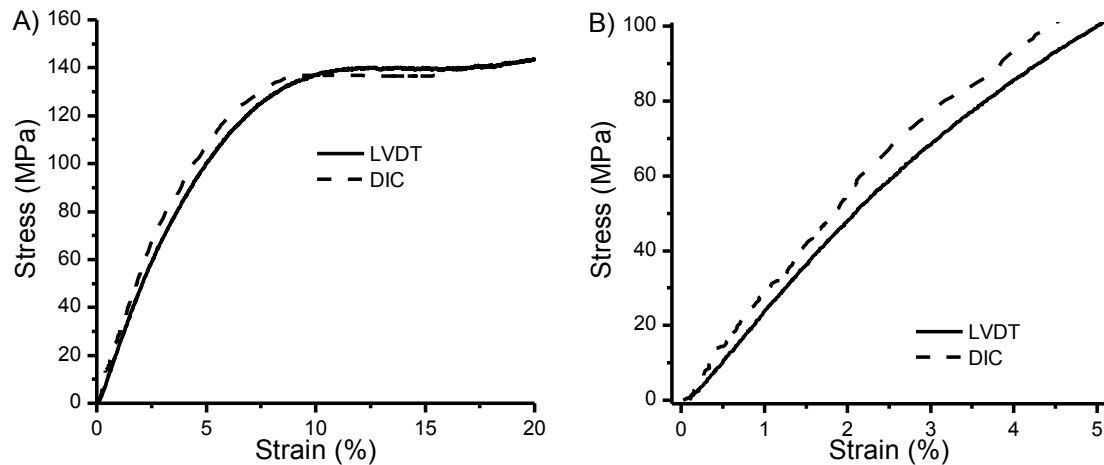
Figure 21. Comparison of DIC and LVDT generated stress-strain curves.

Like the tensile results presented above, erroneous strain due to fixture and

machine compliance can be effectively removed by use of DIC. To quantify the

differences in modulus values, a comparison of the apparent modulus values at different

longitudinal strains for DIC and LVDT is shown in Figure 22 (average of two tests).

Values were determined by the slope of a linear fit to the stress-strain curves in 0.25%

increments of longitudinal strain. Modulus values generated from LVDT increased to a

maximum of 2670MPa at 0.75% strain. The increase in modulus from 2301MPa at

0.25% strain to this maximum is attributed to erroneous displacements in the small strain

region. DIC calculated modulus values do not show this behavior since the measurement

is independent of machine and fixture compliance, and only the actual strain

deformations of the specimen under compression are measured. Thus, modulus values

are highest at the lowest longitudinal strains and subsequently decrease in a near linear

fashion. Peak modulus values were determined to be 3757MPa for DIC measurements at

0.25% strain. These observed differences of 1087MPa and 0.50% strain between

techniques demonstrates the improved accuracy in small strain measurements of DIC

when measuring uniaxial compression moduli of glassy polymer matrices.
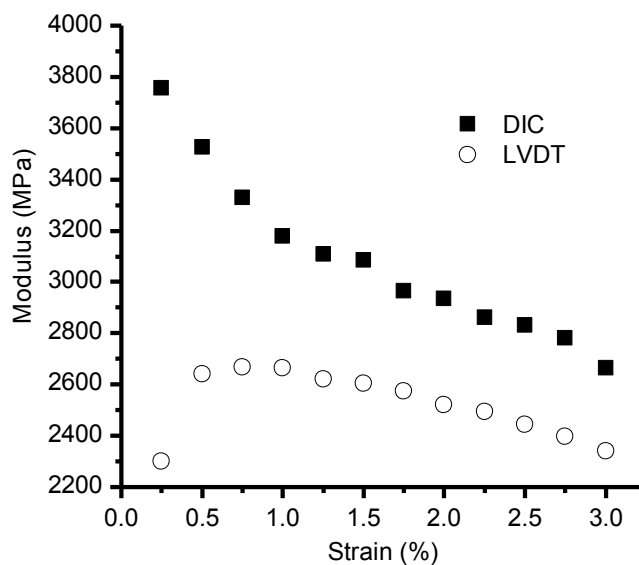
Figure 22. Comparison of LVDT and DIC calculated modulus values.

Poisson's ratio. Since strain measurements in DIC are calculated from

deformations in surface facets, transverse and longitudinal strains can be measured

simultaneously. As a result, calculation of Poisson's ratio for glassy polymer matrices is

attainable without the use of multiple extensometers or strain gauges. Figure 23 shows a

representative plot of the nominal Poisson's ratio determined from DIC calculated

longitudinal and transverse strains. Using this approach, we calculated the Poisson's

ratio for the DGEBA-DDS network to be 0.36 at peak modulus, or 0.25% longitudinal

strain. However, the Poisson's ratio increases at a significant rate from 0-1.5% strain,

making it difficult to determine an exact ratio in compression testing. As the longitudinal

strain increases toward 20%, the Poisson's ratio increases towards and eventually past a

value of 0.5. The non-realistic value of the high strain Poisson's ratio is corrected for by

using true strain instead of engineering strain. These results will be discussed in a subsequent section.
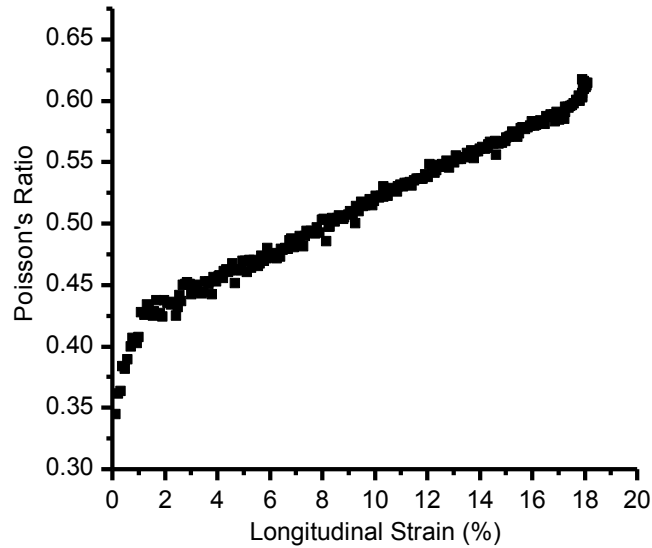
Figure 23. Poisson's ratio vs. longitudinal strain for epoxy network

True stress and strain. DIC is useful for the calculating true compression stress and strain of glassy polymer networks. Prior discussion has been based on nominal strain values determined from the DIC software and stress values calculated by $\sigma_n = F/A_0$ where F is the force and A_0 is the initial cross-sectional area of the cylinder. True strain values were generated from the DIC software, and true stress was calculated as $\sigma_t = F/A$ where A is the actual cross-section of the specimen at force F. Difficulty arises in calculating true stress due to limitations in obtaining accurate real-time cross sectional areas. Traditional methods calculate these values from the Poisson's ratio. However, it is difficult to calculate a precise Poisson's ratio in compression testing as discussed above. DIC computational analysis provides a method to apply a best-fit cylinder to 3-D cylindrical specimen surfaces. We applied this technique to calculate the glassy network cylinder radius throughout the compression loading test to determine actual cross-sectional area

with time. Figure 24 depicts how the best fit method was applied to determine the radius of the cylinder.
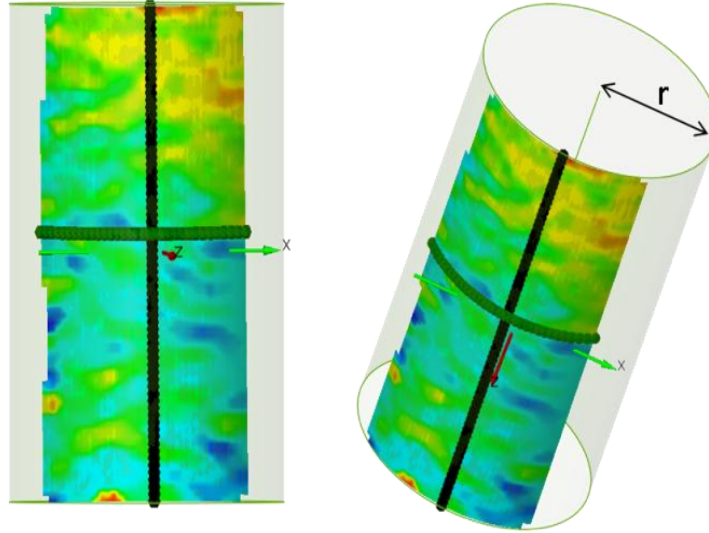
Figure 24. Cylinder strain map showing the application of a best-fit cylinder to the curvature.

Figure 25 compares the true stress vs. true strain curve with the nominal stress vs. strain curve for uniaxial compression of the DGEBA-DDS polymer network. The true stress vs. true strain curve more accurately depicts strain softening associated with increased radius due to specimen barreling. For this experiment, an increase in radius from 6.395mm to 6.689mm at yield was observed. The true longitudinal and transverse strains were also used to calculate the true Poisson's ratio. The true Poisson's ratio at peak modulus was calculated at 0.36, which is identical to the nominal Poisson's ratio presented above. A comparison of the true and nominal Poisson's ratios can be seen in Figure 26, in which the true Poisson's ratio increases to a maximum value of just under 0.50.
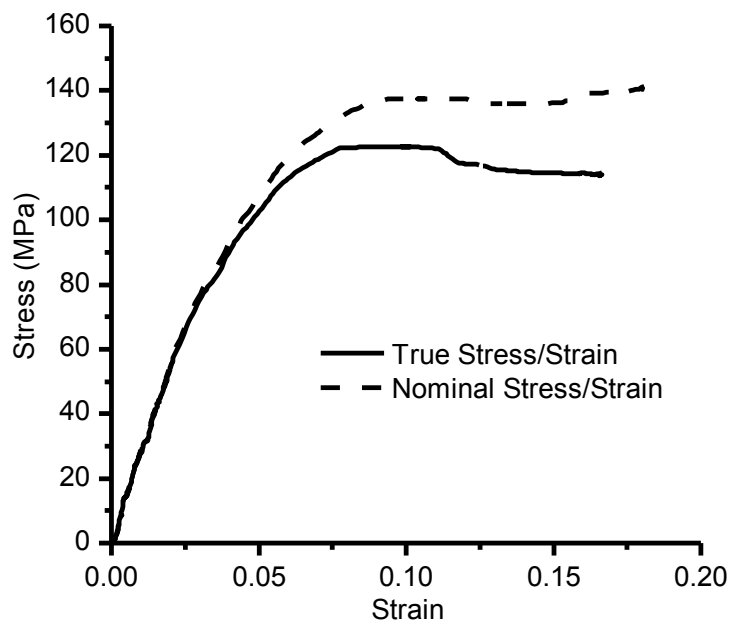
Figure 25. Comparison of DIC nominal and true stress-strain curves.
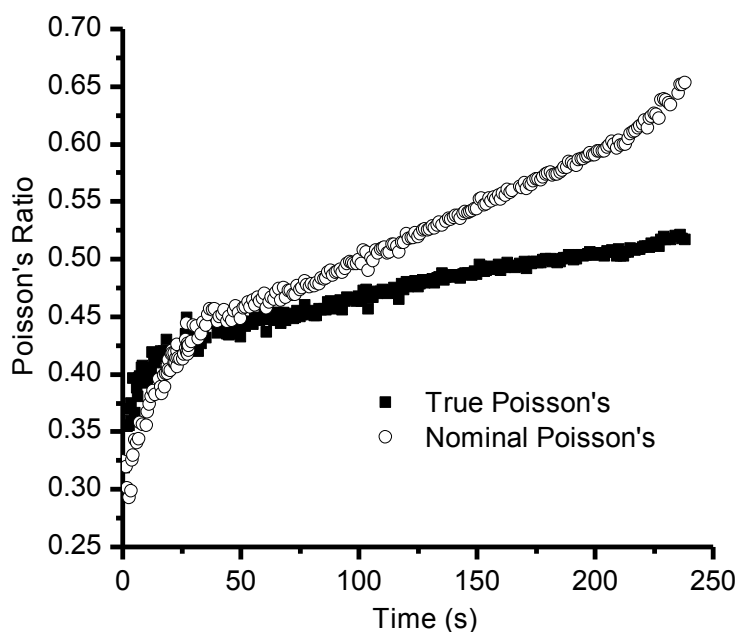
Figure 26. Comparison of true and nominal Poisson's ratio values.

Yield analysis. The yield point of the glassy polymer network is determined at the

peak load or the apparent "knee" in the stress vs. strain curves. Correlation of MTS load

data with digital image sets allowed for assignment of the specific image set where peak

load occurred. This image set was used to assign a uniaxial compression yield strain of

11.61% by averaging the total surface strains for the DGEBA / 4,4'-DDS glassy network.
In comparison, the LVDT measured compression yield was 12.42% for this sample. This
difference of 0.82% strain is significant and suggests 0.208mm of compliance strain for
the LVDT measurement. As a result, DIC is an excellent technique to determine the total
compliance within an experimental set-up.

Digital image correlation is particularly useful for studying the pre-yield and post-
yield strain behaviors of glassy polymer networks in uniaxial compression. To examine
pre- and post-yield strain behavior, strain profiles at various stages throughout the
compression test were analyzed. Figure 27 shows three DIC pre-yield capture images
(stages 48, 80, and 103) and three DIC post-yield capture images (stages 144, 165, and
194) with the legends colors altered to show development of strain in the center of the
specimen. Prior to yield, the strain profiles show mostly uniform strain across the surface
as indicated by small color gradients from top to bottom. Once the glassy polymer
cylinder yields, the material undergoes gross plastic deformation through "barreling"
which results in a more significant strain gradient across the specimen.

Further analysis can be conducted by tracking the strain along section lines placed
on the x- and y-axes of the specimen. Figure 28 shows strain along these axes for the
same stages represented in the strain maps seen in Figure 27. Strain along the x-axis is
represented by the green line, and strain along the y-axis is represented by the black line.
Notice that even prior to yield there appears to be a gradient in strain along the y-axis of
the specimen. Once exceeding the yield point the gradient becomes even more
prominent.
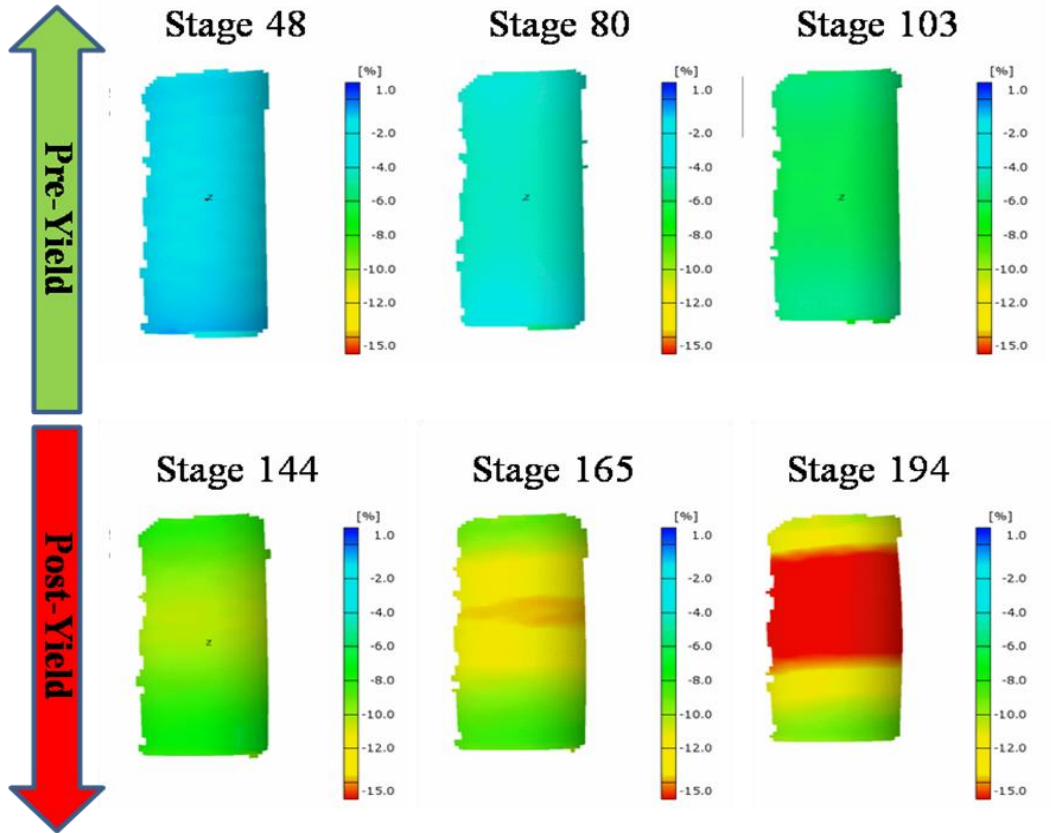
Figure 27. Pre- and post-yield strain maps of cylinder surface showing non-uniform deformation post-yield.
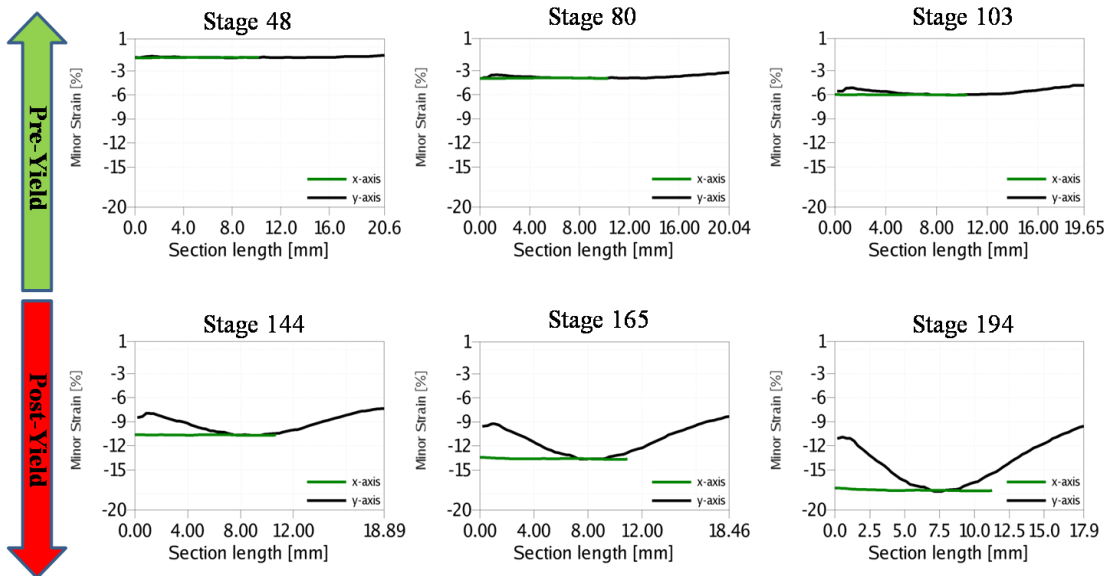
Figure 28. Strain along the x- and y-axes of cylindrical specimen.

This pre-yield strain gradient suggests deviation from uniformity begins well before the yield point of the matrix. Figure 29 presents a post-test digital analysis and plots the minor (longitudinal) strain vs. time for two stage points. Stage points are individual points selected by the analyst on the surface of the specimen. In this example, points were selected in regions of the cylinder where high longitudinal strain and low longitudinal strain were observed. At the yield point (11.61% average minor strain, time ~150s), the value of strain between these two stage points is deviated >5%. This result confirms the specimen does not deform at a uniform strain rate prior to yield. In fact, noticeable strain deviation between these stage points began at ~27s, or a longitudinal strain of 2.02%. Pre-yield deviation progressed slowly compared to post-yield deviation as observed in Figure 27. This post-yield behavior is attributed to the gross plastic deformation barreling of the glassy network cylinders, which creates large amounts of localized deformation.
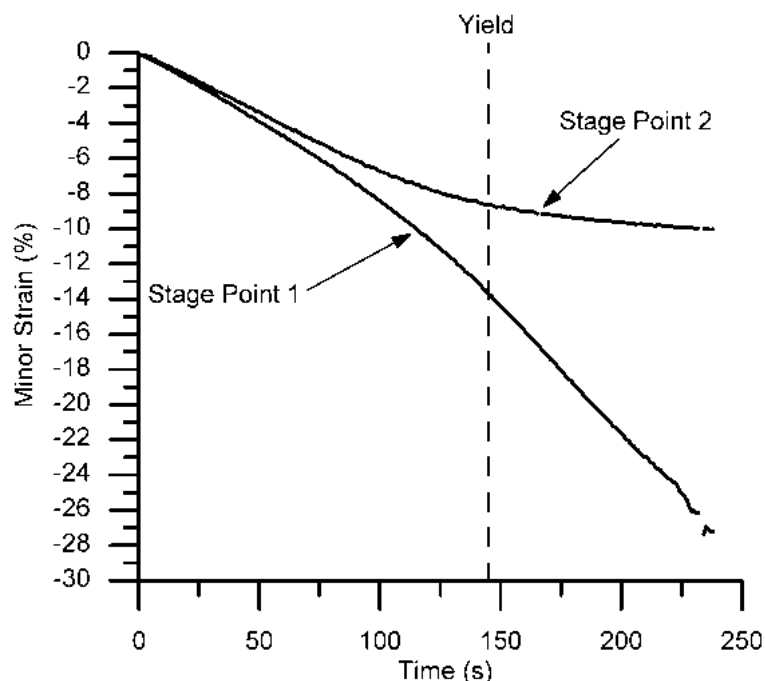
Figure 29. Local strain at two stage points, one in the higher strained region and one in the lower strained region.

Pre-yield strain deviation was further explored by comparing DIC minor strain vs. time to the traditional MTS compression stress vs. strain curve for the glassy polymer network in Figure 30. The traditional stress vs. strain curve is divided into three regions: elastic, anelastic, and plastic. These strain regions are segmented in the traditional stress vs. strain curve in Figure 30A with the elastic component assigned to the initial linear portion of the curve, the anelastic component assigned to the pre-yield non-linear segment of the curve and the plastic component assigned to the post-yield segment of the curve. Comparing the DIC strain vs. time plot in Figure 30B indicates the initial deviation of stage points at 2.02% correlates with onset of the anelastic strain component. This result is significant since the onset of non-uniform strain across the surface of the specimen correlates with the elastic to anelastic transition of the traditional method.
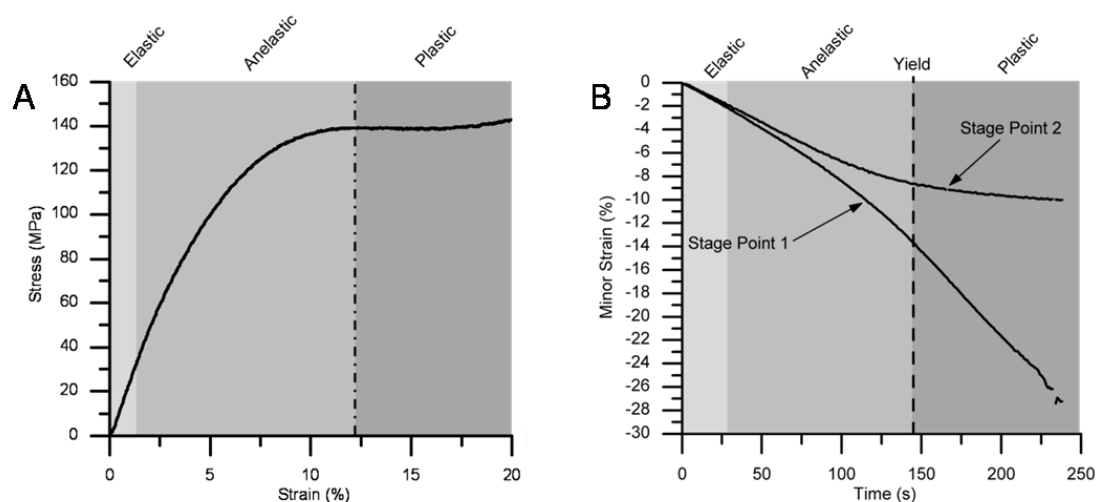
Figure 30. A) Stress-strain plot showing regions of strain. B) Strain vs. time plot showing the regions of strain.

These strain regions are distinguishable based upon their recovery behaviors. Instantaneous strain recovery is the elastic deformation component. Recovery over a certain length of time and/or temperature is the anelastic deformation component and any

non-recovered strain is considered irreversible or the plastic deformation component.[9,10,11] Therefore, strain recovery techniques were applied to further analyze the development of strain in glassy networks.

<div align="center">Strain Recovery with DIC</div>

Methods

Strain recovery experiments were conducted on the epoxy matrix at unloading strains both pre- and post-yield. Cylinders were compressed at a displacement controlled rate of 1.27mm/min up to the unloading strain, at which point, the load was immediately removed at the maximum allowed machine displacement rate, and the recovery was monitored. Strain recovery measurements were conducted using digital image correlation. A triggerlist, or capture sequence, was written to provide the optimum capture rate for each portion of the strain recovery test. The frame (capture) rate was set at a rate of 1fps for the loading segment of the strain recovery test. Just prior to unloading, the frame rate was increased to 10fps in attempt to capture the elastic strain recovery. Approximately 30s post unloading, the frame rate was reduced to a slower rate of 1 fps for 30s and finally to 1 frame per minute for approximately 10 minutes post unloading. Camera calibration was performed using a 25mm x 20mm standard to obtain a resolution deviation of less than 0.03 pixels.

Results

Figure 31 shows the individual stress vs. strain curves and strain vs. time curves for each of the recovery experiments of the 33A network where each line represents a different unloading strain. As expected, the loading paths of the stress-strain curves track similarly up to the unloading point after which the specimens with the higher unloading strain show an increase in area within the recovery envelope. This increased area is due

to an increased amount of slower recovering anelastic strain, and in the case of post yield experiments, an increase in the amount of residual strain. The strain vs. time curves in Figure 31B also track similarly during the development of strain with recovery paths differing depending on the unloading strain. The final point of these curves represents the amount of residual strain after ~10 minutes. All pre-yield experiments recover to a strain value at or near zero while post-yield experiments show a residual strain after 10-minutes. As the unloading strain increased, so did the amount of residual strain.
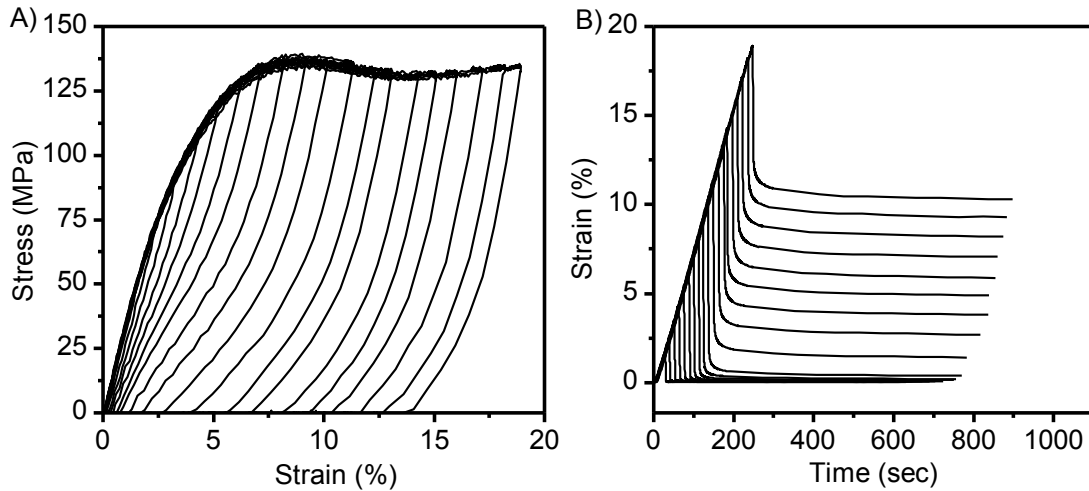
Figure 31. Stress vs. strain curves for strain recovery experiments with increasing unloading strains.

Strain type quantification. Further analysis of the strain recovery data allows for the quantification of the amounts of elastic, anelastic, and plastic strains applied to the specimen during loading. Attempts were made to experimentally measure the amount of elastic strain placed on the specimen. However, due to non-instantaneous unloading rates some anelastic strain was recovered along with the elastic strain during the unloading process. Therefore, the amount of elastic strain was calculated according to the theory of linear elasticity:

$$\varepsilon_{elastic} = \sigma_t / E_{ur} \qquad\qquad \text{Equation 8}$$

in which E_{ur} is the unrelaxed modulus and σ_t is the stress at the unloading time. Previous research measuring strain recovery has employed this method for the calculation of elastic strain.[10,12,13,14,15] Anelastic strain was subsequently calculated by subtracting the amount of calculated elastic and measured residual strains from the total strain applied during loading:

$$\varepsilon_{anelastic} = \varepsilon_{total} - \varepsilon_{elastic} - \varepsilon_{residual}$$ Equation 9

Strain component plots can be generated from these calculations in order to show how strain develops during loading. Figure 32 shows a component plot determined from the 10 minute residual strain data. The plot shows the amount of elastic, anelastic, and plastic strains that are placed on the specimen during loading along with the corresponding stress-strain curve. Each set of points corresponds to a cylinder that was unloaded at that total strain on the stress-strain curve. Elastic strain, represented by square symbols developed rapidly during the linear elastic strain region. Anelastic strain developed from the start and became the dominant strain mechanism once the total strain of the system extended past 5%. The onset and development of plastic strain occurred once the specimen was been taken past the yield point.
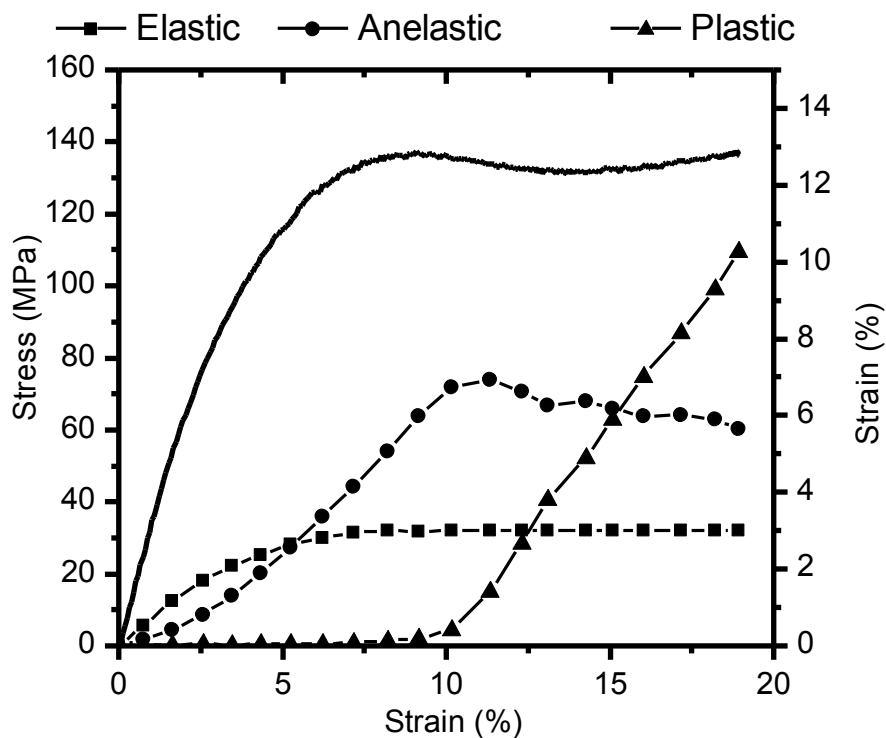
Figure 32. 10 minute component curves with calculated elastic strain values.

Effects of time and temperature on strain recovery. The results illustrated above were limited to recovery times of only 10 minutes post unloading. While a large amount of anelastic strain was recovered during this time, more strain was recovered over an extended period of time or with an increase in recovery temperature. In order to explore the complete recovery of these networks, cylinders were allowed to recover for an extended period of time at room temperature before being placed in an oven at elevated temperatures. It has been reported that complete anelastic strain recovery occurs at a temperature of T_g-20°C for 1 hour.[12,16,17] The residual strain was quantified at each point and plotted along with the 10 minute residual strain in Figure 33. The results of elevated temperature recovery will be discussed in more detail in subsequent chapters.
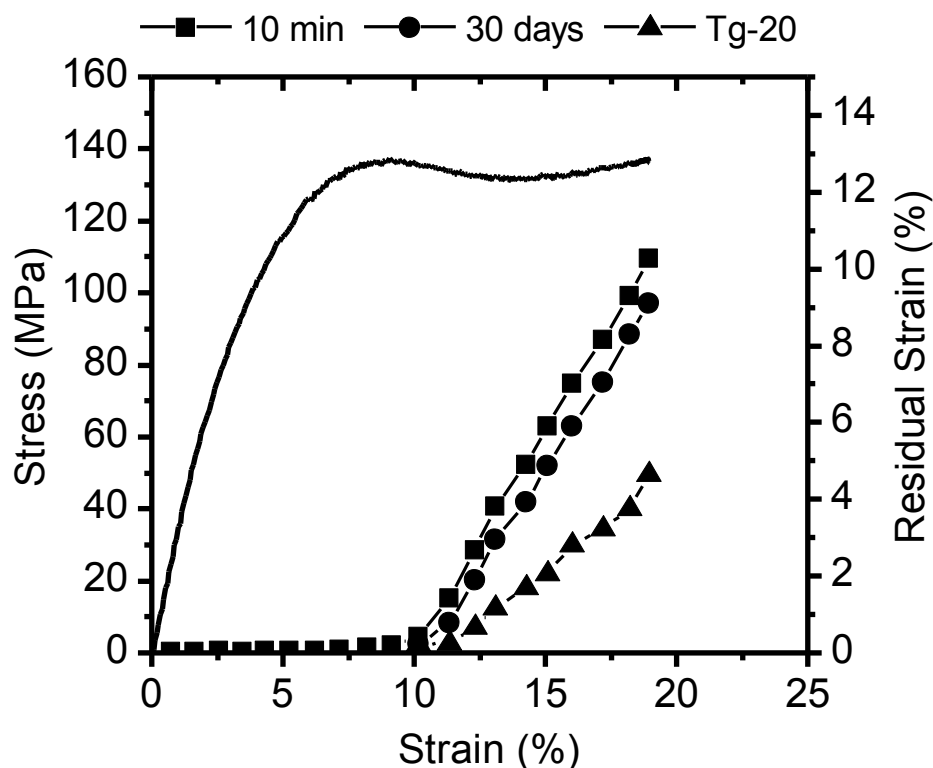
Figure 33. Residual strain plots for 10 minute recovery, extended recovery and Tg-20 recovery.

Using the residual strain from the T_g-20°C specimen, the total sub T_g recovery components were determined and plotted in Figure 34. These plots differ significantly from the 10 minute recovery curves shown in Figure 32 as a larger amount of strain was recovered during the elevated temperature dwell. This recovered strain caused a shift in the component plots from residual strain being the primary component to anelastic strain being the primary component. The post yield drop in anelastic strain was absent from the new curves as anelastic deformation continued to increase post yield. The slope of the anelastic strain component began to decrease as the material was strained past the strain softening region. This result is similar to what has been reported by Quinson and co-workers for deformation of amorphous PMMA.[12]
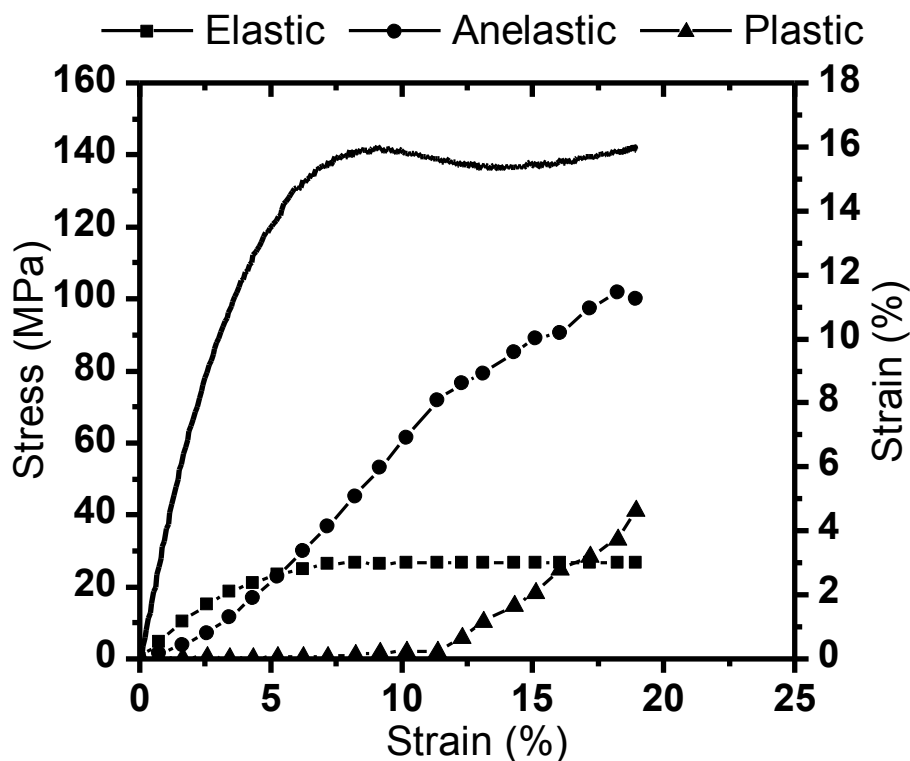
Figure 34. Component curves generated following 1 hour treatment at Tg-20.

Development of Strain

The results above, coupled with strain maps of a deforming cylinder, were used to illustrate the deformation mechanisms of these amorphous epoxy glasses and help to provide a better understanding of the strain and yield mechanisms of glassy solids. As previously discussed, the cylindrical specimen began deforming at a non-uniform strain rate once the magnitude of total strain extended beyond the linear elastic region. Referring to the Kelvin-Voight model of nonlinear viscoelastic deformation (Figure 8) and the strain component curves seen in Figure 34, an explanation for the development of strain can be derived. The Kelvin-Voight Model is used as a simple illustration of time dependency for anelastic strain components in the form of parallel springs and dashpots. Multiple spring and dashpot in series is representative of the multiple motions that contribute to the time dependency of anelastic strain.

Elastic	Anelastic	Plastic

Time-dependent deformation
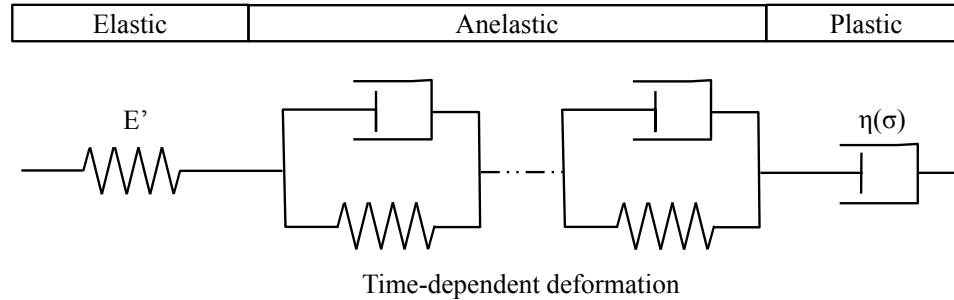
Figure 35. Kelvin-Voight model for nonlinear viscoelasticity.

The elastic, or spring like strain, developed rapidly during the initial linear region of the stress-strain curve. Once the slope of the stress-strain curve began to decrease, the elastic strain approached a plateau, which it reached as the stress reached a maximum value at the matrix yield point. According to equation 8, no more elastic strain can develop after this point. Anelastic strain developed immediately upon loading and increased beyond the yield before the rate of anelastic strain development began to decrease following the strain softening region. The anelastic strain component can be further divided based on the time scale of recovery. As seen in the Kelvin-Voight model the anelastic components are represented by springs and dashpots in parallel. The anelastic recovery appears to occur in two separate stages for the 33A network with the first being non-elastic strain that was recovered at room temperature and the second stage being recovery that occured with an increase in thermal energy. Referring back to Figure 33, there is a clear change in slope of the residual strain curves upon the introduction of thermal energy into the recovery process. This change in slope indicates the activation of the secondary recovery processes that would not occur in a reasonable time scale at the testing temperature.

Figure 36 shows the development of strain at various points along the stress-strain curve. Uniform strains were initially observed and then followed by the development of

a strain gradient across the specimen surfaces during compression. While the stress-strain curve indicated bulk yielding of the cylinder, the actual yield only occurred in a localized region. At the yield point of the stress-strain curve, the locally yielded region appears in red within the DIC strain maps (A). These measurements were combined with histograms (C) to display the relative concentration of strains across the specimen surface. Histograms were constructed from individual strain values associated with each facet used to generate the DIC strain maps. According to the quasi-point defect theory,[18,19,20,21] anelastic strain develops in the form of shear micro-domains (SMDs), which nucleate from imperfections within the network. Higher pre-yield strains near the center of the specimen are due to a growing concentration of SMDs. Yielding occurs when SMDs begin to coalesce allowing for large segmental motion, thereby creating plastic zones and strain gradients, which propagate towards the specimen ends.
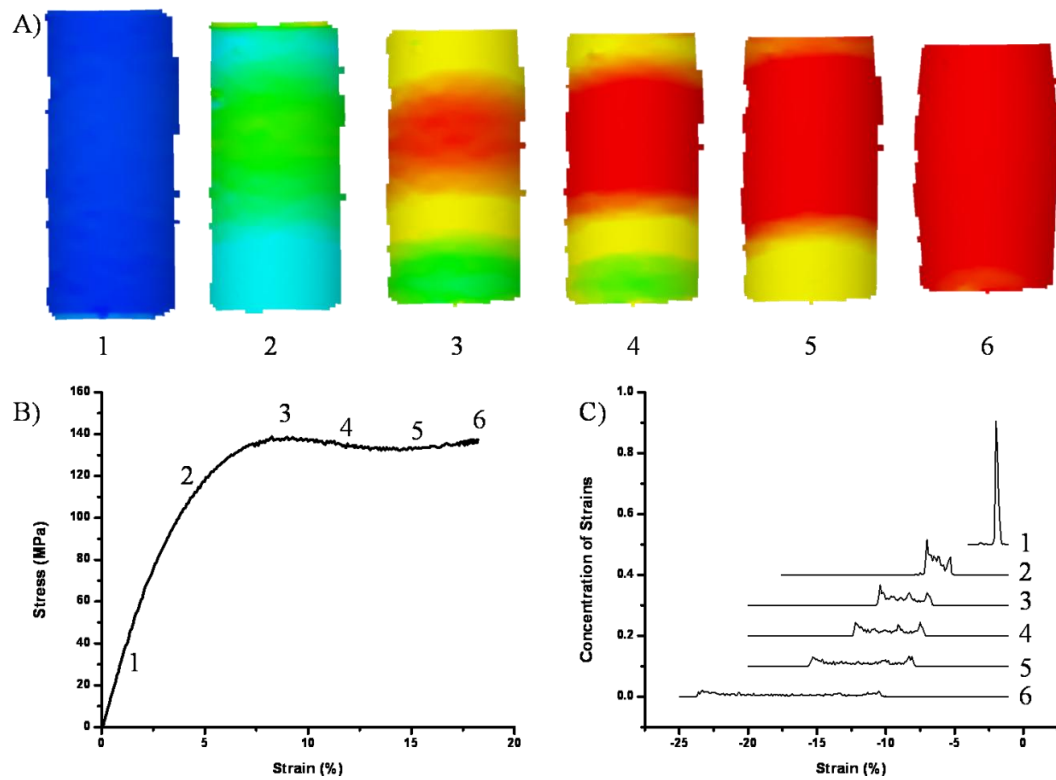
Figure 36. Diagram illustrating the development of strain on an epoxy cylinder.

DIC full-field strain maps provide further insights into the strain behaviors of glassy polymer networks in deformation. The resulting strain maps depicted in Figure 36 clearly show non-uniform surface strains across the specimen during compression. This was confirmed by the histograms, which showed a clear distribution of strain values outside of the linear portions of the stress strain curves. Yield strains are typically reported as the global strains of the specimens and not as local strains of the yielded regions. Higher strained yielded segments combined with lower strained pre-yield segments result in an average strain that is not indicative of the true event. DIC displays an average surface strain at yield for 33A at 9.07%, but the strain maps revealed locally strained regions of the specimen were >10.8%.

To show the effect of local yield on recovery, strain maps of a 33A cylinder loaded to 12.0% total strain are depicted in Figure 37 where only a portion of the cylinder has yielded. This series of strain maps shows recovery from peak strain with locally yielded regions displayed in red (>10.8% strain), through room-temperature, to the complete recovery after Tg-20°C. As seen in the complete recovery strain map after Tg-20°C conditioning, regions that did not yield show full recovery.
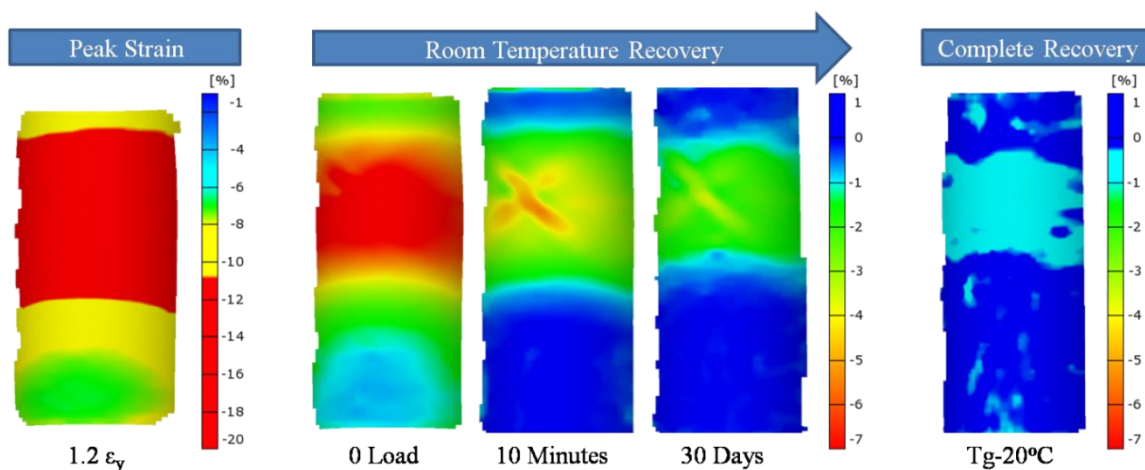
Figure 37. Recovery strain maps showing locally yielded regions.

Conclusions

The objective of this chapter was to describe the digital image correlation techniques used to study uniaxial deformation properties of glassy polymer networks. Tensile and compression measurements of glassy networks are fraught with challenges associated with obtaining accurate strain measurement. DIC provides a non-contact technique simple to use and advantageous to generate accurate/reproducible data for analyzing compression modulus, Poisson's ratio, and yield strain. DIC provided a substantial increase in accuracy for measuring strain compared to LVDT and also allows for simultaneous longitudinal and transverse strain measurements to calculate Poisson's ratio. DIC was particularly sensitive for measuring small strain compression modulus. An accurate yield strain was obtained using DIC, which clearly eliminated erroneous strain data associated with fixture and equipment compliance.

DIC techniques were also developed for studying the pre-yield, yield and post-yield behavior of glassy polymer solids. DIC was used to measure compressive strain recovery of epoxy glasses in order to provide useful insights into the deformation analysis of the epoxy networks by illustrating clear strain localization prior to macroscopic yielding. This strain localization was present in the center of the cylindrical specimens once the total strain of the test extends beyond the linear viscoelastic strain region. This strain localization is due to the development of anelastic strain in the form of shear micro domains, which eventually coalesce to create macroscopic yielding. The anelastic strain recovery occurs in two distinguishable time scales, the first occurs at room temperature over an extended period of time and the second occurs only after the introduction of thermal energy to the system.

The methods developed in this chapter were further utilized for the comparison of epoxy networks of differing molecular structure. By altering network architecture, a better understanding of the mechanisms associated with this non-linear viscoelastic behavior will be obtained.

References

1. Jerabek, M.; Major, Z.; Lang, R.W. *Polym Test* **2010,** *29,* 407-416.
2. Parsons, E.; Boyce, M.C.; Parks, D.M. *Polymer* **2004,** *45,* 2665-2684.
3. Parsons, E.M.; Boyce, M.C.; Parks, D.M.; Weinberg, M. *Polymer* **2005,** *46,* 2257-2265.
4. Godara, A.; Raabe, D. *Compos. Sci. Technol.* **2007,** *67,* 2417–2427.
5. Godara, A.; Raabe, D.; Bergmann, I.; Putz, R.; Muller, U. *Compos. Sci. Technol.* **2009,** *69,* 139–146.
6. O'brien, D.J.; Sottos, N.R.; White, S.R. *Exp. Mech.* **2007,** *47,* 237-249.
7. Mayr, A.E.; Cook, W.D.; Edward, G.H. *Polymer* **1998,** *39,* 3719-3724.
8. Jerabek, M.; Major, Z.; Lang, R.W. *Polym. Test.* **2010,** *29,* 302-309.
9. Gauthier. C. In *Mechanical properties and testing of polymers: an A-Z reference.* Swallowe, G.M. Ed. Kluwer Academic Publishers: Dordrecht, 1999, p. 191.
10. Pegoretti, A.; Pandini, S.; Ricco. T. *Polymer* **2006,** *47,* 5862-5870.
11. Bendler, J.T.; LeGrand, D.G.; Olszewski, W.V. *Polymer* **2002,** *43,* 389-394.
12. Quinson, R; Perez, J; Rink, M; Pavan, A. *J. Mater. Sci.* **1996,** *31,* 4387-4394.
13. Ricco, T.; Pegoretti, A. *J. Polym. Sci. Pol. Phys.* **2002,** *40,* 236-243.
14. Pegoretti, A.; Guardini, A.; Migliaresi, C.; Ricco, T. *Polymer* **2000,** *41,* 1857-1864.
15. Rinaldi, R.; Gaertner, R.; Chazeau, L.; Gauthier, C. *Int. J. Nonlin. Mech.* **2011,** *46,* 496-506.
16. David, L.; Quinson, R.; Gauthier, C.; Perez, J. *Polym. Eng. Sci.* **1997,** *37,* 1633-1640.
17. Oleynik, E. *Prog. Coll. Pol. Sci. S.* **1989,** *80,* 140-150.
18. Perez, J. *Polym. Sci. Ser. B.* **1998,** *40,* 17.
19. Perez, J. *Solid State Ionics* **1990,** *39,* 69.
20. Perez, J.; Balkem, A.A. *Physics and Mechanics of Amorphous Polymers*, Brookfield: Rotterdam, 1998.
21. Gautheir, C.; Pelletier, J.M.; David, L.; Vigier, G.; Perez, J. *J. Non-cryst. Solids.* **2000,** *274,* 181-187.

CHAPTER IV

COMPARISON OF THE NON-LINEAR VISCOELASTIC BEHAVIOR OF DGEBA

CURED WITH 3,3'- AND 4,4'-DDS

Introduction

The previous chapters have described the methods that have been developed for

the analysis of glassy epoxy networks. Over the next few chapters, these methods will be

employed for analysis of differing networks in order to develop relationships between

network architecture and mechanical performance. The focus of this thesis is to explore

the effects of structural isomerism on matrix performance. Investigating networks of

identical chemical composition but different connectivity allows for the effects of

network mobility to be explored. Traditional structure-property studies normally

investigate materials of different structure, i.e. differing chain lengths, varying

functionality, different linking units, etc. While these studies are effective at determining

some general relationships, exact effects on performance cannot be determined as often

the composition of the network has been altered.

This chapter explores the mechanical performance of low molecular weight

diglycidyl ether of bisphenol-A (DGEBA) cured with the meta-substituted 3,3'-

diaminodiphenyl sulfone (3,3'-DDS) and the para-substituted 4,4'-diaminodiphenyl

sulfone (4,4'-DDS). The difference in tensile and compression performance will be

explained by the use of strain recovery techniques to explore variances in strain

development. These methods will be employed to compare the pre- and post-yield

deformation of the two epoxy networks of identical chemical composition but different

curative isomer structure. The results will provide insights into architectural

contributions to strain behavior since variations in chemical composition are eliminated.

The 3,3'-DDS isomer based upon a meta-substituted curative introduces kinks into the polymer network segments while the 4,4'-DDS para-substituted isomer generates more linear segments (Figure 38). These architectural variances have a profound influence on thermomechanical properties leading to observed differences in modulus and T_g. Digital Image Correlation (DIC) methods provide a pathway to compare glassy network strain component behaviors to architectural variances associated with chemical compositions.
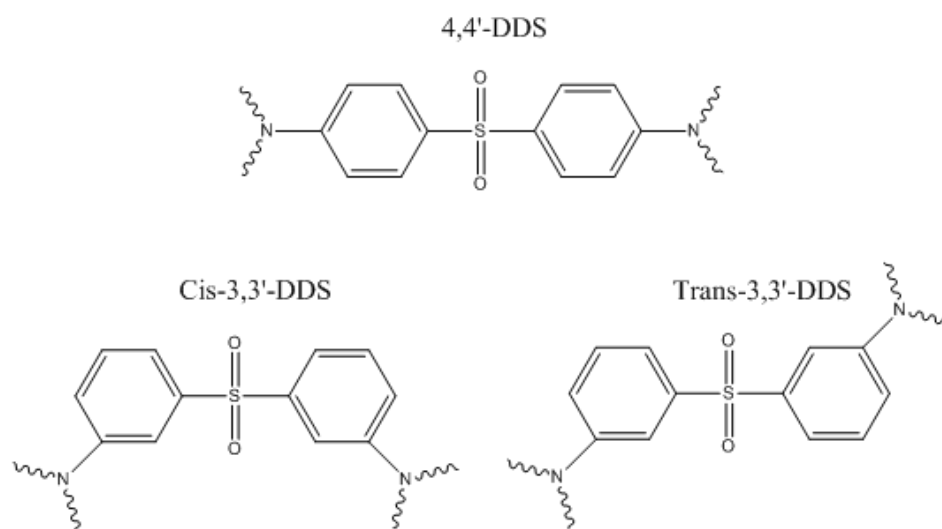
Figure 38. Structures of 4,4'- and 3,3'-DDS.

Results

Comparison of Tensile and Compressive Stress-Strain Behavior

Representative stress vs. DIC measured strain curves for 3,3'- and 4,4'-DDS isomer cured epoxy networks (referred to as 33A and 44A for the remainder of this chapter) are shown in Figure 39. The two chemically identical networks deform in a different manner with the 33A system possessing a higher modulus and lower yield strain than the 44A network (Table 7). The more rigid behavior of the 33A network is accompanied by a lower yield stress and larger amount of strain softening compared to the 44A network. Due to the identical composition, this different mechanical behavior

must be a direct result of the architectural differences of the two networks associated with

the structural isomerism of the curative.
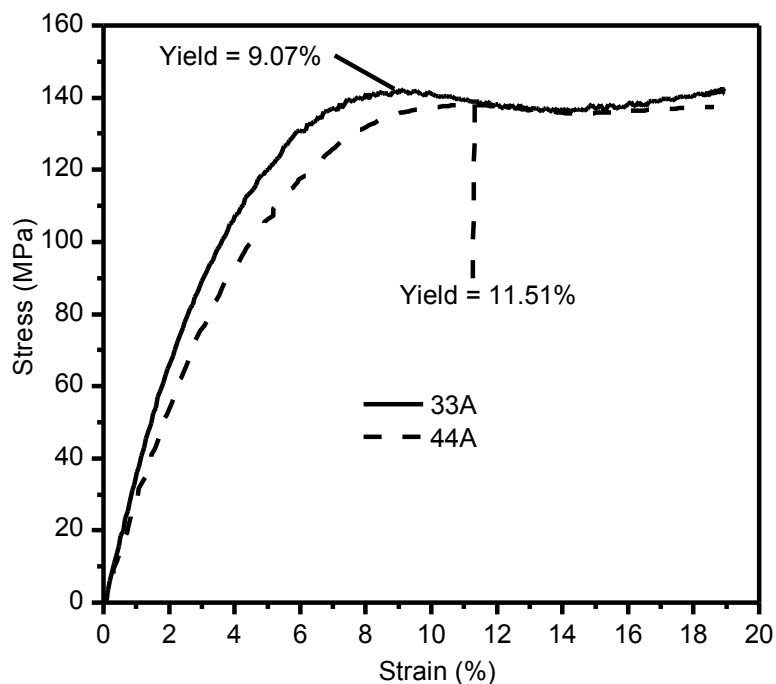
Figure 39. DIC based stress vs. strain curve identifying the yield point of the epoxy matrix.

Table 7. Compressive Properties of 33A and 44A

	Compression Modulus (MPa)	Yield Strain (%)	Yield Stress (MPa)
33A	3914	9.07	142.2
44A	3691	11.51	139.7

Tensile stress-strain curves are shown in Figure 40 revealing the same trend of

more rigid behavior of the 33A network. Failure stress and strain are skewed due to large

variances caused by the brittleness of the two networks. Dilational failure in tensile

analysis of epoxy networks is largely defect driven. Cracks propagate rapidly from flaws

in the network, causing non-reproducible failure before distortional yielding can occur.

Poisson's ratios of the two networks are noticeably different for the two networks, with a

value of 0.405 for the 44A network and 0.395 for the 33A network. This discrepancy in

Poisson's ratio suggests that the 44A network can more readily contract in the transverse direction when loaded axially.
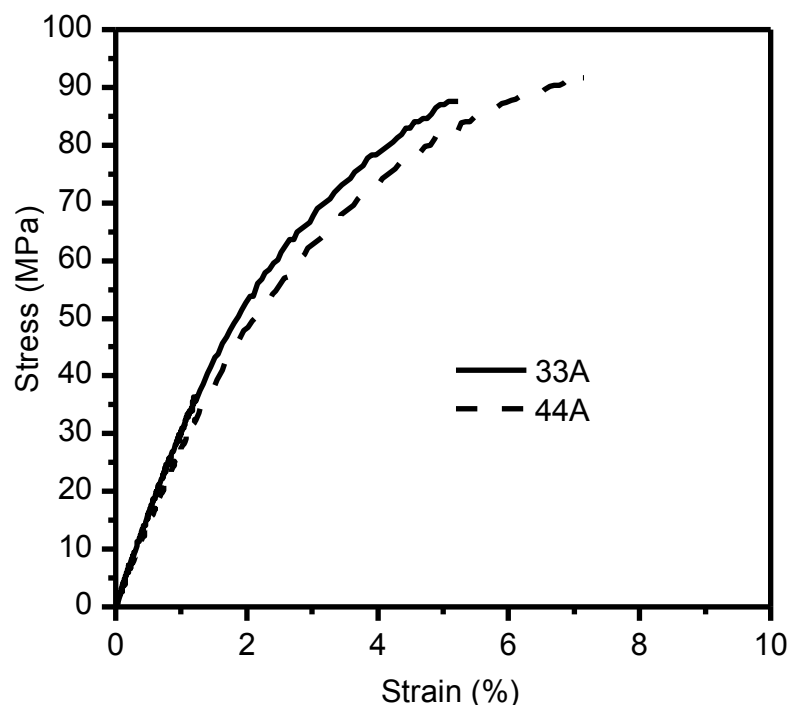
Figure 40. Tensile stress-strain curves for 44A and 33A networks.

Table 8. Tensile Properties of the 33A and 44A Networks.

	Modulus (MPa)	Failure Strain (%)	Failure Stress (MPa)	Poisson's Ratio
A33	3320	6.434	91.7	0.395
A44	3003	6.126	72.5	0.405

Thermomechanical Behavior

Dynamic mechanical analysis was conducted on the isomer networks in order to investigate the modulus (E') and Tan δ vs. temperature relationships (Figure 41A). The most noticeable variance in thermomechanical behavior of the isomers is the difference in the α-transition, or glass transition temperature. The 33A network shows a significantly lower T_g compared to 44A. The E' behavior of the two networks is similar, with the 33A network possessing a slightly higher room temperature modulus. DMA is particularly

useful for analysis of the sub-T_g transitions discussed in the introduction. Therefore,

dynamic mechanical analysis (DMA) was also used to analyze sub-T_g transitions for 33A

and 44A. Figure 41B shows the Tan-δ curves enlarged to show sub-T_g molecular

motions between $^-$115 – $^+$80°C. The large sub-Tg transition is labeled as β-transition and

smaller transition (only visible in the 33A network) is labeled as the γ-transition. The

44A isomer shows a significantly larger and broader β-transition, indicating the

availability of more glassy state molecular motions. The 33A network shows a bimodal

distribution of sub-Tg transitions suggesting more restricted glassy state molecular

mobility for this polymer. The location of the peak maximum and peak area for the α-

and β-transitions of 33A and 44A are seen in Table 9, indicating higher temperature

transitions with larger areas for the 44A network.
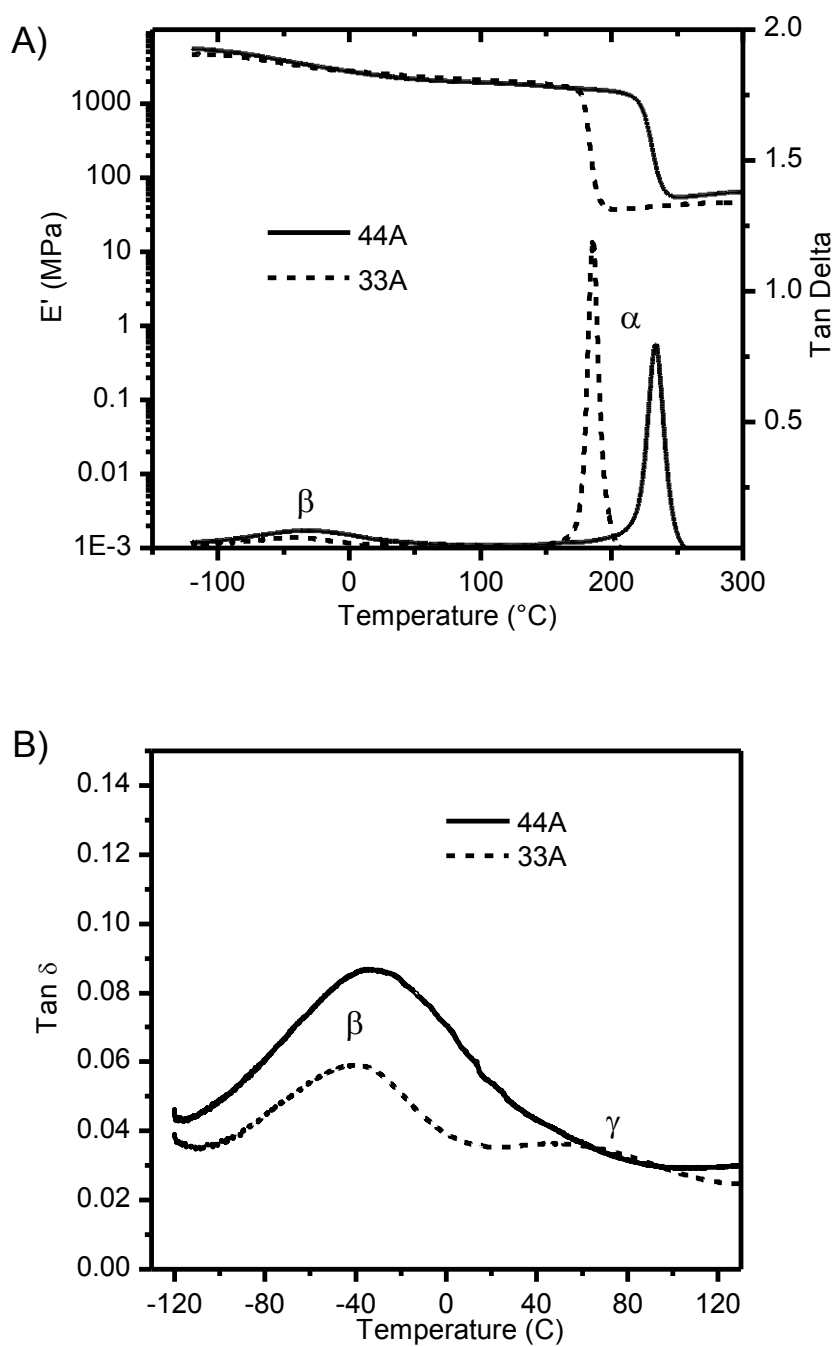
Figure 41. DMA modulus and Tan δ curves for the 33 and 44DDS cured networks.

Table 9. DMA Tan δ Determined Sub-Tg Peak Location and Area.

	T_β (°C)	β Area	T_α (°C)	α Area
44A	-29.9	4.48	233.5	15.15
33A	-38.7	2.38	185.5	14.27

Motions associated with the sub-Tg transitions in epoxy networks were discussed in the introduction, with the most likely contributions coming from rotations of para-substituted phenyl rings and crankshaft motions of the hydroxypropyl ether (HPE) segments.[1, 2, 3] Figure 42 provides an illustration of these available motions, which due to their proximity to one another, could possess some cooperativity accounting for some of the deformation capabilities of epoxy networks.
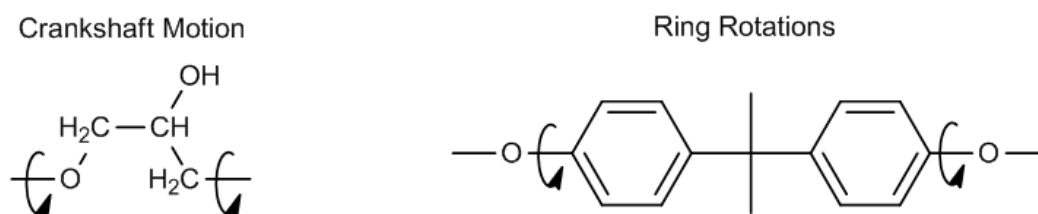
Figure 42. Motions associated with sub-Tg transitions of epoxy networks.

Both of the motions depicted in Figure 42 are from within the DGEBA segment of the network. Recall that the networks contain identical chemical composition, meaning the amount of DGEBA segments is the same in both networks. The presence of a larger β-transition in the 44A network suggests that there is a larger amount of motions within the amine curative segment compared to the 33A network. This added availability of motions is likely due to the addition of more para-substituted phenyl rings into the network, a concept that will be explore in more depth in a subsequent section of this chapter.

Strain Recovery Analysis

   Strain recovery experiments were conducted on each network, and curves were produced using the strain data generated from digital image correlation. However, strain control during testing was conducted via the system LVDT. 33A and 44A networks were unloaded at strains based on their yield strains in order to provide a method of directly comparing strain development in the two networks.   A LVDT determined yield strain of 12.50% was determined for the 44DDS cured network, and a value of 10.03% was determined for the 33DDS cured network. These values were subsequently used to develop the strain recovery test matrix seen in Table 10. LVDT measured strain values were used for the development of this test matrix to ensure appropriate strain control during strain recovery tests. Experiments were displacement controlled based on real time LVDT measurements; therefore, it is important that the input values be derived from the same source. The test matrix is composed of 20 tests per system with unloading strains from 0.1 to $2.0\varepsilon_y$. Basing test conditions on the yield strain of the individual network will allow for direct comparison of the strain recovery processes within different networks.

Table 10. Strain Recovery Experiments Based on LVDT Yield Strains

Pre-Yield			Post-Yield		
Fraction of Yield Strain	44DDS Strain (%)	33DDS Strain (%)	**Fraction of Yield Strain**	44DDS Strain (%)	33DDS Strain (%)
$0.1\varepsilon_y$	1.25	1.0	**$1.1\varepsilon_y$**	13.75	11.0
$0.2\varepsilon_y$	2.50	2.0	**$1.2\varepsilon_y$**	15.00	12.0
$0.3\varepsilon_y$	3.75	3.0	**$1.3\varepsilon_y$**	16.25	13.0
$0.4\varepsilon_y$	5.00	4.0	**$1.4\varepsilon_y$**	17.50	14.0
$0.5\varepsilon_y$	6.25	5.0	**$1.5\varepsilon_y$**	18.75	15.0
$0.6\varepsilon_y$	7.50	6.0	**$1.6\varepsilon_y$**	20.00	16.0
$0.7\varepsilon_y$	8.75	7.0	**$1.7\varepsilon_y$**	21.25	17.0
$0.8\varepsilon_y$	10.00	8.0	**$1.8\varepsilon_y$**	22.50	18.0
$0.9\varepsilon_y$	11.25	9.0	**$1.9\varepsilon_y$**	23.75	19.0
$1.0\varepsilon_y$	12.50	10.0	**$2.0\varepsilon_y$**	25.00	20.0

Figure 31 shows the DIC measured stress vs. strain curves for the room temperature recovery experiments of the 33A (A) and 44A (B) networks. The stress-strain curves identically track for each of the twenty tests up to the individual unloading strains (between 0.1-$2.0\varepsilon_y$), which are indicated by lines dropping from the loading path and returning to a zero-stress value. The specimens with the higher unloading strain show an increase in area within the recovery envelope. This increased area is due to an increased amount of slower recovering anelastic strain, and in the case of post yield experiments, an increase in the amount of residual strain. Comparison of the recovery of the two networks reveals that the 44A network has a lesser degree of strain softening and a less pronounced yield than the 33A. The 44A network also appears to recover a larger amount of strain during the unloading process, an indication of a quicker recovery rate.
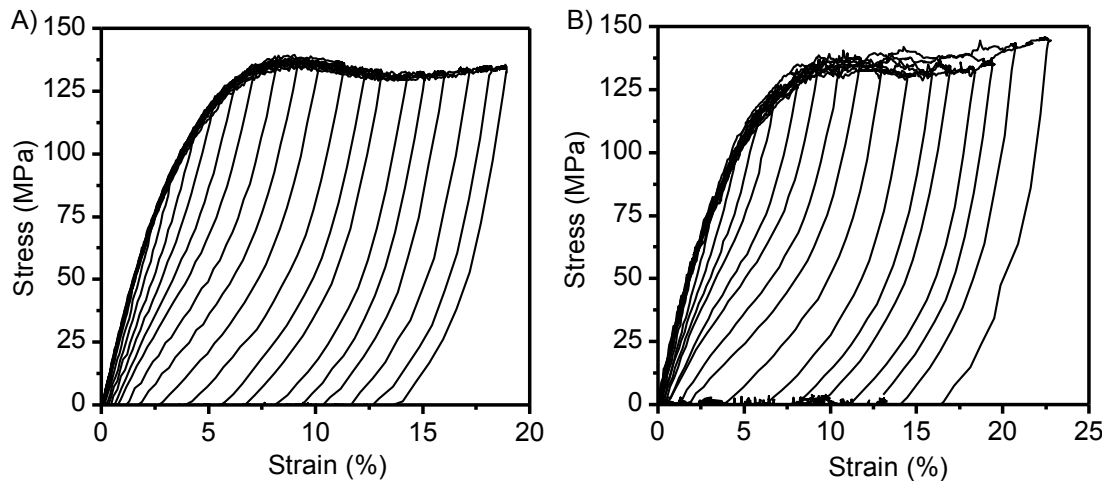
Figure 43. A) DIC Stress vs. strain curves for strain recovery experiments for the 33A network B) 44A network.

The strain vs. time curves for the recovery experiments are seen in Figure 44. The recovery curves for 0.1-$1.0\varepsilon_y$ return to a value at or near zero for both networks indicating no residual strain in the system. Once the unloading strain exceeded the yield, an increase in residual strain was observed continuing to a value of just over 10% for the

33A network. The 44A sample displayed similar pre-yield and post-yield behaviors to slightly less than 15% residual strain at $2.0\varepsilon_y$.
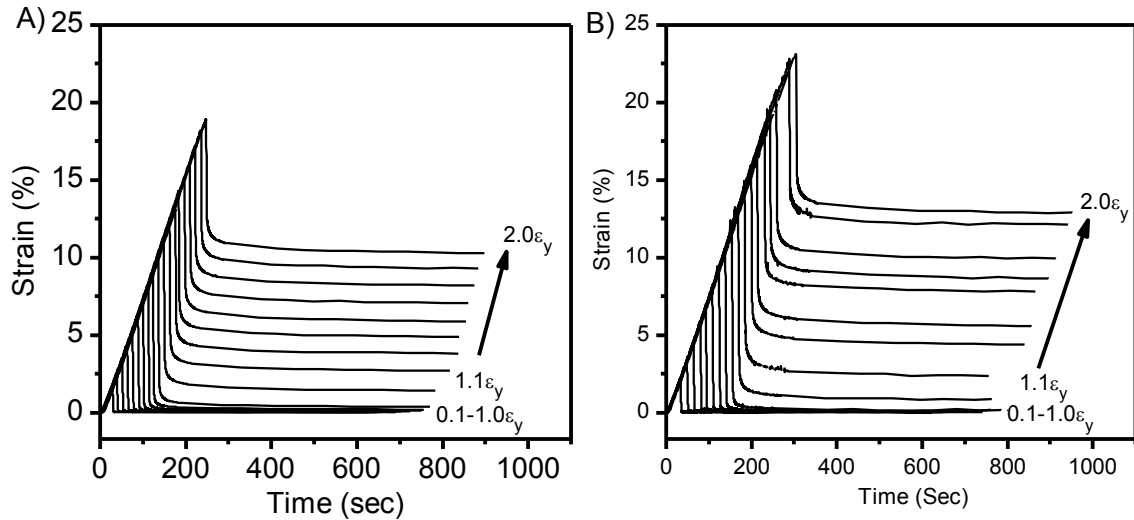
Figure 44. Strain vs. time curves for the 0.1-$2.0\varepsilon_y$ experiments of the A) 33A network and B) the 44A network.

A simple comparison of the recovery rates of the 33A and 44A networks can be seen in Figure 45 where recovery curves from experiments of common peak strains were used. The 44A network shows a significantly higher initial recovery rate than the 33A network, indicating that the 44A network is able to store more energy. This additional energy storage results in a quicker and larger amount of strain recovery. A three term exponential decay function provided a good fit to the initial decay data indicating that at least three processes are involved in the strain recovery.
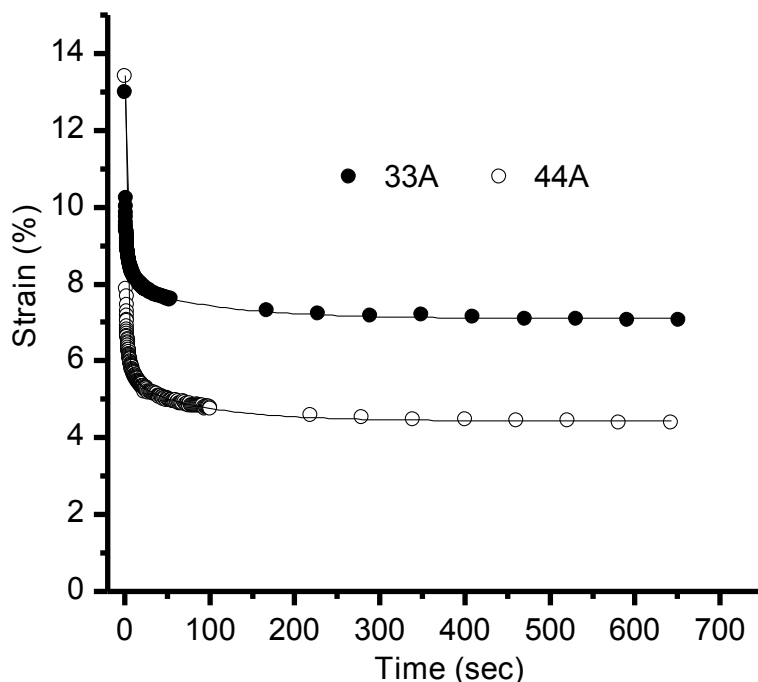
Figure 45. Comparison of initial recovery rates of 33A and 44A.

Effects of Time and Temperature on Recovery

The behavior illustrated in Figure 44 describes 10 minute post unloading strain recovery times. Although a significant portion of anelastic strain was recovered during this period, additional strain was recovered with increased time and/or temperature. To further explore strain recovery, 33A and 44A deformed cylinders were measured by DIC at room temperature after an extended period of time and then placed in an oven at a temperature of Tg-20°C for 1 hour to achieve total recovery of the anelastic strain. Figure 46 shows residual strain data for 33A and 44A, respectively. Each data point in the figure correlates to the amount of residual strain when unloaded at that point in the above stress-strain curve. The time period for extended recovery differs for the two networks as the 44A system was originally tested at an earlier date. However, on a fractional basis the two networks recovered close to the same amount of strain, indicating that the longer time period did not largely influence the results as most room temperature

recoverable strain occurs within the first 30 days. After the room-temperature recovery periods, the specimens were heated to Tg-20°C for one hour in order to recover all anelastic strain. The slopes of the residual strains for the Tg-20°C measurements varied significantly from room temperature. This change in slope indicates activation of secondary recovery processes that would not occur in a reasonable time scale at room temperature. This additional pathway for recovery is seen in both isomer networks, indicating that it is associated with the activation of some molecular motion that is available in both systems. Investigation of the sub-Tg transitions of the two networks in Figure 41B reveals that all glassy state motions are not activated until a temperature of almost 100°C. The most likely contributor to these higher temperature activated motions is the rupturing of hydrogen bonds associated with the HPE segments.[4] When plastic deformation occurs, hydrogen bonds are broken and segments rearrange. Upon removal of the load, most anelastic strain is recovered. However, some anelastic strain is not able to recover as hydrogen bonds reform within the network, trapping in some stored energy. As the temperature is raised, motions in all HPE segments become available and complete anelastic recovery can occur.
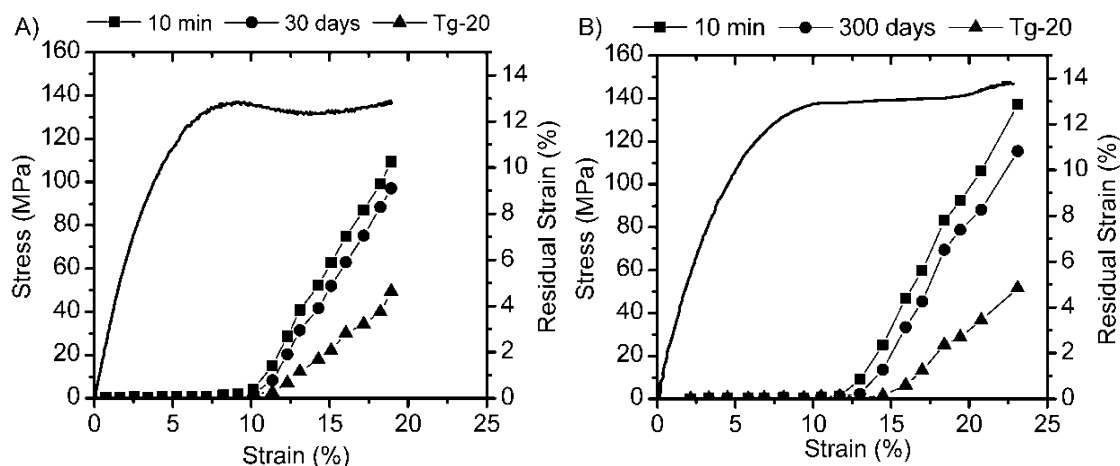
Figure 46. Residual strain plots for 10 minute recovery, extended recovery and Tg-20 recovery.

Quantifying Strain Components

Further DIC analysis of the strain recovery data allows for the quantification of the amount of elastic, anelastic, and residual strains placed on the specimen during loading. Elastic strain is calculated according to Hooke's Law and Theory of Linear Elasticity using the equation $\varepsilon_{elastic} = \sigma_t / E_{ur}$ where E_{ur} is the unrelaxed modulus and σ_t is the stress at the unloading time. Anelastic strain was calculated as $\varepsilon_{anelastic} = \varepsilon_{total} - \varepsilon_{residual} - \varepsilon_{elastic}$ where ε_{total} is the maximum point of the strain-time curve, $\varepsilon_{residual}$ is the measured strain remaining on each test specimen, and $\varepsilon_{elastic}$ is calculated as described previously.

Strain component plots are displayed in Figure 34 for the 10 minute strain recovery and the total sub-Tg recovery. The 10 minute strain component plots (A and B) were developed using the residual strain after 10 minutes, and the total sub-Tg recovery components (C and D) for 33A and 44A networks were determined using residual strains from Tg-20°C values seen in Figure 46. Component plots are shown for the two different recovery periods in order to emphasize the variance that occurs from the time or temperature of recovery. The term "plastic" strain is used loosely in the 10 minute component plots as this component also includes recoverable strain. It is important, however, to realize that the time scale of recovery is important for application to a real world situation where the recovery time and temperature is not the ideal prescription for complete anelastic recovery.
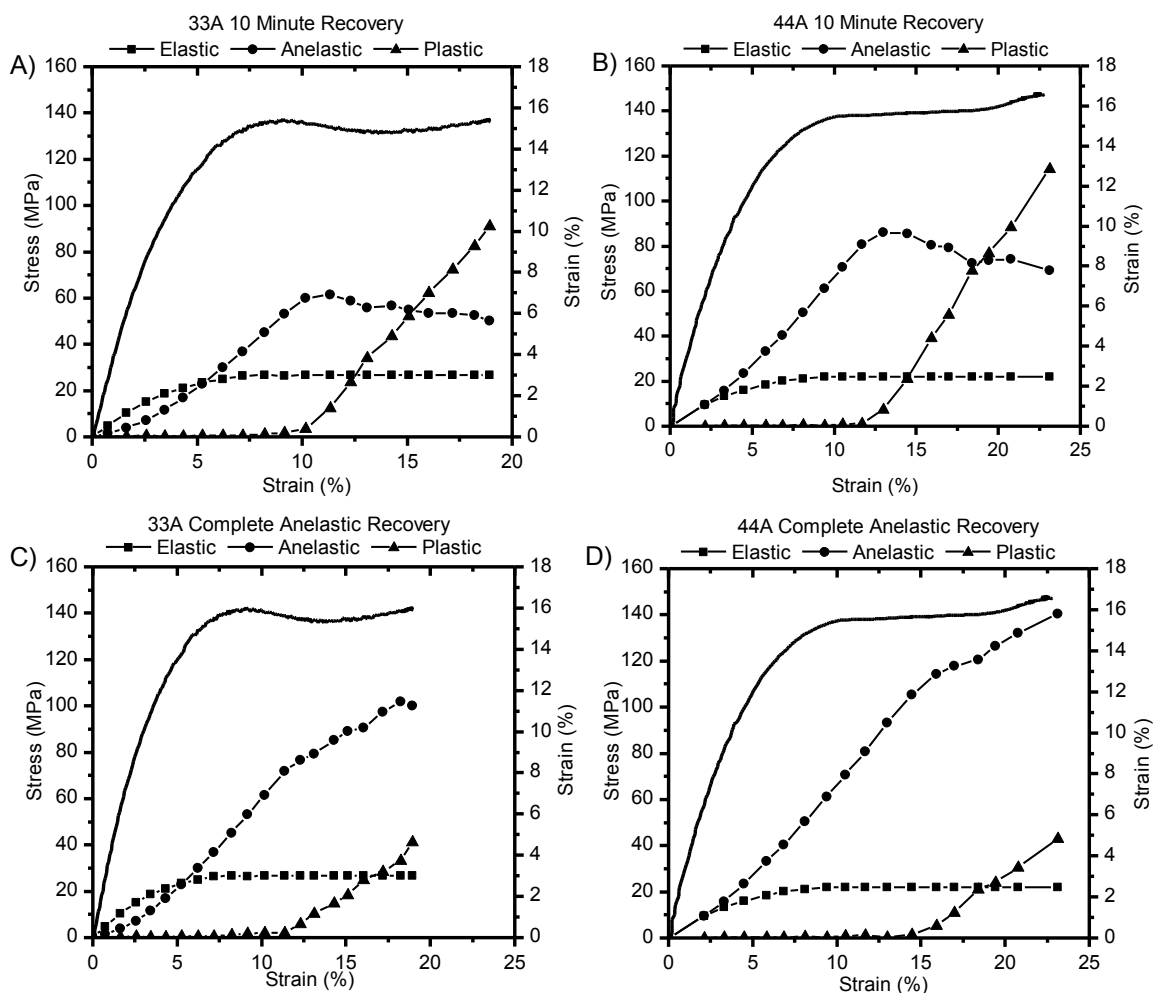
Figure 47. Strain component plots generated for 33A and 44A.

Pre-yield behavior of the 10 minute and complete anelastic recovery component plots is identical due to complete recovery of all strain occurring in less than 10 minutes. Post-yield behavior differs as large segmental rearrangement within the polymer increases the time scale of recovery, and complete recovery is no longer able to occur within 10 minutes. This incomplete recovery is due to the presence of plastic strain and to the introduction of a slower recovering anelastic strain. Reasons for the slower recovering anelastic strain will be discussed in a later section. Further comparison of the 33A and 44A strain behavior will focus solely on the complete anelastic strain recovery component plots in Figure 34C and D.

The general strain development for each network was similar. Elastic strain for the network isomers develops rapidly from onset and plateaus at the stress maxima. Anelastic strain developed immediately upon loading and continued to increase beyond the yield. Anelastic strain became the dominant strain pathway in both network architectures as the total strain exceeded the linear elastic regions. Following the strain softening region, the rate of anelastic strain development decreased in a manner similar to what has previously been reported for linear polymer glasses.[5] Plastic strain developed linearly once the yield point of the individual network was exceeded. Differences in the strain development of the networks exist in the form of initial rate and final magnitude of anelastic strain.

In order to directly compare the development of strain between isomers, 33A and 44A strain components were plotted as a function of the yield strain in Figure 48. Plotting the data in this manner provides insights regarding variances in strain behaviors of the two networks associated with isomer positioning of the DDS curatives. Elastic strains develop at almost the same rate with the maxima varying from differences in the unrelaxed modulus values, suggesting elastic motions remain the same for each network isomer. The data described in Figure 48 also suggests the development of plastic strain is the same for both networks. Assuming elastic and plastic strain components are nearly identical, differences in strain and yield behavior of the two network isomers must be primarily due to the anelastic strain component.
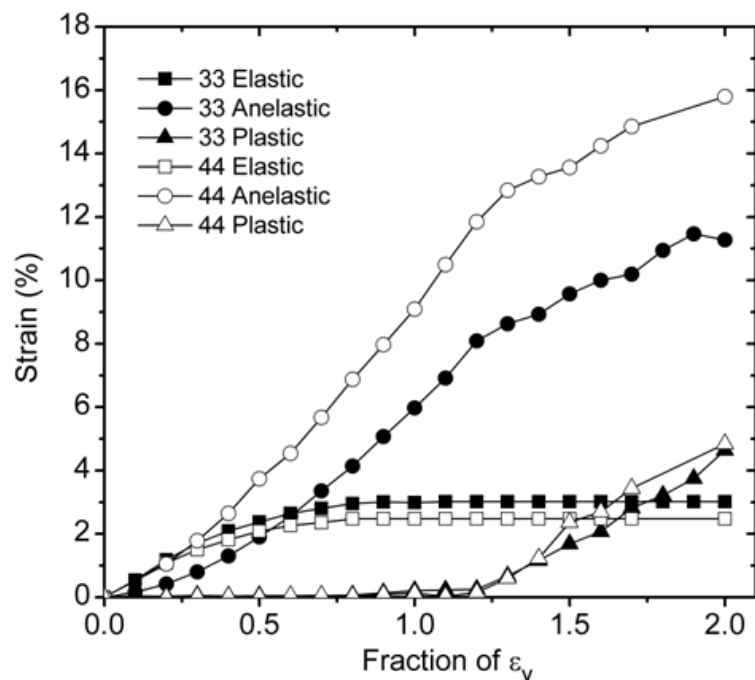
Figure 48. Strain components plotted as a function of the yield strain of the network.

Differences in strain patterns can be explained in terms of glassy state molecular motions. Elastic strain is associated with the intermolecular interactions between neighboring chain segments. Since the chemical compositions of the two isomer networks are identical, molecular interactions for the two networks are the same but must differ in magnitude due to the proximity of neighboring chains. Similar plastic strain behaviors were observed for the post-yield deformations of the isomers and are associated with α-type motions that occur from larger scale segmental flow. Further insights into the similar flow characteristics for the network isomers are seen by the parallel slopes of the post-yield anelastic strain component curves, which suggest anelastic contributions in this region are the same. As a result, variances in the deformation behaviors for the two isomer networks are attributed to the pre-yield anelastic strain development.

Anelastic strain has been attributed to architecture and sub-Tg molecular motions for glassy polymer networks.[6] The DMA results in Figure 41 show clear evidence of differences in sub-Tg molecular motions between $^-$115 – $^+$80°C. The increased anelastic strain for 44A displayed in Figure 48 suggests greater sub-Tg molecular mobility for this isomer, which is confirmed by the larger area in the Tan-δ curve seen in Figure 41. It is also noteworthy to again mention the more prominent bimodal transitions apparent for the 33A isomer, which suggest more restricted glassy state molecular mobility for this polymer.

The meta-linkages in the 33A epoxy isomer provide a higher degree of molecular conformations in the liquid state, resulting in increased density, stiffness and lower Tg upon cooling into the glassy state. Since 44A has lower conformational mobility in the liquid state, the result upon cooling into the glassy state is higher free volume, lower density, lower modulus and higher Tg. Figure 49 shows PALS data used to calculate the average hole size free volume of 44A and 33A as 82 Å^3 and 77 Å^3, respectively, and describes the observed differences in free volume for the network isomers.
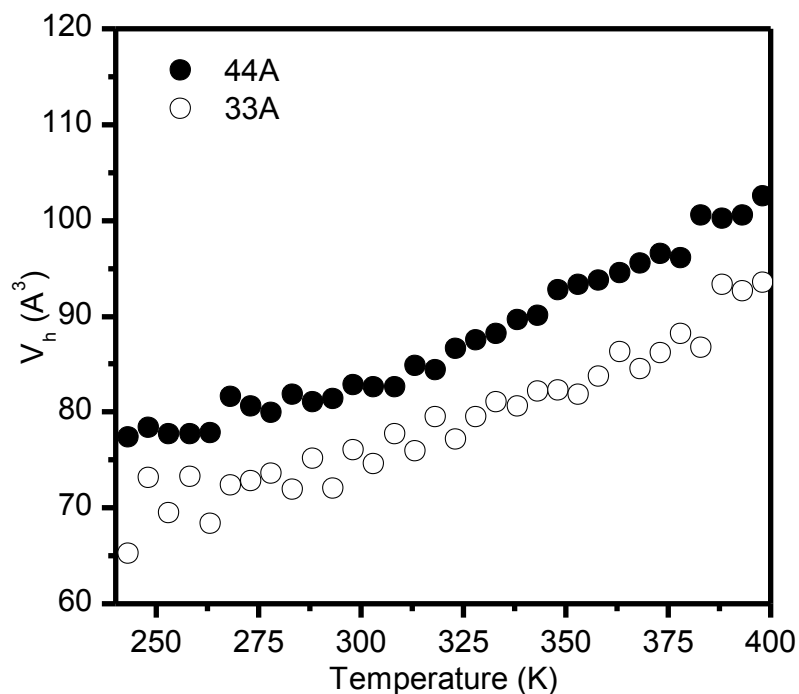
Figure 49. Average hole-size for 33A and 44A.

Differences in sub-Tg molecular motions observed through DMA and free volume between the network isomers provide rationale when considering variances in the elastic, anelastic and plastic strain components observed in Figure 34. The higher elastic component of 33A results from increased modulus driven from a higher packing order, density and lower free volume. As discussed, α-type large segmental motions control plastic deformations, and the isomer networks behave in a similar manner. The specific sub-Tg molecular motions associated with glassy state anelastic deformations for these networks are not fully understood but are most certainly associated with phenyl ring flips, ring librations, methylene vibrations, hydroxyproplyether rotations. [7,43] The availability of more molecular motions and increased free volume of the 44A system leads to the increased anelastic strain development. Anelastic strain has been associated with a small amount of material densification in compression,[8] and there is more available free volume in the 44A system to compact.

The ability of the network to undergo anelastic deformation is essential for storing energy which delays the onset of macroscopic yielding. The 44A network is able to store a higher degree of energy as evidenced through increased anelastic strain. The 33A isomer displays a lower yield strain which is attributed to a reduction in phenyl ring motions from the 33DDS curative. Figure 50 compares the relative ring motions for the 3,3'- and 4,4'-DDS isomers. Comparison of the relative motions for the isomers reveals networks synthesized from 4,4'-DDS contains phenyl-ring flipping motions attributed to its axis of symmetry which contribute to the energy storage capability for this isomer. The meta-substituted 3,3'-DDS lacks an axis of symmetry, reducing ring motions to simple oscillatory librations, which reduces pre-yield energy storage. The shape of the stress-strain curve for 33A is indicative of the impeded ability to store energy as the stress continued to build at a more rapid rate than in the 44A network culminating in lower strain at yield.
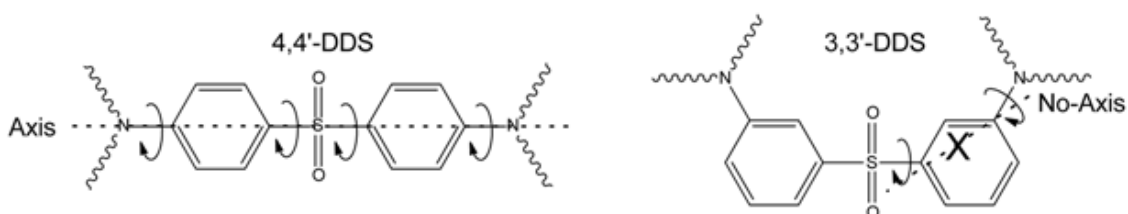
Figure 50. Comparison of phenyl-ring flipping in 33A and 44A networks.

Upon yield, energy is dissipated through longer-range segmental (α-type) motions resulting in strain softening. Figure 51 depicts the segmental rotations envisioned for the 33A isomer. These large rotations exhibit a higher degree of cooperativity with adjacent network segments, analogous to plastic flow, leading to the larger amount of strain softening compared to the 44A isomer. These large rearrangements account for the post-yield variances between the network isomers described in Figure 2.
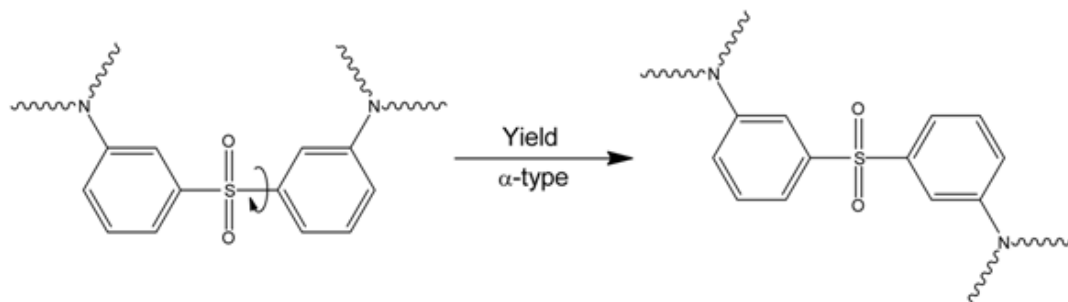
Figure 51. 33A stress dissipation from α-type rearrangement (segmental rotation).

Conclusions

Strain recovery procedures were used for the comparison of curative isomer structure on viscoelastic deformation by the analysis of DGEBA networks cured with both 3,3'-DDS and 4,4'-DDS. The resulting comparison showed that the networks had similar elastic and plastic strain behavior but differing anelastic strain behavior. The similar elastic behavior was due to the common molecular interactions of the chemically identical networks. Likewise, the plastic behavior was the same due to identical chemical composition. Plastic strain occurs by α-type motions, or viscoplastic flow, removing any conformational effects from the different isomers. This leaves the discrepancy in strain behavior to be accounted for by anelastic strain. The 44A system developed anelastic strain at a significantly higher rate prior to yield as it was able to undergo more molecular motions as indicated by DMA tan δ curves of the two systems. The increased molecular mobility of the 44A network arises from the increased para-substitution and from the availability of an axis for phenyl-ring rotations in the 4,4'-DDS segments. The 33A network does not possess this axis of symmetry, displaying less energy storage capabilities. However, the 33A network did show increased energy dissipation post-yield due to segmental rearrangements associated with the 3,3'-DDS curative.

References

1. Shi, J.F.; Inglefield, P.T.; Jones, A.A. *Macromolecules* **1996,** *29,* 605-609.
2. Heux, L.; Halary, J.L.; Laupretre, F.; Monnerie, L. *Polymer,* **1997,** *38,* 1767-1778.
3. Lee, J.Y.; Song, Y.W.; Kim, S.W.; Lee, H.K. *Mater. Chem. Phys.* **2002,** *77,* 455-460.
4. Yurenko, N.A.; Yevtushenko, G.T.; Yermilova, Y.Y.; Shologon, I.M.; Rozenberg, B.A. *Polymer Science USSR* **1984,** *26,* 2867-2872.
5. Quinson, R; Perez, J; Rink, M; Pavan, A. *J. Mater. Sci.* **1996,** *31,* 4387-4394.
6. Sindt, O.; Perez, J.; Gerard, J.F. *Polymer* **1996,** *37,* 2989-2997.
7. Ochi, M.; Shimbo, M.; Takaskima, N.; *J. Polym. Sci.* **1986,** *23,* 2185.
8. Kung, T.M.; Li, J.C.M.; *J. Mater. Sci.* **1987,** *22,* 3620.

CHAPTER V

EFFECTS OF DGEBA EQUIVALENT WEIGHT ON DEFORMATION IN NETWORK

ISOMERS

Introduction

In the previous chapter, the effects of isomerism on network properties were explored by investigation of amine isomerism in low molecular weight DGEBA based networks. Networks cured by the para-substituted 4,4'-DDS displayed a higher level of sub-Tg molecular motion, resulting in a higher level of energy storage through anelastic strain. The goal of this chapter is to further explore the effects of isomerism on mechanical performance, through the investigation of isomer networks of varying crosslink density. While the effects of varying crosslink density on epoxy network properties have been studied extensively, this work seeks to further the knowledge by also investigating isomer networks at each level of molecular weight between crosslinks, M_c. As was discussed in the introduction, crosslink density can be modified in multiple ways including changing monomer functionality,[1,2,3,4] changing monomer molecular weight,[5] changing the stoichiometric ratio,[6,7] or altering the network cure profile.[8,9] Trends that have been shown include increased modulus and yield stress with increased crosslink density.[1,65] It has also been shown that as M_c increases, the T_g decreases, leading to a tougher resin system described as having an "increase in deformability."[10] The crosslink density of epoxy networks has also been shown to affect sub-T_g motions with higher crosslink densities resulting in more cooperativity between neighboring segments.[11]

Variations in crosslink density in this work were obtained by changing the linear molecular weight of the DGEBA resin. An increase in resin equivalent weight (EW)

results in an increase in the measured molecular weight between crosslinks of the network. The study of isomerism effects on deformation was continued through the use of 3,3'- and 4,4'-DDS at each equivalent weight. Mechanical and thermomechanical properties were measured for each network, and differences in performance were related to available motions of the individual networks. Lastly, strain recovery was explored on the highest EW networks to compare to the 33A and 44A networks from Chapter IV.

<div align="center">Materials</div>

Epoxy resins were that of varying equivalent weights of diglycidyl ether of bisphenol-A (DGEBA). Resins were supplied by Hexion Specialty Chemicals Company under the trade names of EPON 825 (175 g/mol equivalent weight), EPON 830 (195 g/mol equivalent weight), EPON 834 (245 g/mol equivalent weight) and EPON 1001F (540g/mol equivalent weight). From this point on, these resins will be referred to by their equivalent weights, as EW175, EW195, EW245 and EW540. These systems were cured using either 3,3'-diaminodiphenyl sulfone (33DDS, 97% purity) or 4,4'-diaminodiphenyl sulfone (44DDS, 97% purity), which were purchased from Sigma Aldrich and used as received. Chemical structures for the raw materials are provided in Figure 1.
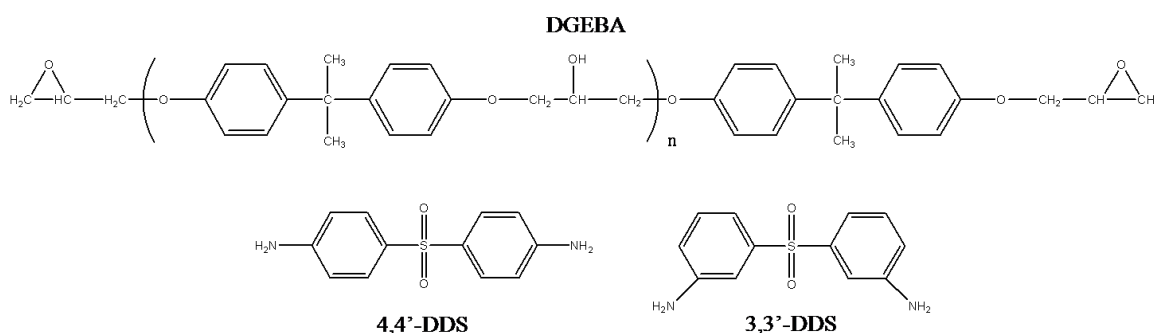
Figure 52. Chemical structures for DGEBA and DDS monomers.

Results

Comparison of 33DDS vs. 44DDS and Varying Epoxy EW

Changing the molecular weight of the DGEBA network correlates directly to an alteration of the mechanical performance of the network. Figure 53 shows stress vs. LVDT measured strain curves for the 8 networks of varying equivalent weight DGEBA cured with 3,3'-DDS (A) and 4,4'-DDS (B). A clear trend is seen in both 3,3'- and 4,4;-DDS networks as an increase in DGEBA equivalent weight results in a reduction of mechanical performance. This stress-strain curves show a clear step down with increasing equivalent weight, resulting in decreases modulus, yield stress, and yield strain. A reduction in glass transition temperature of the networks is also seen with increasing DGEBA equivalent weight. Table 2 shows the compressive mechanical properties for the eight differing systems.
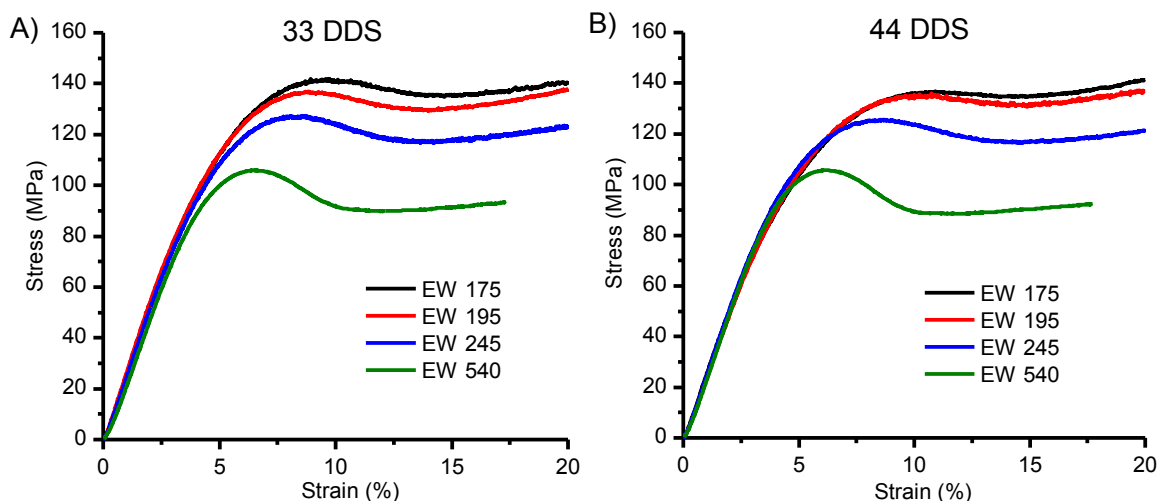
Figure 53. Stress-strain curves for varying equivalent weights cured with 33DDS (A) and 44DDS (B).

Table 11. Compressive Mechanical Properties of Varying EW Networks

		Modulus (MPa)	Yield Stress (MPa)	Yield Strain (%)
33 DDS	EW 175	2886	141.65	9.16
	EW 195	2867	137.37	8.92
	EW 245	2725	126.92	8.05
	EW 540	2626	105.38	6.53
44 DDS	EW 175	2728	137.01	10.89
	EW 195	2614	135.16	9.86
	EW 245	2726	125.10	8.42
	EW 540	2655	105.56	6.32

A distinct difference is also seen in the post-yield behavior of the stress-strain curves as the higher equivalent weight resins show an increased amount of strain softening. Strain softening is indicative of the network's ability to dissipate applied stress. Higher equivalent weight resins show a decreased yield stain due to a lower resistance to stress induced flow. Once stress induced flow begins, less stress is required to maintain it. The post-yield behavior of the EW540 networks resembles that of linear polymer glasses as the stress decreases significantly before leveling off to a near constant value. In linear polymer glasses, this is indicative of propagation of locally strained regions.

At low equivalent weights, epoxy systems cured with 3,3'-DDS possess a higher modulus, higher yield stress, and lower yield strain. This difference in properties can be related to the increased conformations introduced from the meta-substituted amine, allowing for tighter chain packing when cooling from the liquid to glassy state.[12] The better chain packing reduces free volume resulting in higher modulus values, yield stresses, and lower yield strains for the 3,3'-DDS systems. However, the discrepancy in mechanical performance of the isomer networks decreases as the equivalent weight of

DGEBA increases. Plots showing the relationship of these key properties to equivalent weight are seen in Figure 54.
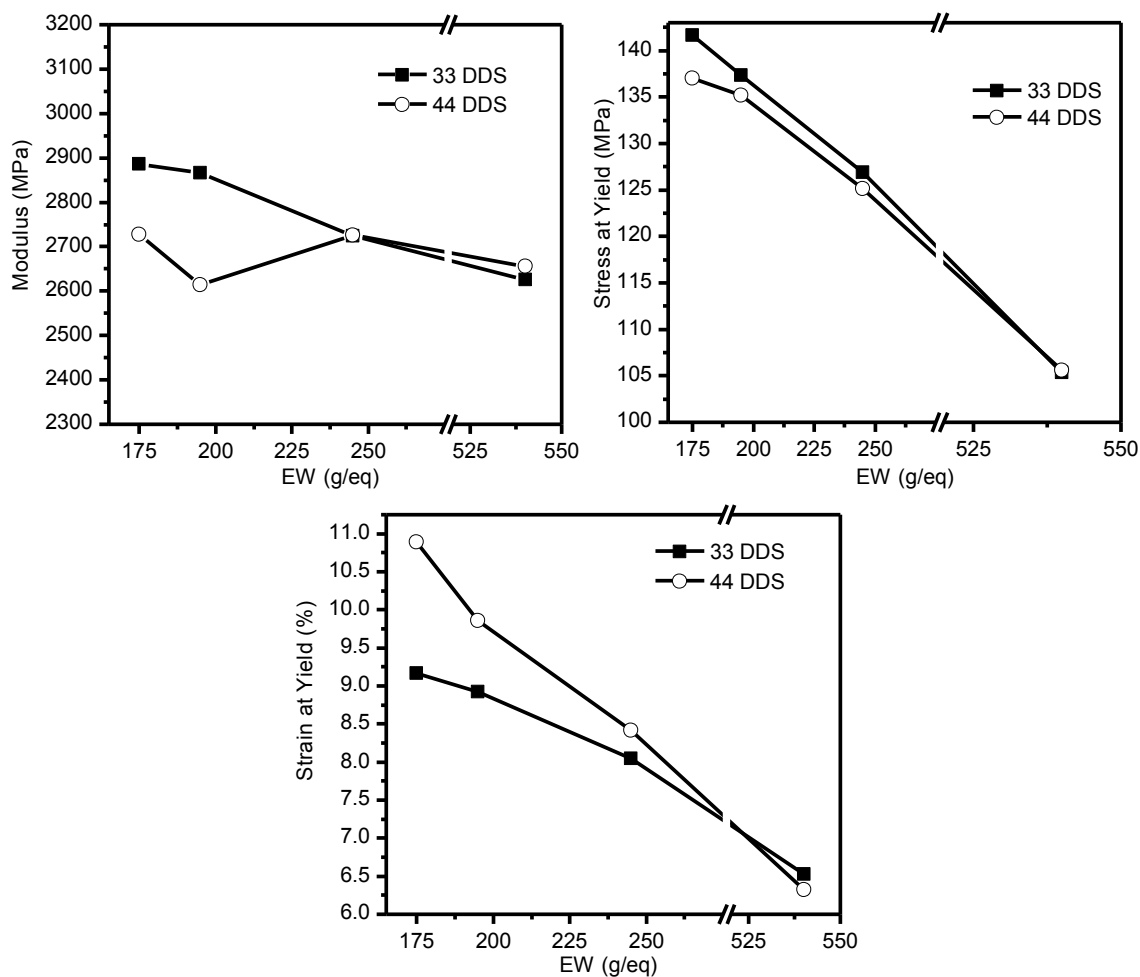
Figure 54. Effects of equivalent weight on mechanical properties of epoxy-amine systems: Modulus (left), Stress at Yield (center), and Strain at Yield (right)

The trend plots shown in Figure 54 show a clear reduction of the effects of isomerism on mechanical performance with increasing equivalent weight. This trend indicates that as the length of linear DGEBA segments increases, the packing arrangements upon cooling from the liquid to glassy state are no longer greatly affected by the curative structure. Part of this reduction of isomerism effects is due to the decreased concentration of amine segments within the network. Formulations were kept at a 1:1 ratio of epoxide to amine reactive hydrogen, resulting in higher epoxy

concentrations as the equivalent weight increased. Density values of the epoxy networks

also decreased as epoxy equivalent weight increased indicating a reduced packing

efficiency in higher molecular weight resins. Therefore, as weight increases, the packing

arrangements of the network become primarily controlled by the epoxy linear segments

due to the higher epoxy concentration and due to the appearance of a decreased packing

efficiency. Figure 55 provides a comparison of stress-strain curves for the EW175 and

EW540 DGEBA resins. The EW175 isomer networks show a clear difference in

behavior while the EW540 isomers behaved nearly identically.
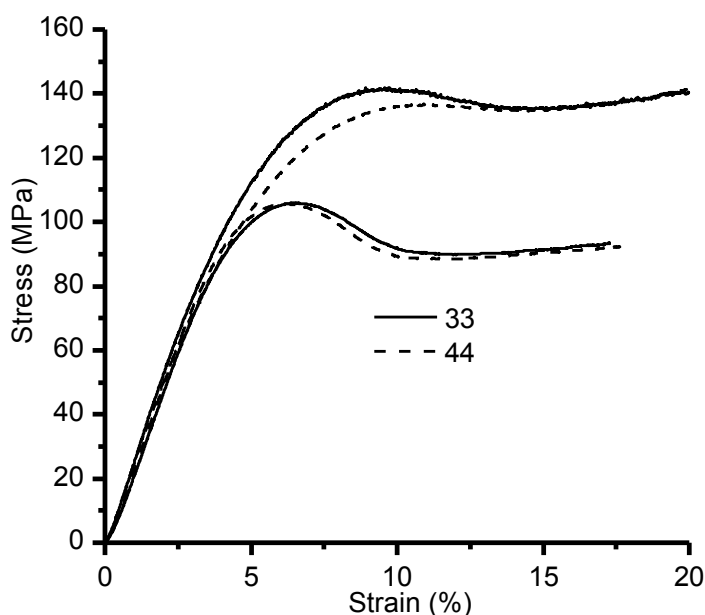
Figure 55. Stress-strain curves for EW175 and EW540 resins cured with 3,3'- and 4,4'-DDS.

The results in displayed in Figure 54 all fit the trend of converging properties with

the exception of the EW195-44 system, which showed a lower modulus than the EW175-

44, EW245-44, and EW540-44 systems. This discrepancy arises from the difficulty in

controlling cure state of 4,4'-DDS cured systems. Figure 56 shows isothermal DSC

results of 200°C curing reactions for 3,3'- and 4,4'-DDS systems. The 3,3'-DDS systems

show no evidence of exothermic reaction after 60 minutes while 4,4'-DDS systems show

continued exothermic heat release for almost 180 minutes at 200˚C. However, as

conversion is driven up for these 4,4'-DDS cured networks a decrease in modulus occurs.

Figure 57 shows stress-strain curves for EW175-44 at three different post-cure times (1,

2, and 3 hours). The curves show a clear change in line-shape for the specimens post-

cured longer than 1 hour. The change in line shape reveals a reduction in modulus of the

system and an elimination of strain softening, resulting in an indistinguishable yield

point. Such a distinct change in performance suggests a change of chemical structure of

the network. A likely explanation for these results is that further conversion, at times

exceeding 1 hour, occurred through etherification, not through epoxy-amine reactions.

Etherification results in a tougher behavior pre-yield due to the introduction of more ether

segments in the network, thereby explaining the lower modulus. The decreased strain

softening post-yield occurs due to a reduction of the molecular weight between crosslinks

of the network. Shorter linear segments within the network reduce the amount of

available flow upon yielding.
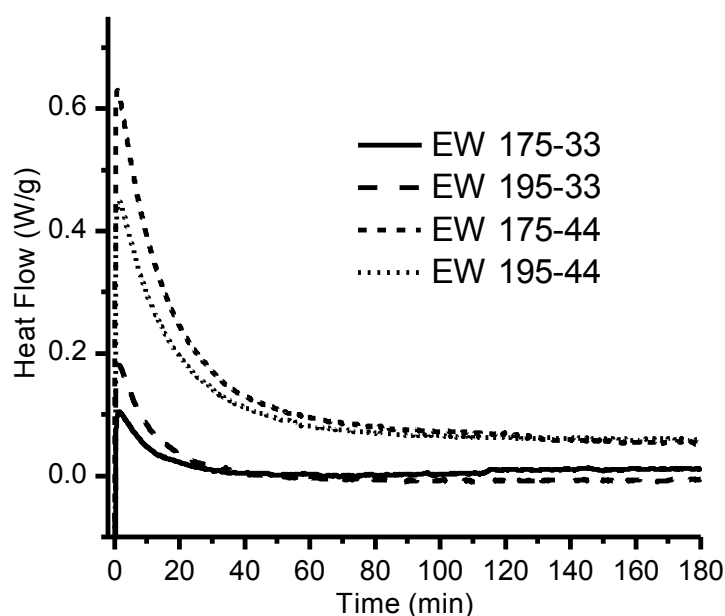
Figure 56. 200ºC isothermal DSC for epoxy-amine systems showing longer periods of exothermic energy release for 44DDS cured systems.
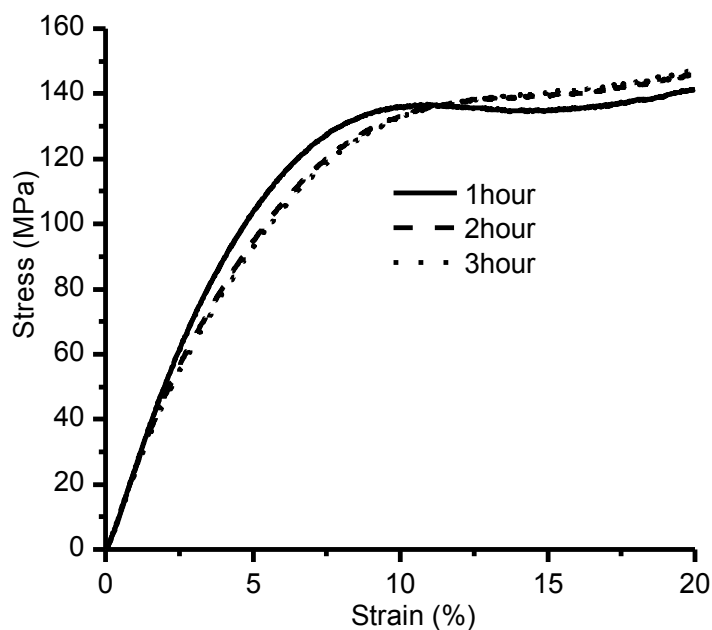
Figure 57. Stress-strain curves for EW175-44 post cured for 1, 2, and 3 hours.

Thermomechanical Behavior

Further insights to the effects of DGEBA equivalent weight were gained by investigation of the thermomechanical properties of the various networks. Figure 58 shows DMA E' and Tan δ curves for the 8 networks of varying equivalent weights and isomer structures. Modulus curves track similarly with cold temperature modulus values in the 4000-6000 MPa range. Glass transition temperatures differ significantly as seen in the E' and Tan δ curves with T_g decreasing as equivalent weight increases. The decreased isomer effect on properties is also illustrated in thermomechanical behavior as α-transitions for isomer networks become similar as equivalent weight increases with the EW245 and EW540 isomers showing almost identical transitions.
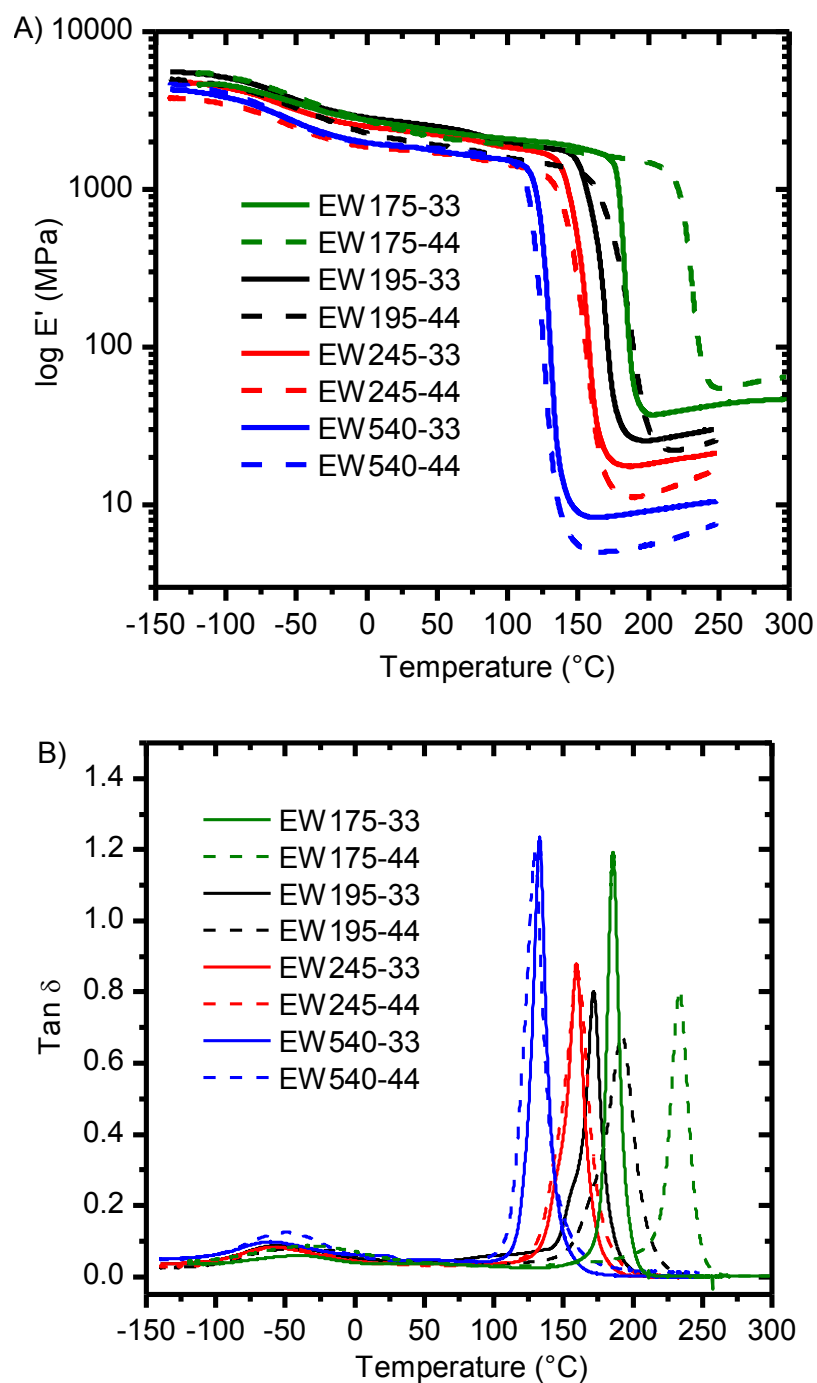
Figure 58. DMA E' (A) and Tan δ (B) curves for varying EW networks.

Rubbery modulus values were taken from the post-T_g plateau for each network

and used to calculate the molecular weight between crosslinks, M_c, for the DGEBA-DDS

networks. Table 12 shows rubbery modulus, density and molecular weight between

crosslink (experimental and theoretical) values for the varying equivalent weight

networks. $M_{c,exp}$ was calculated based on the theory of rubber elasticity from:

$$M_{c, exp} = 3\rho RT/E' \hspace{3cm} \text{Equation 10}$$

where ρ is the network density, R is the universal gas constant, and E' is the rubbery

modulus at the temperature, T.[13],[14] $M_{c,the}$ was calculated by monomer molecular weights:

$$M_{c, the} = \frac{(m_a + 2m_e)}{3} \hspace{3cm} \text{Equation 11}$$

where m_a is the amine molecular weight and m_e is the epoxy molecular weight.

Table 12. M_c Data for Varying EW Epoxy Networks

System	E'$_r$ (MPa)	Density (g/ml)	$M_{c, exp}$ (g)	$M_{c, the}$ (g)
EW175-33	37.2	1.237	394.1	316.1
EW175-44	54.8	1.239	297.3	316.1
EW195-33	25.47	1.239	571.6	329.2
EW195-44	22.13	1.236	685.8	329.2
EW245-33	17.56	1.226	801.6	386.4
EW245-44	11.18	1.227	1262.2	386.4
EW540-33	8.29	1.165	1528.6	802.8
EW540-44	5.04	1.157	2500.5	802.8

Experimental M_c values exceeded theoretical values in all cases with exception of

the EW175-44 system. A M_c value in excess of the theoretical value indicates residual

functionality within the cured network. This is expected as it is practically impossible to

react all epoxy and amine groups in a thermoset network. However, the experimental

values for M_c are in significant excess with the EW195-44, EW245-44, and EW 540-44

exceeding twice that of the theoretical value. This high excess over theoretical values

suggests that networks are significantly under cured. Due to the unlikely nature that

>25% of the functional groups remain, an alternative explanation must be used. The

equivalent weights of the epoxy resins are an average with individual DGEBA chains

having differing degrees of polymerization. It is plausible based on the values of M_c to

assume that the rubbery state properties are being dominated by the longer DGEBA chain segments as these segments take less stress to induce flow within. The small amplitude of the DMA test does not allow for complete extension of these longer segments resulting in the tighter bound segments remaining dormant and not playing a role in the deformation event. This leads to an overestimation of the M_c for the network. The EW175 networks do not display this trend of vast overestimation, due to a low poly dispersity index (PDI). As the equivalent weight increases, so does the PDI leading to the increased disparity between theoretical and experimental M_c values. Networks cured with 4,4'-DDS display a higher M_c value compared to 3,3'-DDS networks, due to a reduced conversion as illustrated by the DSC results in Figure 56. The EW175-44 network is the only network that does not display a M_c value in excess of the theoretical value. This discrepancy is a result of the significantly higher temperature value for the rubbery plateau. Any residual epoxy groups within the network will readily react with secondary hydroxyls as the temperature exceeds 200°C resulting in a rapid reduction of the M_c.

Additional insights into the behavior of the networks can be found by investigating the transitions displayed in the Tan δ curves of Figure 58. The glass transition, or α-transition, temperature decreases with increasing DGEBA equivalent weight, an expected behavior as the crosslink density of the network is decreasing. The behavior of the sub-T_g transition(s) also differs between networks. Figure 59 shows DMA Tan δ curves enlarged to show the sub-T_g transitions for the varying equivalent weight networks while

Table **13** shows the temperatures for the peak centers of both the α- and β-transitions along with the respective areas of each. There appears to be a loose trend of decreasing temperature and increasing area for systems with higher DGEBA equivalent weight. The bimodal nature of the sub-T_g transitions makes it difficult determine exact temperatures of the transitions, particularly in the 4,4'-DDS cured networks, but the general trend of shifting towards lower temperatures with increasing EW is evident. Similar results were seen by Imaz et al. in TGDDM based isomers of varying crosslink density.[15] The increase of area of the sub-T_g peak is evidence of increased cooperative motions within the systems containing higher EW DGEBA.
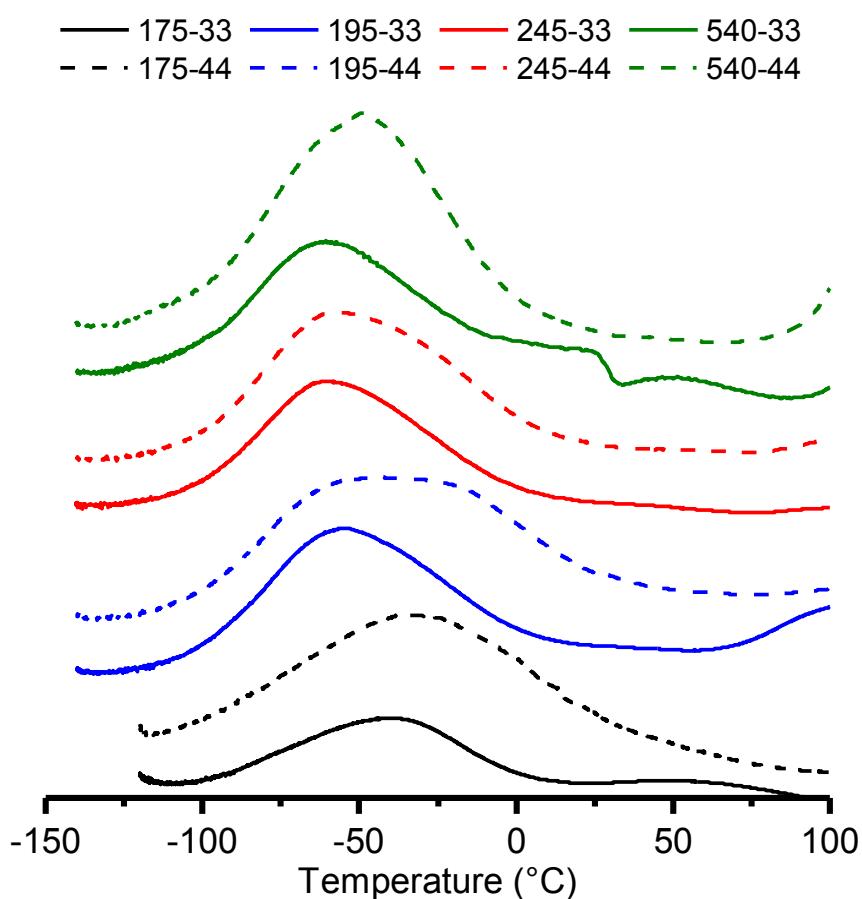
Figure 59. DMA Tan δ sub-T_g transitions.

Table 13. Temperatures and Areas of α- and β-transitions

System	T_α (°C)	Area	T_β (°C)	Area
EW175-33	185.5	15.11	-38.7	2.31
EW175-44	233.5	16.37	-29.9	4.23
EW195-33	171.8	17.24	-54.7	3.12
EW195-44	191.6	20.72	-46.8	4.30
EW245-33	159.4	17.1	-60.0	2.83
EW245-44	160.2	22.27	-58.1	3.75
EW540-33	132.8	18.39	-60.7	4.13
EW540-44	129.3	23.98	-49.0	5.28

In all sets of network isomers, the 4,4'-DDS cured network possesses a larger area and higher temperature. The larger area suggests more cooperative motion within these networks, particularly in situations where conversion is not complete. The increase in peak center is a product of the more prominent bimodal distribution for 4,4'-DDS networks. While the mechanical behavior between isomers becomes more similar as EW increases, the molecular motions indicated by DMA remain different. It is likely that the advantages of the increased molecular motions of the higher EW 4,4'-DDS networks are not realized in compression due to the low yield stress required to induce flow in the long linear DGEBA segments.

Strain Recovery

Strain recovery experiments were conducted on the EW540 networks in order to investigate the mechanisms for strain development and recovery in networks with high M_c values. Figure 60 shows stress vs. DIC measured strain for the recovery experiments of the EW540-33 and EW540-44 isomer networks. Curves appear with more noise than what was seen in the prior recovery experiments discussed in Chapter IV, due to lower overall stress values. Severe strain localization created complications with speckle patterns preventing data collection for higher strained specimens.
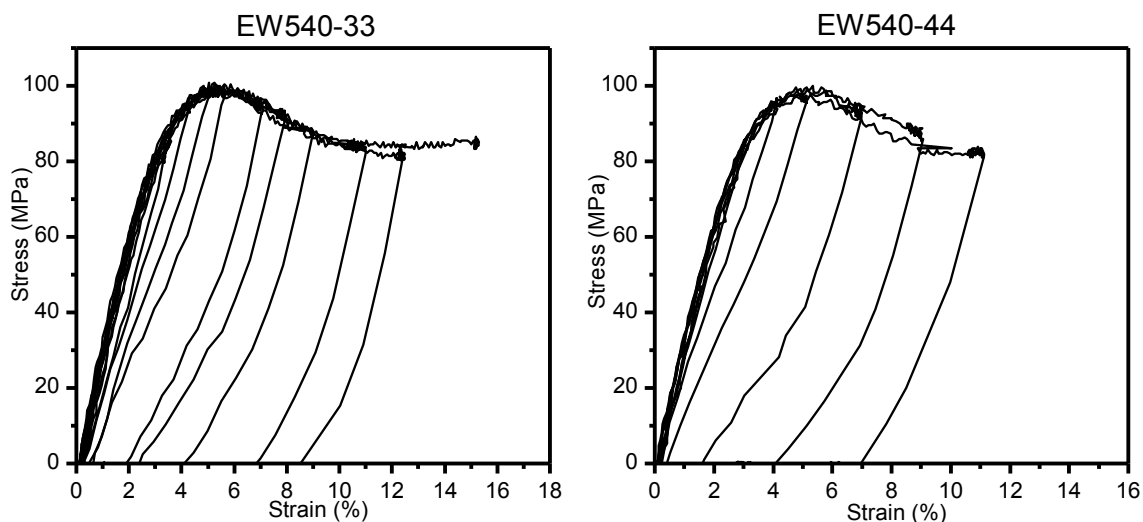
Figure 60. Stress vs. DIC strain for EW540 strain recovery experiments.

A notable trend in the EW540 recovery experiments is the rapid recovery of strain for the pre-yield experiments with total strain returning to zero immediately during the unloading process. Figure 61 shows the DIC measured strain vs. time plots for the EW540 recovery experiments, again illustrating the rapid recovery in pre-yield recovery tests. Post-yield experiments show increased residual strain like the experiments discussed in Chapter IV. However, the EW540 networks do not appear to recover a large portion of the strain that was applied during loading, suggesting increased energy dissipation compared to energy storage.
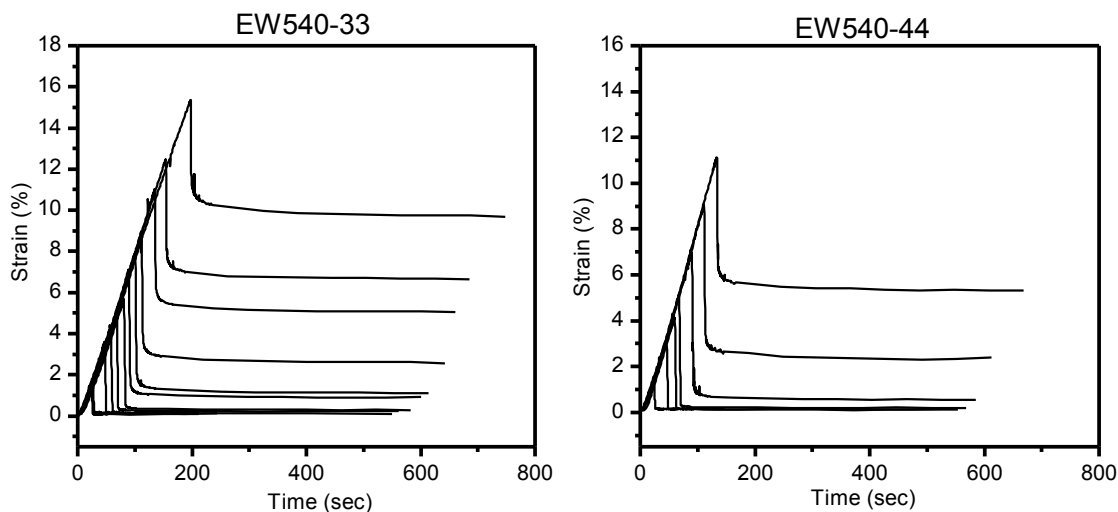
Figure 61. DIC strain vs. time for EW540 strain recovery experiments.

Elevated temperature recovery was conducted at three different temperature stages of 50, 70, and 90°C. The small range of elevated temperature recovery was due to the low glass transition temperatures of the EW 540 networks. Temperatures were selected based on DMA Tan δ seen in Figure 62 in which the onset of α-type motions occurs at 100°C. Elevated temperature anelastic strain recovery experiments must occur at a temperature below this point in order to avoid the simultaneous recovery of plastic deformation. Additional analysis of recovery at elevated temperatures was conducted by differential scanning calorimetry (DSC) experiments of highly deformed resin. Figure 63 shows a DSC temperature sweep of EW540 specimens that were deformed to 20% strain. DSC specimens were cut from the heart of the localized strain region and heated at a rate of 10°C/min through their glass transition temperatures. The resulting thermograms show a clear exothermic peak resulting from elevated temperature recovery of anelastic strain. Exothermic peaks are associated with the release of stored energy from the network.[16]
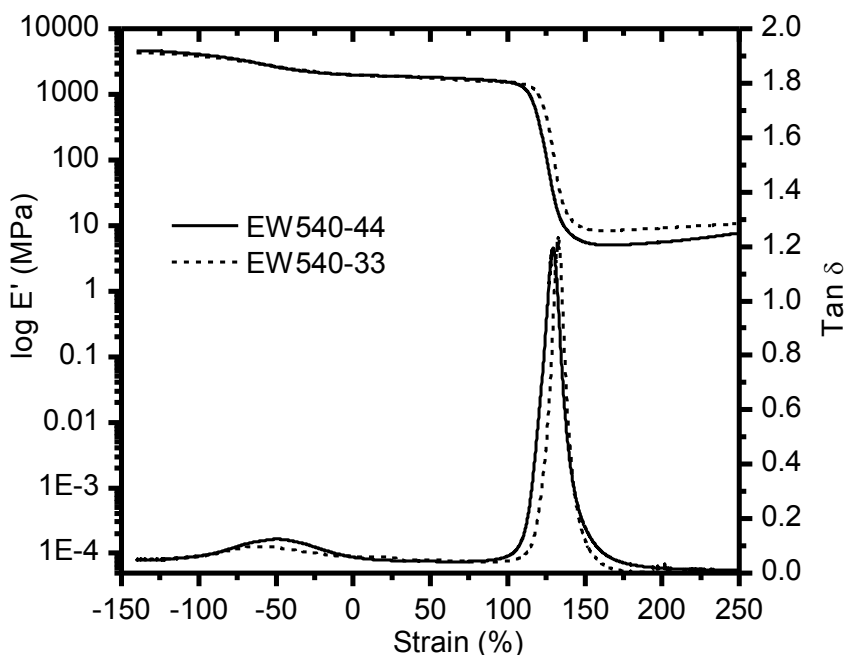
Figure 62. DMA results for EW540 isomer networks.
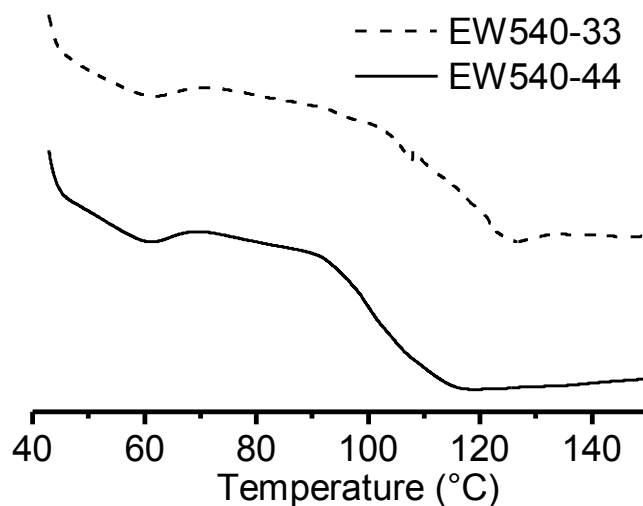
Figure 63. DSC recovery of anelastic strain for EW540 networks.

The large exothermic peak in Figure 63 leads to the prediction that a large amount

of anelastic strain will recover at elevated temperatures. However, the residual strain

plots in Figure 64 show only a small amount of additional recovery upon thermal

treatment of the EW540 networks. This lack of elevated temperature anelastic strain

recovery is due to the low concentration of residual anelastic strain within the network

due to the highly localized strain development post-yield. The specimens used for DSC were taken directly from the highly deformed region and, thus, contained a larger concentration of deformed material compared to the bulk cylinder. A more detailed discussion on strain localization will follow in a subsequent section.
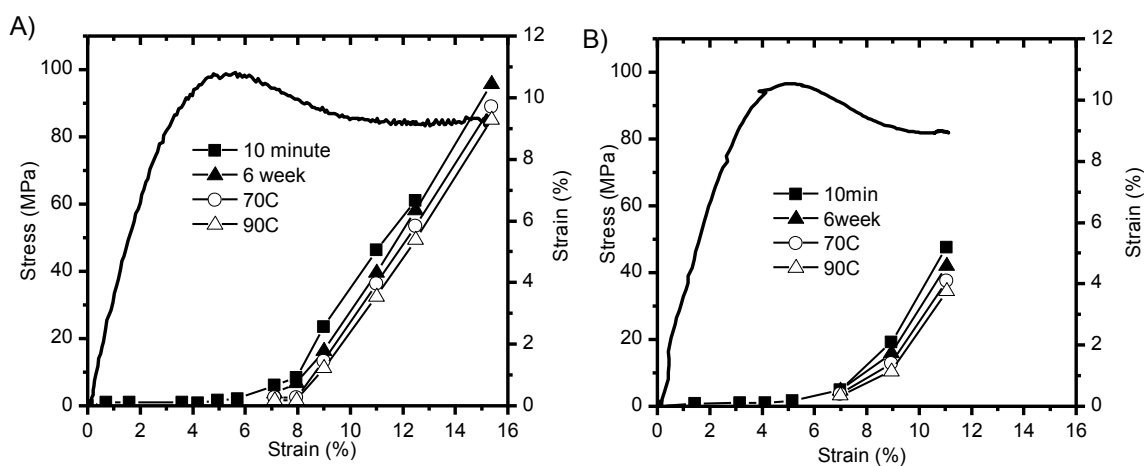
Figure 64. Residual strain plots for recovery experiments of EW540 networks.

The residual strain plots in Figure 64 show the residual strains after 10 minutes and 6 weeks at RT and after elevated temperature treatment at 70 and 90°C. Thermal treatment at 50°C yielded no additional strain recovery and was not included in the plot. Comparison of the results of EW540-33(A) and EW540-44(B) indicates similar behavior for the two networks, as was expected based on the similarity of their stress-strain curves. The development of plastic strain occurs at a very rapid rate in the EW540 networks with plastic strain increasing from a value near zero at 8% total strain to a value of 9.3% at 15.4% total strain. This rapid development suggests that a large amount of anelastic strain within the network is converted to plastic strain shortly after the material yields. It is also interesting to note that plastic strain development is not seen until values well past the peak in the stress-strain curve.

Strain component plots based on the residual strain values following treatment at 90°C can be seen in Figure 65. The two networks show almost identical strain development behavior with elastic strain initially being the dominant strain mechanism, followed by anelastic strain becoming dominant as the total strain exceeded 4%, and plastic strain becoming dominant at higher strains (>12% total strain). The behavior of the EW540 networks is significantly different from what was seen in the EW175 networks discussed in Chapter IV as anelastic strain reaches a maximum post-yield and subsequently decreases. The decrease in anelastic strain coupled with the rapid development of plastic strain and the post-yield stress drop in the stress-strain curve suggests that stress is rapidly dissipated once the onset of plastic deformation occurs.
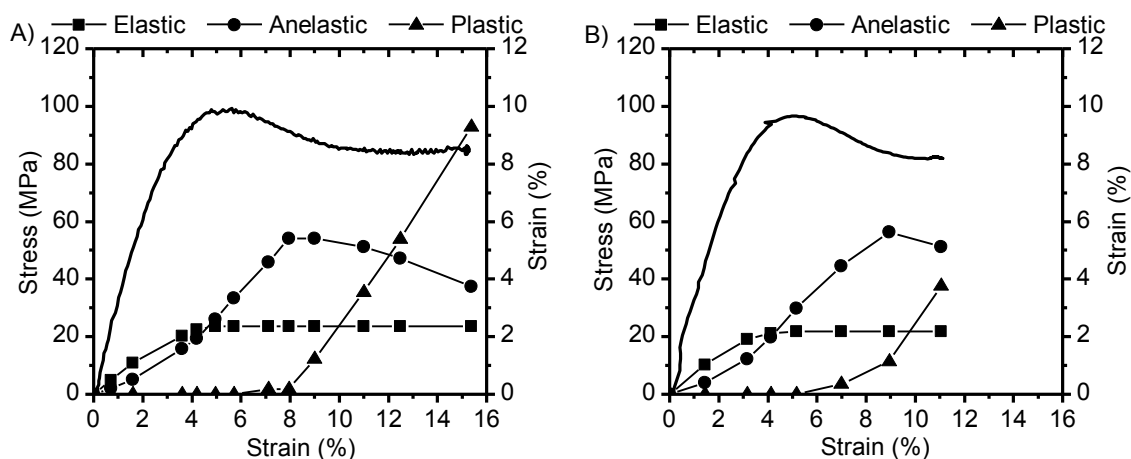
Figure 65. Strain component curves for EW540-33 (A) and EW540-44 (B).

Strain maps were used to further investigate the strain development within the EW540 networks. Figure 66 shows four strain maps for a EW540-33 specimen taken to ~11% total strain. The four stages of strain maps show the distribution of strain initially (1), at yield (2), at peak strain near 11% (3), and after recovery (4). Histograms show the relative concentrations of strain for each of the strain maps, and stage points display the local strain at two points on the cylinder during the deformation and recovery process.
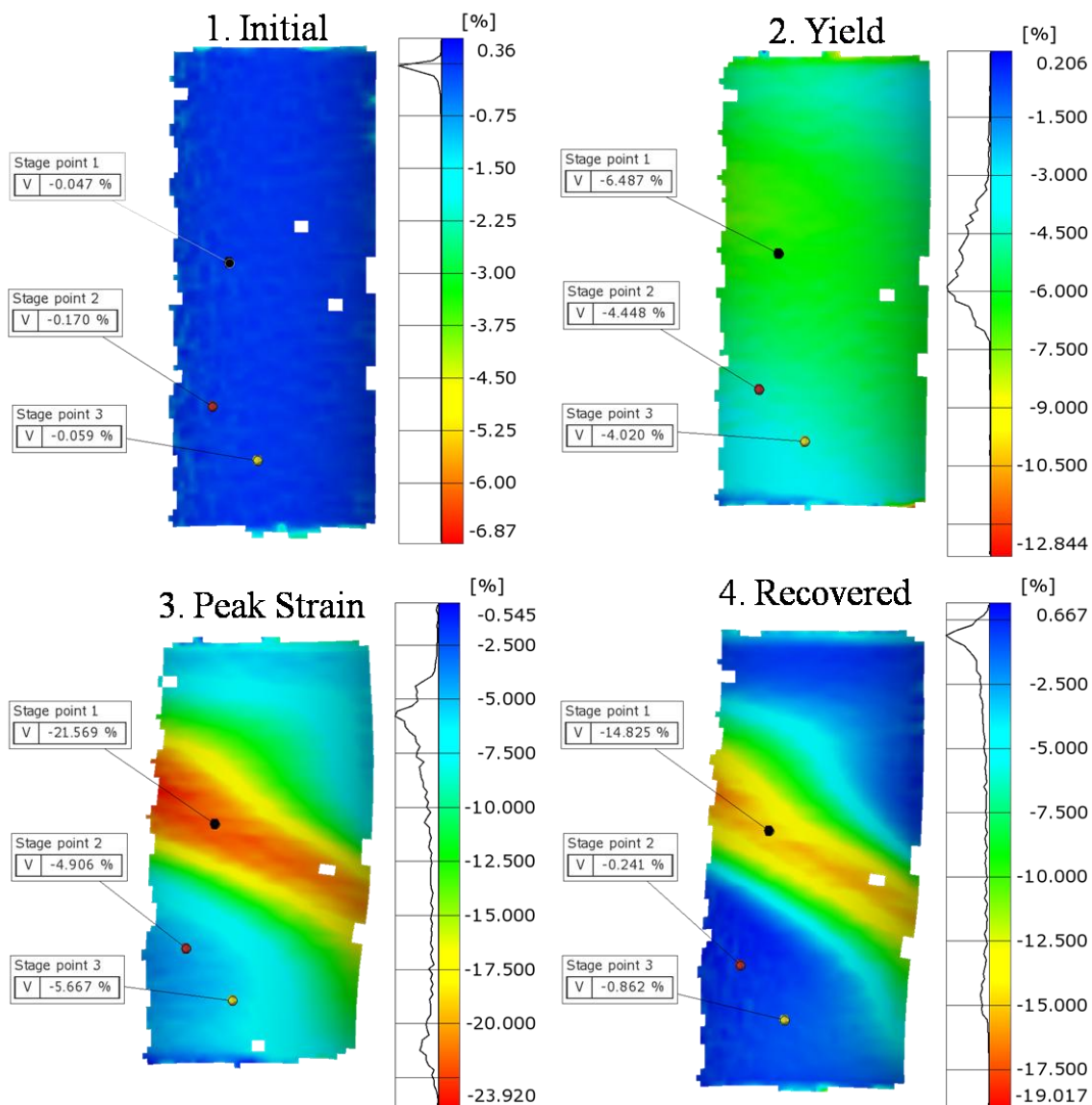
Figure 66. Strain maps for EW540-33 taken to ~11% total strain.

The strain maps in Figure 66 illustrate the extreme strain localization that is responsible for the post-yield deformation behavior of the EW540 networks. The initial strain map (1) shows uniform strain across the surface. However, at yield (2), strain is no longer uniform and begins to develop rapidly in a localized region as seen by the strain map at peak strain (3). Following the unloading process (4), the majority of the cylinder returns to its original state while the region of highly localized deformation retains a large amount of strain. Figure 67 shows the compressive strain at the three labeled stage points

of the cylinder during the loading and recovery process where the dotted lines represent the times associated with the strain maps seen in Figure 66. The large difference in strain rates of the stage points illustrates the effect of localized strain development on bulk cylinder deformation. Strain development in the non-yielded regions slows drastically, and in some areas, development ceases, and a small amount of recovery occurs (stage point 2). Meanwhile, in the locally yielded regions (stage point 1) strain develops at a rate that is significantly faster than the applied strain rate. The net result of this increased localized strain rate is a decreased strain rate in some areas (stage point 1) and an alleviation of strain in others (stage point 2).
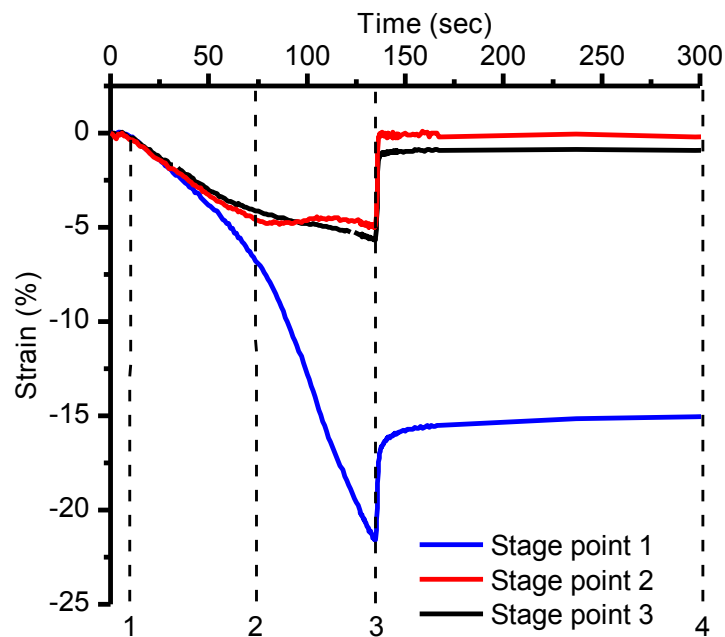
Figure 67. Strain values of two stage points on the EW540-33 cylinder.

Figure 68 shows the growth of strain along a section line created on the y-axis of the cylinder. The development of strain along the y-axis post-yield occurs primarily within the center of the specimen with strain at the specimen ends staying relatively constant. As strain continues to build, there is a slow growth of the yielded region indicated by the widening of the high strain peak. At peak strain for this specimen

(~11% total strain), the highly strained region displays a strain value over 21% while the lowest strained region displays a value of <6% resulting in a gradient of approximately 15% strain.
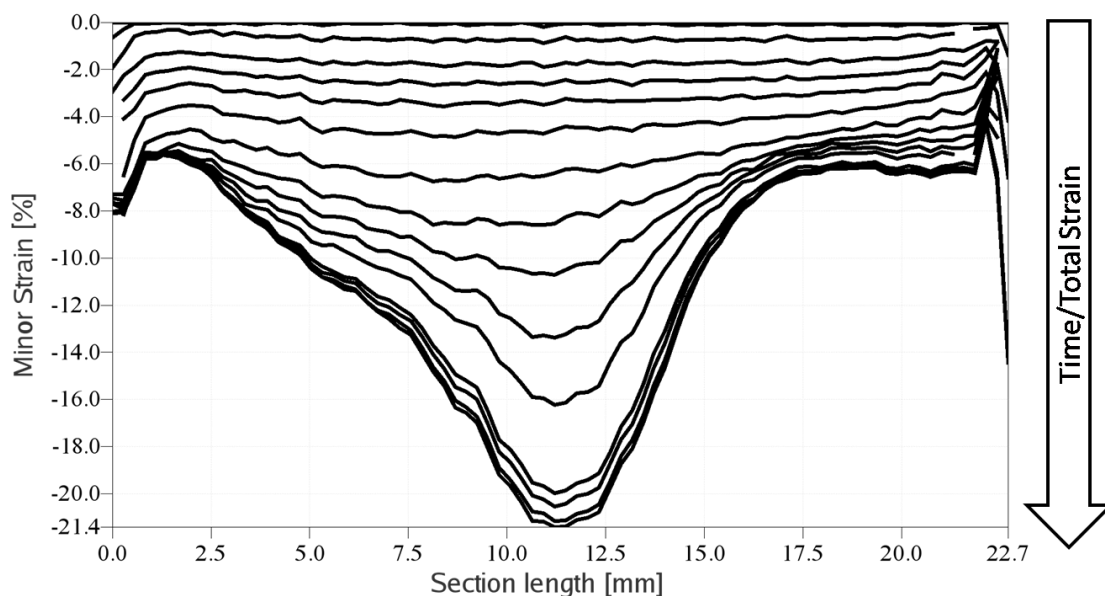
Figure 68. Development of strain along the y-axis of the cylinder.

The large degree of strain localization in the EW540 networks can be used to explain the bulk strain development and recovery patterns discussed earlier. Pre-yield behavior displays the trends that are similar to those shown in Chapters IV; however, post-yield the EW540 networks display a significantly larger amount of strain softening due to the ease of maintaining viscoplastic flow within the network. The longer segments between crosslinks allow for more flow within a local region preventing the rapid progression of the yielded region towards cylinder ends as seen in networks with a higher crosslink density. At yield, anelastic strain development ceases (as seen in Figure 65) and further strain development occurs primarily through viscoplastic flow within the locally yielded region and slow growth of the plastically deformed region.

Comparison to 33A and 44A

The previous chapter provided a comparison of the strain recovery behavior of isomer networks composed of EW175 DGEBA and 3,3'- or 4,4'-DDS (33A and 44A). These networks displayed similar development of elastic and plastic strain when plotted based on the fraction of the yield strain. However, the two isomers developed anelastic strain at different rates. This variance in anelastic strain development was determined to be the primary contributor to the different deformation characteristics of the networks. EW540-33 and EW540-44 isomers show nearly identical mechanical behavior in the form of stress-strain curves, and the strain recovery experiments showed identical strain development as well. Therefore, only the EW540-33 recovery data will be used for comparison to EW175.

Direct comparison of the strain development of the EW540-33 and EW175-33 can be seen in Figure 69 along with the stress-strain curve for each system. The significantly different stress-strain behavior can be explained by the development of strain seen in the component plots. More elastic strain developed in the EW175 network due to the achievement of a higher stress value prior to yield. Anelastic strain develops at a similar rate but deviates significantly as the EW540-33 system yields. The yield point for the two networks differs largely with the EW175-33 network yielding at a strain of 9.07% and the EW540-33 network yielding at a strain value of 5.61%. The two networks also show distinct post-yield behaviors as the EW175-33 network continues to build anelastic strain post-yield while the EW540-33 displays a decrease in anelastic strain shortly after network yielding. This decrease in anelastic strain in the EW540-33 network is accompanied by a more rapid development of plastic strain.
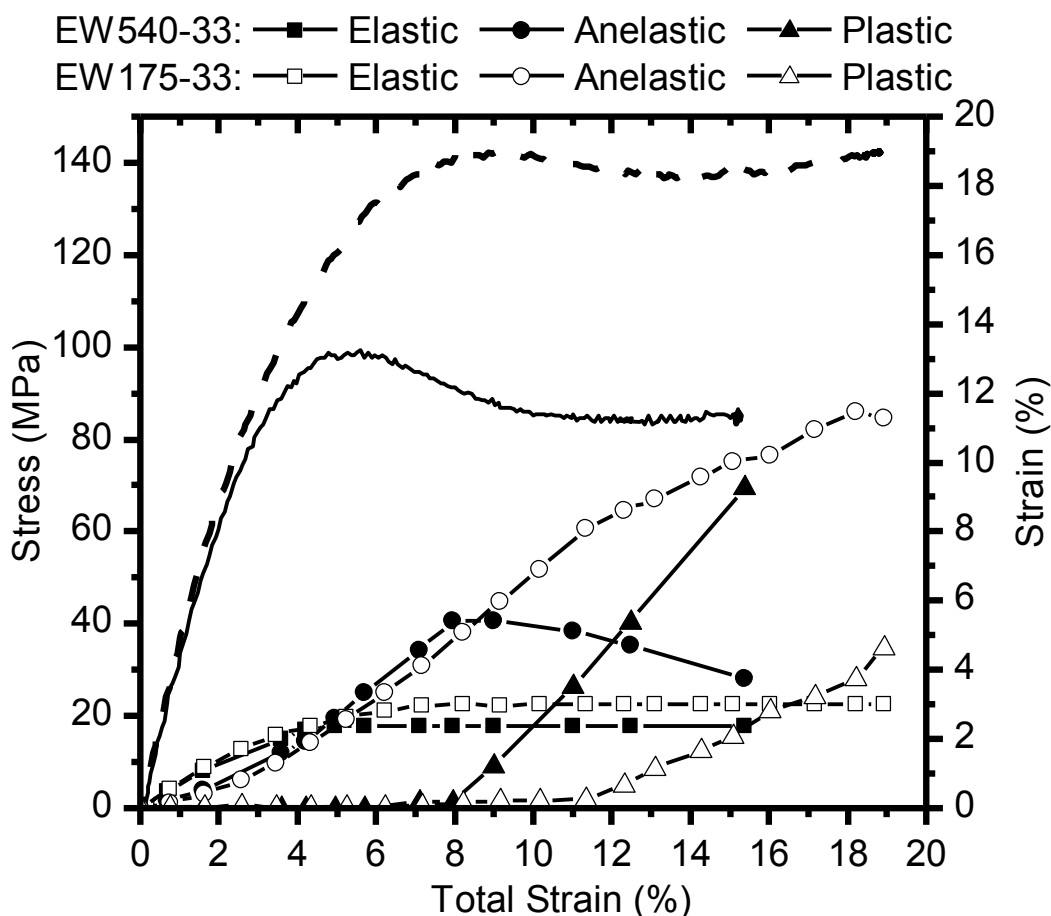
Figure 69. Comparison of strain development in EW175-33(---) and EW540-33(—) networks.

The increased rate of plastic strain development and decreased anelastic strain in the EW540-33 system can be attributed to the degree of strain localization in the yielded specimen. Figure 70 shows a deformed cylinder for the EW175-33 network along with the multi-section line plot showing development of strain along the y-axis of the cylinder with increasing time. The curvature seen in the deformed cylinder is a product of the deformation occurring out of plane. Although the results in Figure 70 for the EW175-33 system show strain localization, overall localization is decreased compared to the behavior of the EW540-33 network seen in Figures 66-68. Quantitatively, the difference in strain from low to high strained regions in the EW175-33 network range from 8-13% while in the EW540-33 network gradients range from 14-17%. The increased strain

localization in the EW540 network leads to increased strain softening where some stored energy/anelastic strain in un-yielded areas is alleviated. Once initiated, viscoplastic flow continues to occur at a stress that is lower than that required to yield additional regions, resulting in the majority of the subsequently applied strain being in the form of plastic strain. The EW175-33 network displayed only a small amount of strain softening due to the decreased strain localization, leading to the maintenance of a higher stress level and continued anelastic strain development. The EW175-44 network (not pictured) shows little to no strain softening, indicating even less strain localization.
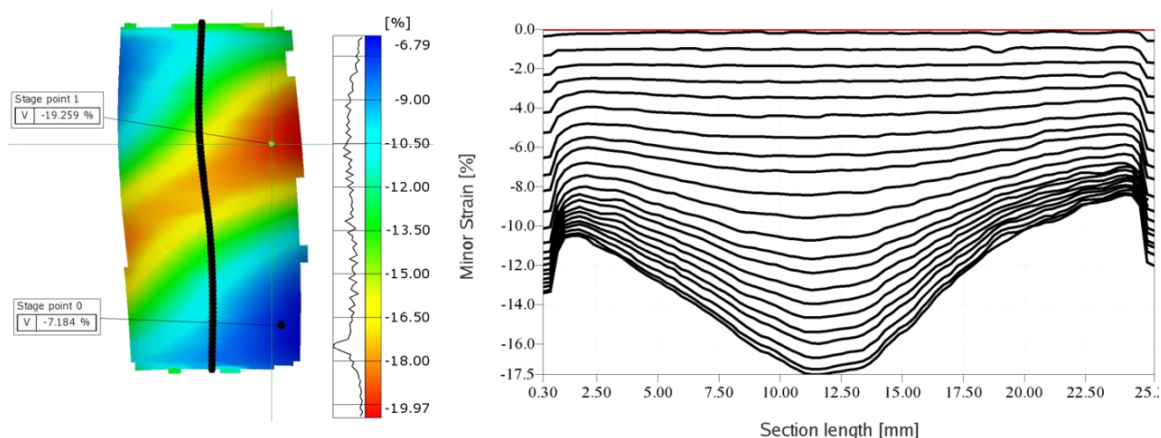
Figure 70. Strain localization in EW175-33.

The networks differ structurally by their molecular weight between crosslinks (Table 12) with the EW175-33 network possessing a significantly lower theoretical and experimental M_c. The increased frequency of junction points within the EW175 networks decreases mobility post-yield as chains exist in an almost fully extended state, not able to experience large amounts of flow. The increased length of the linear segments within the EW540 networks results in a greater mobility upon yielding, allowing the material to flow similar to what is seen in linear thermoplastic materials. It is this flow behavior that contributes to the increased localization and strain softening.

The differences in pre-yield behavior of the two networks are attributed to the earlier onset of yield in the EW540 networks. Thus far, glassy state deformation characteristics have been attributed to available molecular motions (seen in DMA Tan δ curves) and available free volume within the network. Free volume analysis was not conducted on EW540 specimen, but the differences in deformation behavior can be explained without. The stress-induced onset of α-type motions associated with yielding occured at a much higher stress and strain within the EW175 networks. This delayed yielding was a result of the network being more resistant to large segmental motions. The thermal energy required to induce α-motions, as seen in Figure 58, was much higher in the EW175 networks (T_g EW175-33 is 185°C and T_g EW540-33 is 133°C). The requirement of more thermal energy to induce flow would indicate that this network would require more stress to cause yielding. Additionally, sub-T_g transitions are indicative of available cooperative motions in the glassy state. The DMA Tan δ sub-T_g transitions seen in Figure 59 indicated that the EW540 networks have a higher glassy state mobility as the sub-T_g transitions had a larger area and lower temperature than those of the EW175 networks. Additionally, the temperature range of the EW175 networks extended past the temperature of testing (25°C), indicating that some glassy state motions were not available at the testing temperature providing additional rigidity and resistance to yield.

<div align="center">Conclusions</div>

The scope of this chapter was to investigate structure-property relationships of glassy polymer networks through varying the equivalent weight of the DGEBA based epoxy network isomers. Compression experiments conducted on cylindrical specimens showed a clear step-down in the stress and strain at yield with increasing epoxy

equivalent weight for both 3,3'- and 4,4-DDS cured networks. The decrease in yield

values was attributed to an increase in molecular weight between crosslinks, which

creates more cooperative glassy state mobility as seen in dynamic mechanical analysis.

DMA Tan δ curves showed a decrease in temperature of the α- transition with increasing

M_c, indicating the requirement of less energy to induce α-motions. A decrease in

temperature was also seen for the β- transitions, along with an increase in area of the

peaks, revealing the availability of more cooperative motions along the increased linear

segments.

Additional analysis of network isomers revealed that increased DGEBA EW

decreased the effect that curative isomer structure had on deformation. The EW540

isomers showed nearly identical stress-strain behavior with similar modulus, yield stress,

and yield strain values. This behavior illustrated that deformation became controlled

primarily by the long, linear DGEBA segments within the network. These segments have

a decreased resistance to flow, indicated by the low yield stress, and are the primary

component of the network as the maintenance of stoichiometric ratios decreases the

overall amine segment concentration.

Strain recovery experiments were used to investigate strain development in the

EW540 networks. These results showed an earlier onset and a more rapid development

of plastic strain when compared to the EW175 networks discussed in Chapter IV. The

increased rate of plastic strain development was accompanied with a decrease in anelastic

strain post-yield. These differences in strain development were attributed to increased

strain localization due to an increased molecular weight between crosslinks. More

cooperative motions were available in the EW540 networks resulting in a lower

resistance to yield. Once yield began, significant strain softening occurred as the stress

required to continue flow in the yielded region was lower than the stress required to

initiate local flow.

References

1. Mayr, A.E.; Cook, W.D.; Edward, G.H. *Polymer* **1998**, *39*, 3719-3724.
2. Sindt, O.; Perez, J.; Gerard, J.F. *Polymer* **1996**, *37,* 2989-2997.
3. Cook, W.D.; Mayr, A.E.; Edward, G.H. *Polymer* **1998,** *39*, 3725-3733.
4. Lesser, A.J.; Calzia, K.J. J. Polym. Sci. Pol. Phys. **2004,** *42*, 2050-2056.
5. Glad, M. D.; Kramer, E. J. *J. Mater. Sci.* **1991**, *26*, 2273-2286.
6. Lin, C.J.; Bell, J.P. *J. Appl. Polym. Sci.* **1972,** *16*, 1721-1733.
7. Murayama, T.; Bell, J.P. *J. Polym. Sci. A1.* **1970,** *8*, 437-445.
8. Meyer, F.; Sanz, G.; Eceiza, A.; Mondragon, I.; Mijovic, J. *Polymer* **1995**, *36,* 1407-1414.
9. Barton, J.M.; Hamerton, I.; Howlin, B.J.; Jones, J.R.; Liu, S. *Polymer* **1998**, *39*, 1929-1937.
10. Lee, J.; Yee, A. F. *Polymer***, 2000**, *41*, 8375-8385.
11. Tarasov, V.P.; Smirnov, Y.N.; Yerofeyev, L.N.; Irzhak, V.I.; Rozenberg, B.A. *Polymer Science USSR*. **1983**, *24*, 2732-2736.
12. Kaushik, M.; Jackson, M.B.; Heinz, S.R.; Wiggins, J.S.; Nazarenko, S. Proceedings from SAMPE Fall Meeting, Wichita, KS, October 20-23, 2009.
13. Tobolsky, A.V.; Carlson, D.W.; Indictor, N. *J. Polym. Sci.* **1961**, *54*, 175-192.
14. Tobolsky, A.V. *J. Polym. Sci. Pol. Sym.* **1965**, *9*, 157-191.
15. Imaz, J.J.; Juvado, M.J.; Corcuera, M.A.; Mondragon. I.J. *J. Appl. Polym. Sci.* **1992**, *46*, 147-166.
16. Oleinik, E.F.; Rudnev, S.N.; Salamatina, O.B.; Shenogin, S.V.; Kotelyanskii, M.I.; Paramzina, T.V.; Nazarenko, S.I. *e-Polymers* **2006** no. 029.

CHAPTER VI

EFFECTS OF ISOMERISM AND INCREASED CROSSLINK DENSITY ON

DEFORMATION OF GLASSY NETWORKS

Introduction
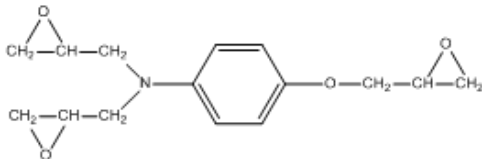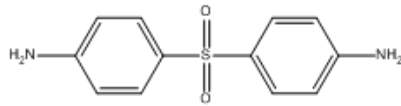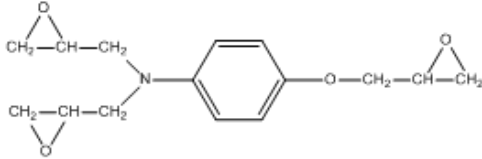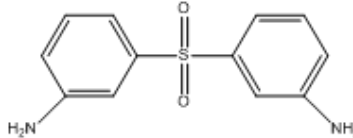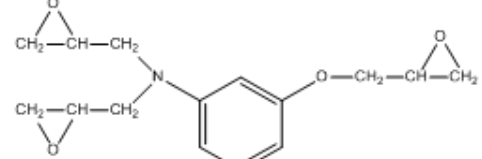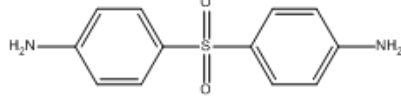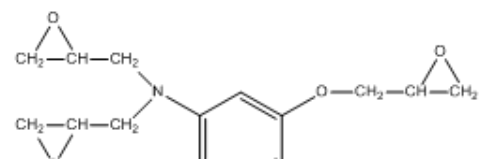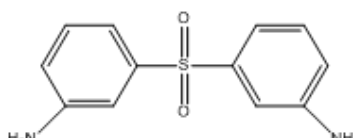
In continuation of the investigation of isomer effects on mechanical deformation

of epoxy networks, a new set of isomer networks were investigated. This chapter

discusses the results of trifunctional aminophenol based epoxy resins cured with 3,3'- or

4,4'-DDS. The use of the triglycidyl aminophenol (TGAP) resin allows for exploration

of isomerism within the epoxy segment along with the amine segment, as the

aminophenol can be either meta- or para-substituted. The deformation behaviors of the

four different networks were compared through compression tests and strain recovery

experiments and related to the different network mobility and free volume created by

isomer position. Additional comparisons on the effects of Mc on deformation can be

obtained through comparison of the tighter bound TGAP based networks to the networks

based on linear DGEBA epoxies of the previous chapters. The TGAP resins differ from

the previously used DGEBA as they are tri-functional and possess a shorter chain

segment in between functional groups. This will create a tighter bound network with a

higher crosslink density.

Materials

Epoxy resins were based on epoxidized aminophenol, resulting in a tri-functional

resin that can be meta- or para-substituted. Resins were supplied by Huntsman Advanced

Materials under the trade names of Araldite MY 0510 (triglycidyl ether of para-

aminophenol, p-TGAP) and Araldite MY 0610 (triglycidyl ether of meta-aminophenol,

m-TGAP). Epoxy resins were cured at a 1:1 ratio of epoxy to amine reactive hydrogen

using either 3,3'-Diaminodiphenyl sulfone (33DDS, 97% purity) or 4,4'-diaminodiphenyl

sulfone (44DDS, 97% purity), which were purchased from Sigma Aldrich and used as

received. Chemical structures for the raw materials and nomenclatures for final cured

networks are seen in Table 14.

Table 14. Monomer Composition of the Four Isomer Networks

System	Epoxy Resin	Curative
44pAP		
33pAP		
44mAP		
33mAP		

Results

Deformation Behavior of TGAP Based Isomers

Figure 71 displays stress vs. digital image correlation (DIC) measured strain for

the four different isomer networks, showing a vast array of mechanical deformation

characteristics based on isomer positions. The isomer position clearly affects the

modulus, the yield point (stress and strain), the amount of strain softening post yield and thereby, the onset of strain hardening. The all meta-substituted 33mAP system displayed the most rigid behavior, showing the highest modulus, highest yield stress, and lowest yield strain. On the contrary, the fully para-substituted 44pAP system possessed the lowest modulus, lowest yield stress, and highest yield strain. A summary of the compressive properties can be found in Table 15.
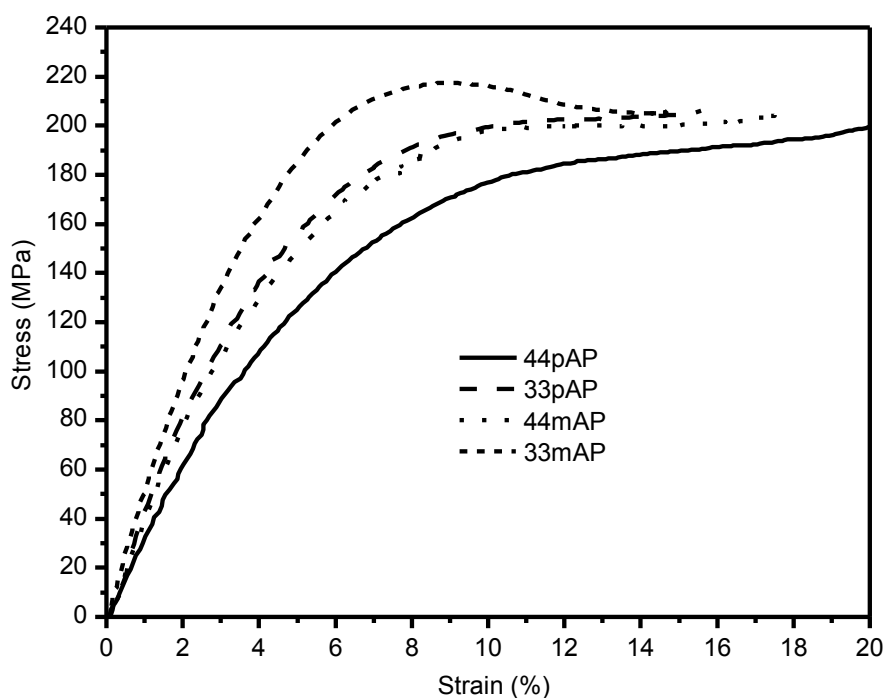
Figure 71. Stress-strain comparison of the four isomer networks.

Table 15. Compressive Properties of Isomer Networks.

	Modulus (MPa)	Yield Stress (MPa)	Yield Strain (%)
44pAP	3385	~190	>14.0
33pAP	4977	~203	~13.0
44mAP	4369	~200	~12.4
33mAP	5540	217.5	8.96

The properties compiled in Table 15 show approximated yield values for the 44pAP, 33pAP, and 44mAP systems as these networks did not show an identifiable drop

in the stress-strain curve. This behavior suggests very limited strain softening within the network, likely a product of the high crosslink density. The fully meta-substituted 33mAP network did show clear yield and subsequent strain softening, indicating a higher stress dissipation capacity than networks containing para-substitution (epoxy, amine, or both). This behavior is similar to what was seen in Chapter IV as the 33A system displayed more rigid behavior prior to yield and an increased strain softening post-yield when compared to the 44A network.

Thermomechanical Behavior

Figure 72 shows tensile dynamic mechanical analysis, displaying both modulus (E') and Tan δ curves for the four network isomers. The systems displayed similar behaviors with the exception of the 44pAP network, which displayed a significantly lower E' than the others. The 44pAP network showed the lowest compression modulus as well, but not to the same degree. Decreased modulus values associated with network α-transitions occur at different temperatures for each network and show the trend of increased transition temperature with increasing para-substitution. A similar result was seen in lower equivalent weight DGEBA based isomer networks. Rubbery modulus values vary for each network and are reflective of network crosslink density.
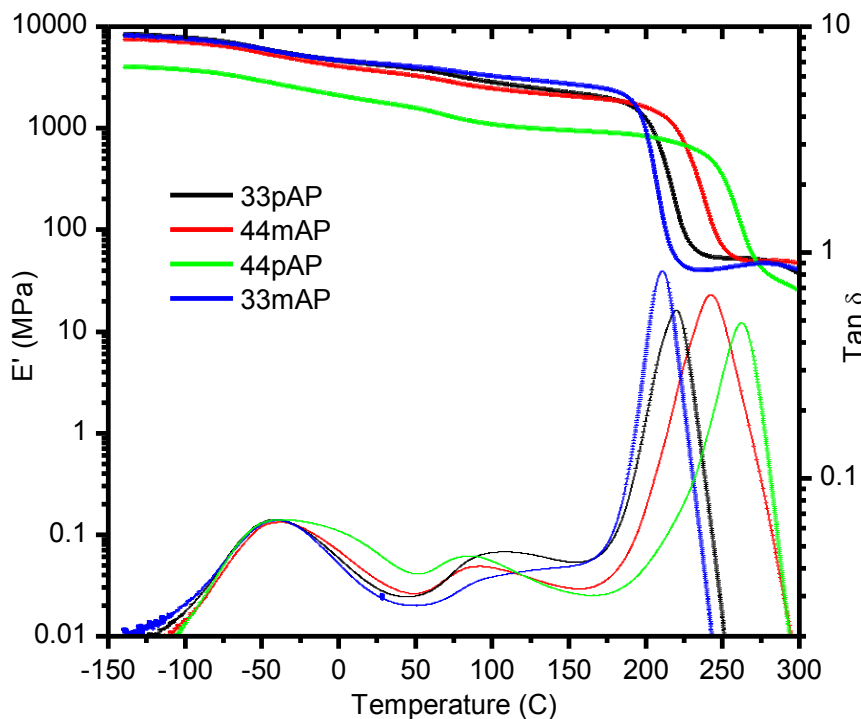
Figure 72. DMA modulus and tan δ curves for isomer networks.

Experimental M_c values were calculated for each network based on the theory of rubber elasticity according to same procedures discussed in Chapter V. The theoretical molecular weight between crosslinks was calculated using monomer weights and functionalities:

$$M_{c,the} = \frac{(3m_a + 4m_e)}{7}$$

Equation 12

where m_a is the amine molecular weight and m_e is the epoxy molecular weight. Values for the experimental and theoretical M_c values can be found in Table 16. Experimental M_c values differed for all networks indicating conversion and connectivity differences. The variances in M_c are associated with variances in reactivity, vitrification, and steric hindrances within each isomer network. The discrepancies in experimental and theoretical M_c values are likely a result of the weakest domain of the network dominating rubbery state properties. At temperatures above the T_g, applied stress will induce strain

only within the weakest or loosest bound region of the material. At the low stain

amplitudes of DMA, it is highly likely that the measure E' in the rubbery state is only

indicative of these regions. The resulting M_c value is thus not an average, but a

representation of the weakest region of the network.

Table 16. M_c Data for the Aminophenol-Based Isomer Networks

System	E'$_r$ (MPa)	Density (g/ml)	$M_{c, exp}$ (g)	$M_{c, the}$ (g)
44pAP	27.5	1.3196	680.1	264.7
44mAP	49.4	1.3250	364.6	264.7
33pAP	53.0	1.3288	328.2	264.7
33mAP	40.2	1.3242	420.0	264.7

The TGAP based networks all display two distinct sub-T_g transitions, labeled as β

and γ in Figure 72. The β-transition is extremely broad, stretching from $^-125°C – {}^+50°C$.

Three of the four isomer networks (33pAP, 44mAP, and 33mAP) display nearly identical

β-transitions, while the 44pAP system displays a slightly broader transition. A second

sub-T_g transition, the γ-transition, is seen in the Tan δ curves in the 50-150°C range. This

peak is smaller in both magnitude and breadth than the β-transition. A summary of the

transition temperatures and peak areas can be found in Table 17.

Table 17. Tan δ Transition Temperatures and Areas for TGAP Isomer Networks

	$T_α$	Area	$T_β$	Area	$T_γ$	Area
44pAP	262.6	14.86	-42.7	3.48	89.1	0.48
44mAP	242.5	23.44	-39.9	2.98	91.2	0.49
33pAP	220.1	14.75	-42.5	2.99	99.5	0.60
33mAP	211.0	17.58	-40.8	2.95	N/A	N/A

The β-transitions of the isomer networks were similar (with the exception of

44pAp), but the γ-transitions differed significantly. The p-TGAP networks displayed a

sharper γ-transition with maxima at ~90°C while the m-TGAP networks showed a less

pronounced transition that becomes a shoulder of the α-transition. The γ-transition of the

44mAP network displayed a maximum near 100˚C while it failed to display a maximum in the 33mAP network. This difference in transition maxima indicates that the energy required to activate these motions was greater in the m-TGAP systems. The meta-substitution of the epoxy allows for tighter packing of segments, thereby requiring more energy to loosen the chain segments. The amine substitution also affected the shape of the γ-transition as 4,4'-DDS networks displayed peaks of larger magnitude than those 3,3'-DDS networks, suggesting an increased mobility of the 4,4'-DDS networks. Increased mobility arises from the variances in cooperative motions within the networks. The 4,4'-DDS networks showed a lower overall conversion as indicated by a large residual exotherm in the DSC traces in Figure 73. A lower conversion leaves more free chain ends in the system, creating a lower overall crosslink density. Decreased crosslink density also allows for more cooperative motion due to an increase in unbound segments.
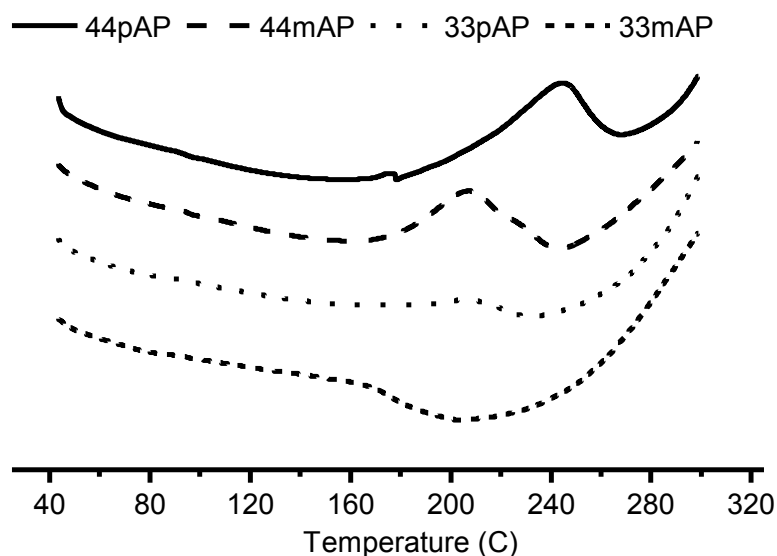
Figure 73. DSC first scan traces of multifunctional isomer networks.

As discussed in previous chapters, the origins of these transitions are not completely understood, but motions associated with the lower temperature transition have

been reported to be associated with phenyl-ring re-orientations within the epoxy and amine segments,[1] onset of motions from unreacted glycidyl groups,[2] and crankshaft motions of the hydroxylether groups.[3] Furthermore, it has also been debated as to whether or not the sub-T_g transitions are a response of cooperative motions within the glassy state with those such as Starkweather declaring that sub-T_g motions involve small segments independent of one another.[4,5] However, additives have been shown to facilitate or restrict motion associated with the sub-T_g transition, indicating that motions can exhibit cooperativity.[6,7] The existence of cooperative motion helps to explain the behavior exhibited by the isomer networks in Figure 72, which will be discussed in detail later.

Motions associated with the γ-transition are even less understood but are likely associated with activation of motion within more hydroxypropyl ether segments. Solid state ^{13}C NMR analysis has shown the activation of HPE methylene segments at temperature ranges of 60-90°C for DGEBA/DDM (4,4'-diaminodiphenyl methane) networks.[8] This increased motion of HPE units occurs through disruption of the hydrogen bonding associated with the secondary hydroxyl. Disruption of hydrogen bonding of these segments has been shown to occur in the 30-140°C range.[9] Increased presence of the γ-transition compared to the linear DGEBA networks of Chapters IV and V can be associated with the increased relative concentration of HPE segments in the TGAP networks. Another contributing factor to consider is the proximity of neighboring chains to one another. The tighter bound TGAP networks result in increased hydrogen bonding due to the increase of binding partners in the surrounding neighborhood.

Strain Recovery Experiments

Strain recovery experiments were conducted on the four resin systems at various increments of unloading, depending on the number of cylinders for each sample set. Figure 74 shows the stress-strain curves for each recovery experiment with the loading paths tracking almost identically to one another and the unloading curves dropping at various unloading strains. The resulting recovery envelopes increased in size as the unloading strain increased. These stress-strain curves were used to determine the peak strain of each individual recovery experiment. Subsequent calculation of strain components and recovery rates were based on the determined peak strain.

Table 18 Table 18 lists the individual experiments for each of the four isomer networks, along with the unloading, or peak, strain for each test. To further clarify, the column labeled control strain corresponds to the strain endpoint set in the test control software. This control strain is LVDT based and cannot be used in subsequent calculations as compliance was not accounted for. The column labeled peak strain corresponds to the DIC measured maximum strain as determined by the average of surface strain across the entire visible surface. This strain value was used for all calculated strain components.
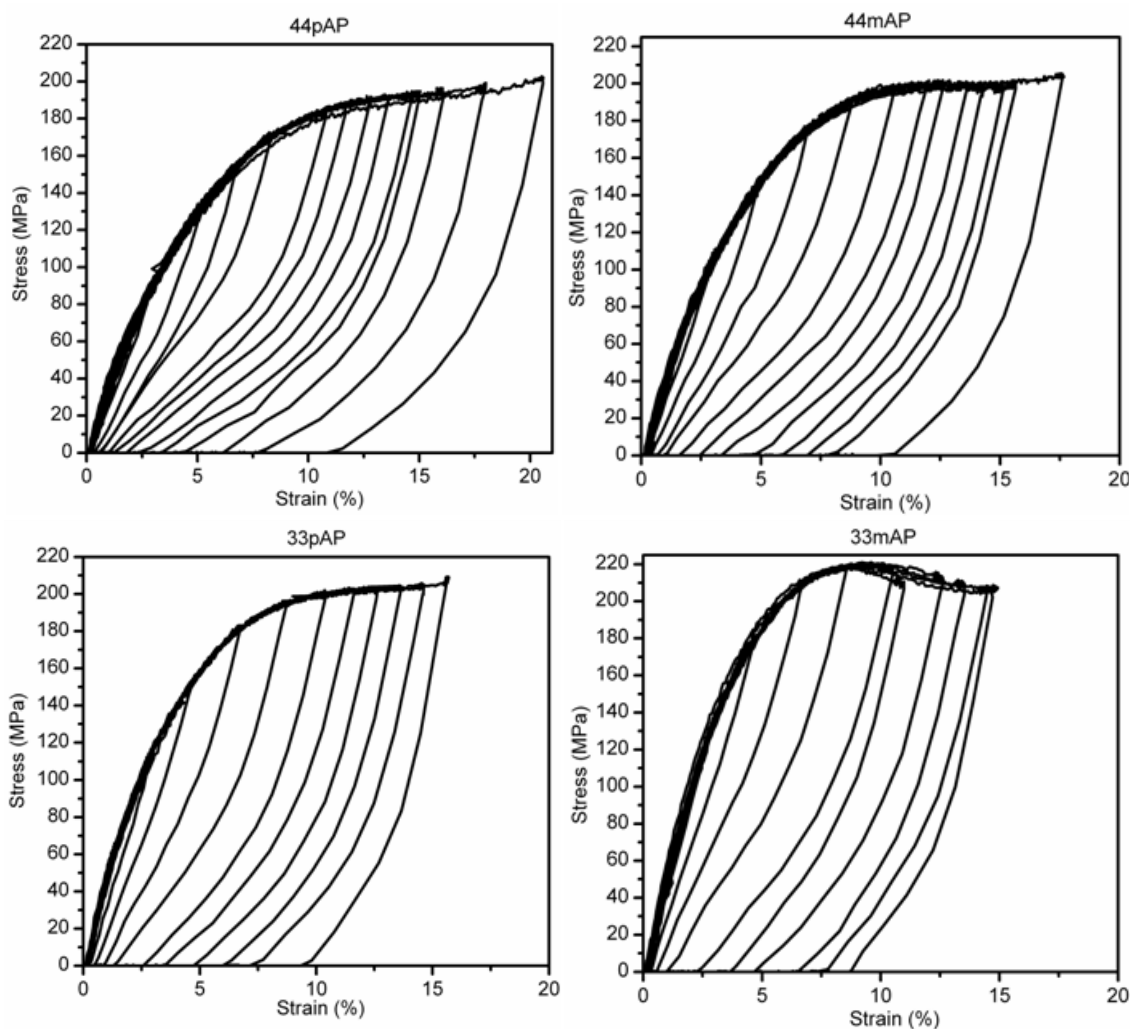
Figure 74. Stress-strain curves of all recovery experiments for all four aminophenol-based systems.

Table 18. Control and Peak Strains for Strain Recovery Experiments

44pAP		33pAP		44mAP		33mAP	
Control Strain	Peak Strain	Control Strain	Peak Strain	Control Strain	Peak Strain	Control Strain	Peak Strain
2%	1.275	2%	1.357	2%	1.476	2%	1.224
4%	3.08	4%	3.132	4%	3.139	4%	2.938
6%	5.147	6%	4.645	6%	4.858	6%	4.737
8%	6.854	8%	6.784	8%	6.97	8%	6.679
10%	8.372	10%	8.737	10%	8.813	10%	8.582
12%	10.803	12%	10.379	12%	10.564	12%	10.501
13%	11.678	13%	11.644	13%	11.927	13%	11.07
14%	12.865	14%	12.617	14%	12.845	14%	12.269
15%	13.602	15%	13.626	15%	13.64	15%	13.548
16%	14.652	16%	14.625	16%	14.527	16%	14.518
17%	15.392	17%	N/A	17%	15.128	17%	15.44
18%	16.066	18%	16.415	18%	16.571	18%	16.592
20%	17.999	20%	18.268	20%	18.258	20%	N/A
22%	20.601						

Recovery curves for each experiment can be seen in Figure 75, where the peak strains are indicated by the maximum of the individual curves. Recovery curves are limited to the initial 10 minute recovery period following specimen unloading. Subsequent recovery during extended time periods and elevated temperatures will be discussed in a later section. Of the four sets of recovery curves seen in Figure 75, the curves for the 44pAP system show a quicker room temperature recovery rate, as well as a larger magnitude of recovered strain. The highest strain experiment (22% LVDT strain) showed only ~6% residual strain after 10 minutes whereas this amount of residual strain was obtained in lower magnitude experiments for the other three systems. This larger quantity of recovered strain indicates a larger amount of anelastic strain was placed on the 44pAP system during loading.
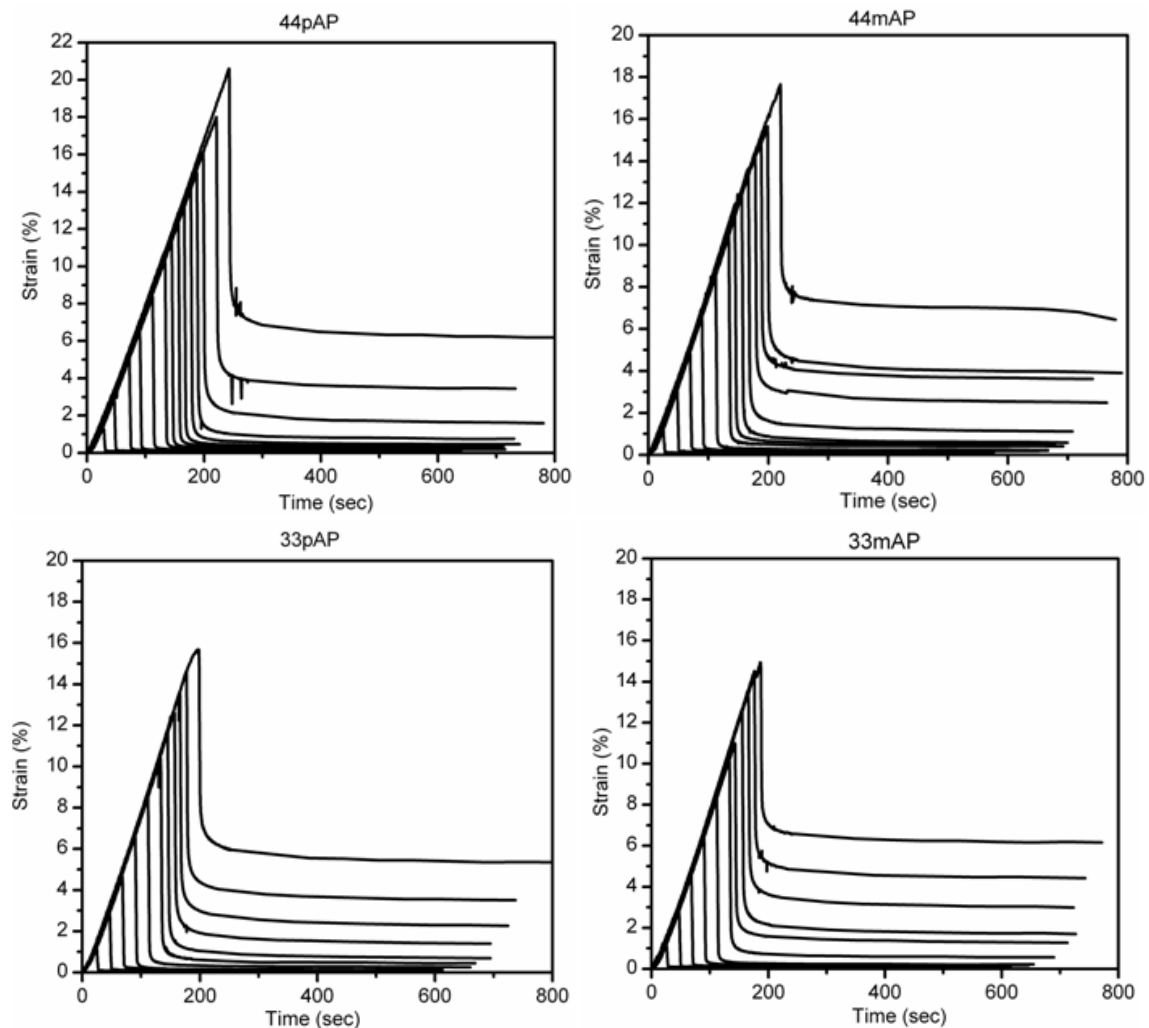
Figure 75. Strain vs. time curves for all recovery experiments of the four isomer networks.

A more direct comparison of the recovery behavior of the four isomer networks was obtained by analysis of recovery curves with the same unloading strain for each system. Figure 76 shows the 16% anelastic recovery curves for each of the four networks. The 16% experiments were chosen based on their similar peak strains as seen in Table 18. Only anelastic strain recovery was considered for this comparison; therefore, the initial residual strain value was determined by subtraction of the elastic strain component from the peak strain value reported for each network. The anelastic strain recovery curves seen in Figure 76 show a clear difference in the amount of residual

strain with the 44pAP system recovering the most strain and the 33mAP system recovering the least amount of strain.
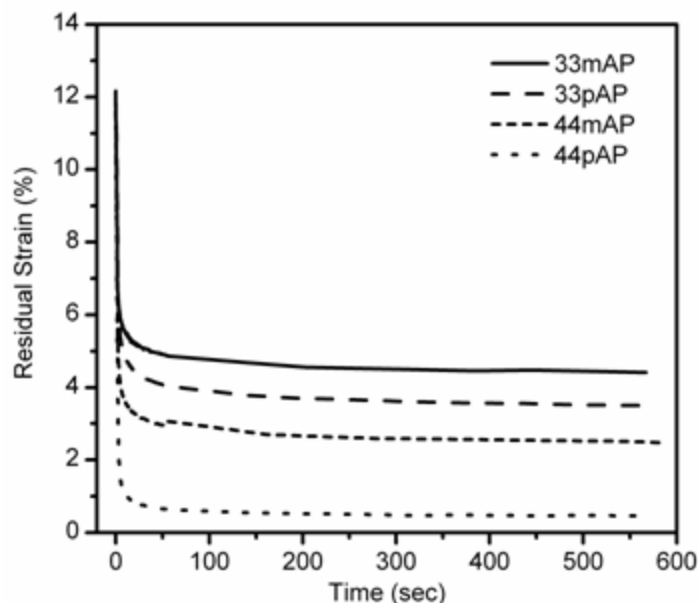
Figure 76. Comparison of anelastic strain recovery of the four isomer networks.

The anelastic recovery curves followed an exponential decay pattern, allowing for further quantification of isomer recovery differences based mathematical fits to the raw data. A three component exponential decay function was applied to each of the anelastic strain recovery curves seen in Figure 76. A three component exponential fit implies that there are at least three decay routes, which for strain recovery means that there are multiple molecular motions occurring simultaneously. The resulting three component fit data is seen in Table 19, where constants apply to the equation:

$$y = A1*\exp(-x/t1) + A2*\exp(-x/t2) + A3*\exp(-x/t3) + y0 \qquad \text{Equation 13}$$

in which A1, A2, and A3 represent the individual recovery components, and t1, t2, and t3 represent the time scale of recovery for each of these components. Components A1 and A2 were of similar value for each of the four isomer networks while the primary contributing component is A3. The magnitudes of the A3 component account for the

difference in strain recovery of the networks, indicating that the motions associated with this component were able to more freely occur in the fully para-substituted network. The motions associated with the A1 and A2 components appear to have similar mobility as they occur in nearly equal amounts in each network. However, investigation of the relative time scales of these recovery components showed the 44pAP A1 and A2 components to recover at a time scale an order of magnitude faster than the other networks. Additionally, the time scale of the mixed para- and meta- networks are the longest, indicating some form of restricted mobility.

Table 19. Three Component Exponential Fit Constants for the Four Isomer Networks.

	33mAP	33pAP	44mAP	44pAP
y0	4.442	3.487	2.495	0.519
A1	1.102	1.221	1.146	1.288
t1	10.464	15.171	11.934	1.485
A2	0.734	0.738	0.653	0.760
t2	113.26	164.46	148.83	25.088
A3	5.588	6.774	7.343	9.565
t3	1.154	1.684	1.379	1.485

Room temperature recover. Residual strains of deformed cylinders for each recovery experiment are displayed in Figure 77. Residual strains are plotted along with the stress-strain curves of the networks in order to illustrate where in the loading path the respective cylinder was unloaded. Three residual strain curves are displayed for each network showing the effects of time on room temperature recovery within the tightly bound network. The 10 minute curves use residual strains seen in Figure 75 while the 1-day and 4-week curves were generated from additional data points collected at the specified point in time. Four-week data was generated from specimen heights as the speckle coating displayed inaccurate results due to aging and adhesion complications.
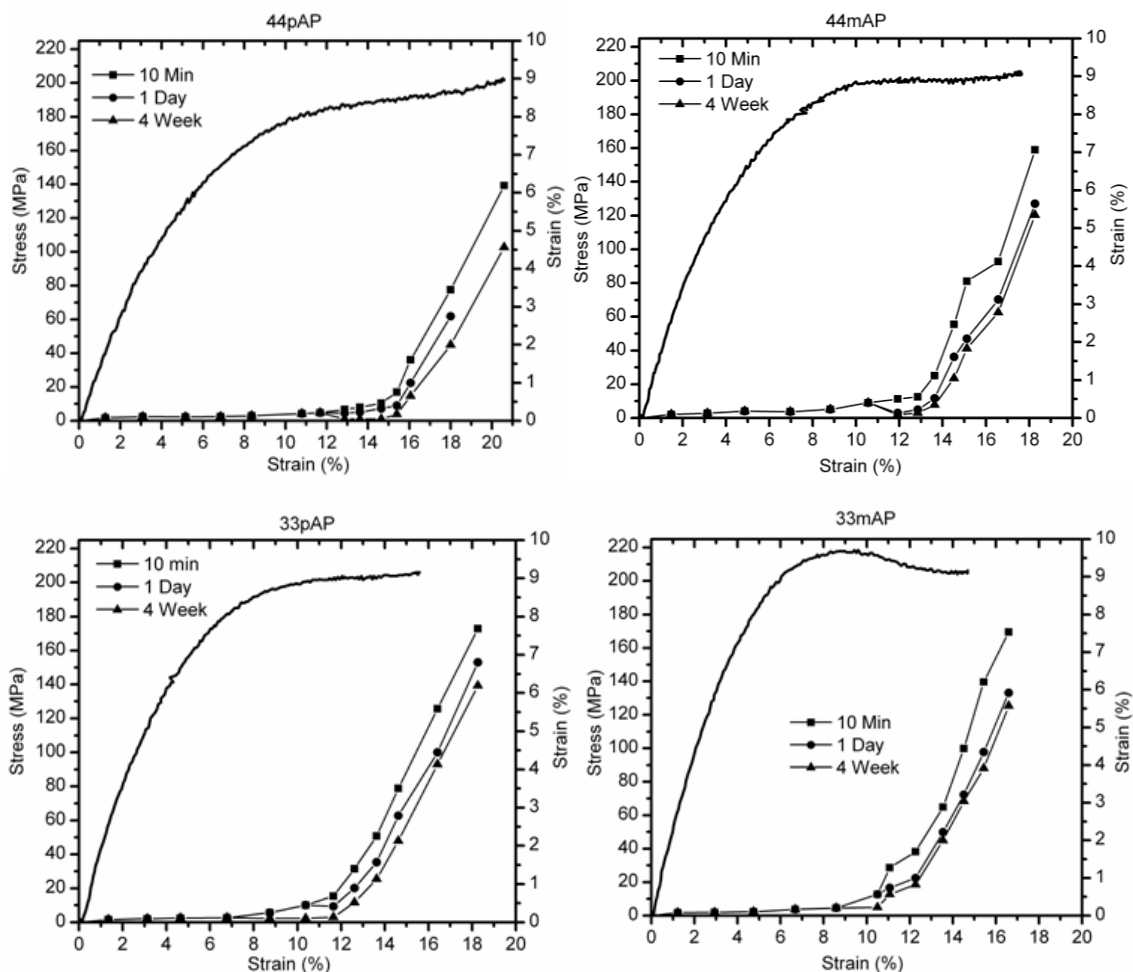
Figure 77. Residual strain plots for the four isomer networks.

Extended recovery periods resulted in more recovered strain in all networks, with 1.5-1.75% additional strain recovered during the 4-week dwell. 3,3'-DDS networks recovered a lower overall amount of strain (i.e., they possessed more residual strain) when compared to their 4,4'-DDS cured counterparts, indicating fewer available recovery processes or restricted network mobility. A trend for extended recovery times was not evident when comparing the rates of recovery for the para- and meta-substituted epoxy. However, the p-TGAP based networks appeared to recover more strain than their meta-substituted counterparts. The onset of residual strain for the networks correlates to the yield point and increased with increasing para-substitution.

Elevated temperature recovery. The above analysis was limited to room temperature recovery for extended time periods. As illustrated in the previous chapters, extended recovery occurs by heating the deformed specimens to higher temperatures with complete anelastic recovery occurring at temperatures of T_g-20˚C.[10,11,12,13,14] The TGAP based networks often display weak thermal transitions that are sometimes difficult to see through DSC. Transitions can also be hidden by an exothermic peak associated with further curing reactions within the highly crosslinked networks. Vitrification rapidly occurs in these networks, with glass transition temperatures often exceeding that of the curing temperature. This rapid vitrification results in the entrapment of unreacted functional groups within the network. Heating the network towards the glass transition temperature results in an increase in mobility leading to subsequent exothermic reaction, a phenomenon that was particularly evident in the 4,4'-DDS cured networks.   Figure 73 shows first scan DSC thermal traces for the isomer networks heated at 10˚C/minute. Networks cured with 3,3'-DDS (33pAP and 33mAP) showed a clear exothermic glass transition temperatures at 220˚C and 180˚C respectively. However, the networks cured with 4,4'-DDS (44pAP and 44mAP) did not show a clear transition due to exothermic heat release from subsequent curing reactions. Due to the inability to determine a distinct glass transition for all networks through DSC, the elevated temperature recovery was conducted in equal stages for each system with temperatures being selected based on transitions seen in the DMA Tan δ curves (Figure 72). The temperatures for elevated temperature recovery can be seen in Table 20 with stages 1-3 being sub-T_g/anelastic recovery and stage 4 being above T_g to show complete strain recovery. Recovery at each temperature was monitored through change in height of the cylindrical specimens.

Table 20. Elevated Temperature Recovery Stages

Network	Stage 1	Stage 2	Stage 3 (full anelastic recovery)	Stage 4 (complete recovery)
44pAP	24hr 50°C	2hr 100°C	2hr 150°C	1hr 250°C
33pAP	24hr 50°C	2hr 100°C	2hr 150°C	1hr 230°C
44mAP	24hr 50°C	2hr 100°C	2hr 150°C	1hr 230°C
33mAP	24hr 50°C	2hr 100°C	2hr 150°C	1hr 220°C

Residual strain plots showing recovery at elevated temperatures are displayed in Figure 78 for all four isomer networks. The sub-T_g recovery was conducted in 50°C increments starting at 50°C and ending at 150°C. Further sub-T_g recovery did not occur when cylinders were heated to 160°C for 2 hours, indicating all anelastic strain had recovered following 2 hours at 150°C. The final set of data points for each network is after thermal treatment at a temperature above T_g. The specific temperature for this stage varied depending on the determined T_g for each network with the 44pAP network requiring the highest temperature treatment (250°C) and the all meta-substituted network requiring the lowest temperature (220°C). Specific above T_g recovery temperatures were determined based on the DSC measurements seen in Figure 73 with temperatures for 44pAP and 44mAP approximated at a temperature just past the exothermic peak.
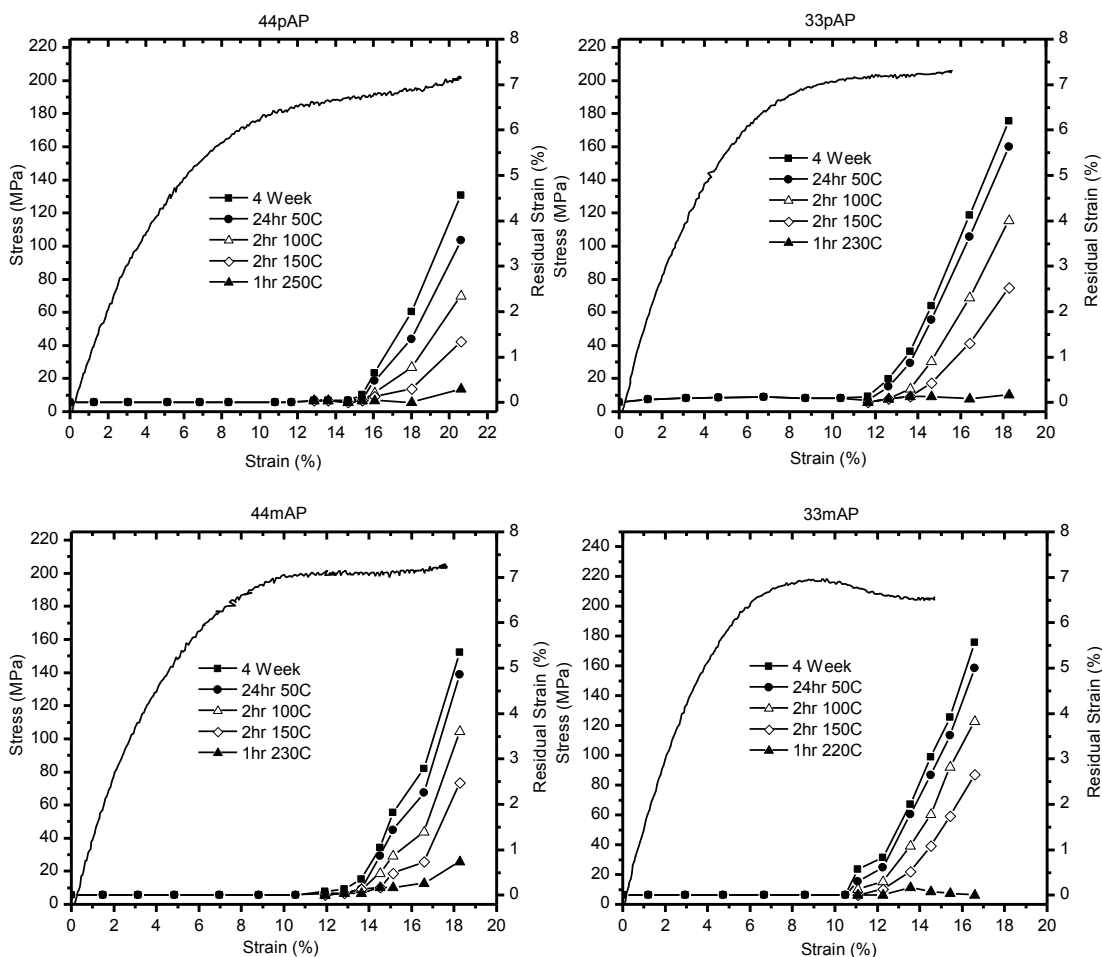
Figure 78. Residual strain plots for multifunctional networks.

Comparison of the networks revealed that the 44pAP system recovered the most strain at the first elevated temperature stage (~1%) while the other networks recovered significantly less. Subsequent recovery stages yielded results with no clear trends, indicating similar recovery mechanisms for each network. Recovery at a temperature above T_g theoretically should return each network to its original state, a result that was illustrated in the 3,3'-DDS cured networks but not in the 4,4'-DDS cured networks. The 44pAP and 44mAP networks still retained a small amount of strain after treatment at 250˚C and 230˚C respectively. This remaining strain was due to one of two reasons, both of which are a result of the subsequent curing at temperatures above the glass transition

temperature. The further advancement of cure either resulted in a re-vitrification of the network prior to complete recovery or subsequent crosslinking "locked-in" the remaining unrecovered strain and prevented complete recovery. Either way, complete recovery did not occur in the 4,4'-DDS cured networks.

Investigation of the dynamic mechanical analysis tan δ curves in Figure 72 aids in explanation of the elevated temperature recovery trends seen in Figure 78. The first stage of the elevated temperature recovery occurred at 50˚C immediately following the completion of the β-transition. However, the breadth of the β-transition of the 44pAP network extended further into the 25-50˚C range explaining the increased amount of strain recovery for this system at 50˚C. Recovery at 100˚C occurred within the γ-transition, resulting in the significant recovery seen in Figure 78. Further recovery was seen at 150˚C as all motions associated with this transition were activated. As we discussed previously, the γ-transition is associated with activation of hydroxypropyl ether segments by disruption of the hydrogen bonding associated with the secondary hydroxyl. The isomer networks displayed differing behaviors at this transition (location of maximum and relative magnitude) with the m-TGAP network transitions occurring at a higher temperature. The higher temperature requirement indicates that the energy required to activate the motions was greater in the m-TGAP networks. The increased energy requirement arises from the proximity of hydroxypropyl ether segments to one another. The meta-substitution of the epoxy allows for tighter packing of segments and thereby, closer proximity of neighboring hydroxyls, amines, sulfones, etc., creating more and stronger hydrogen bonds. The amine substitution affected the magnitude of this transition, with γ-transitions of the 4,4'-DDS networks displaying a larger magnitude than those cured with 3,3'-DDS. The increased magnitude suggests an increased

mobility of the 4,4'-DDS networks. Increased mobility indicated by this transition likely arises from the variances in free volume of the networks, as seen in the DGEBA isomers. Another plausible explanation for the higher magnitude of the 4,4'-DDS transition is related to the overall conversion. Recall that the DSC traces in Figure 73 displayed a large residual exotherm for systems cured with 4,4'-DDS, indicating a lower overall conversion for these systems. A lower conversion leaves more free chain ends in the system creating a lower overall crosslink density. In a network with a high crosslink density like these, free chain ends act to plasticize the network increasing mobility.

Determination of strain components. Strain component plots were developed based on the method developed in Chapter III, with the elastic strain being calculated according to Hooke's Law and Theory of Linear Elasticity using the equation $\varepsilon_{elastic} = \sigma_t / E_{ur}$ where E_{ur} is the unrelaxed modulus and σ_t is the stress at the unloading time.[10,15,16,17,18] Anelastic strain was calculated as $\varepsilon_{anelastic} = \varepsilon_{total} - \varepsilon_{residual} - \varepsilon_{elastic}$ where ε_{total} is the maximum point of the strain-time curve in Figure 75 and $\varepsilon_{residual}$ is the measured strain remaining on each test specimen. Strain component plots for the TGAP based isomer recovery measurements are displayed in Figure 79 where individual data points are calculated from the residual strains following recovery at 150°C seen in Figure 78.
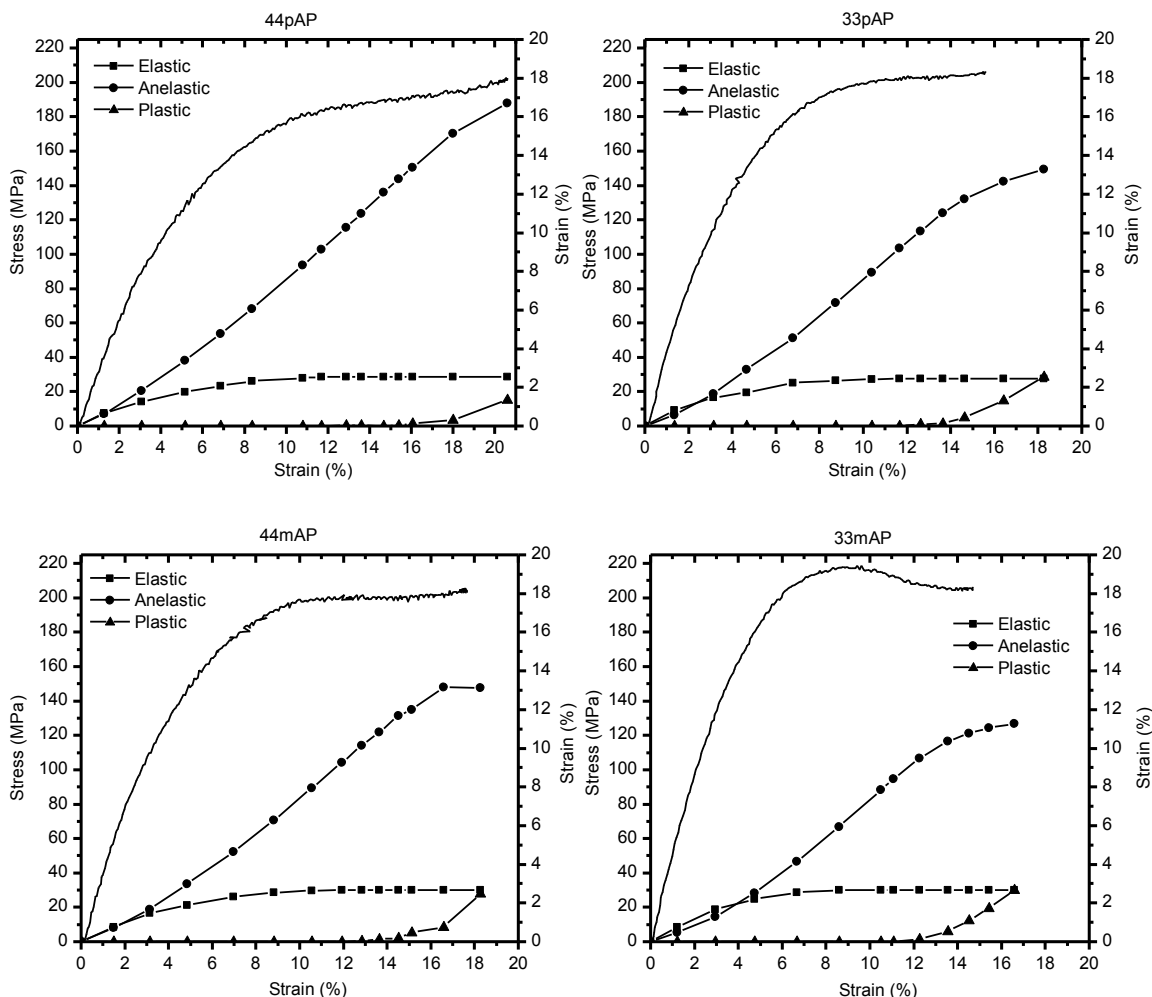
Figure 79. Strain component plots for aminophenol isomer networks.

The component plots seen above show the strain development in the four isomer networks. Elastic and anelastic strain developed simultaneously, followed by the development of plastic strain post-yield. While elastic and anelastic strain developed simultaneously in all networks, the initial rates of development differed with anelastic strain developing the quickest in the fully para-substituted 44pAP system and the slowest in the fully meta-substituted 33mAP system. Alternatively, elastic strain developed the slowest in 44pAP and quickest in 33mAP. Comparison of the 44mAP and 33pAP systems reveals that anelastic strain developed at a quicker rate in the 44mAP network.

The more rapid development of anelastic strain in this network implies that the mobility induced by the para-substituted 4,4'-DDS has a greater affect on anelastic strain development than para-substituted TGAP. The difference in behavior can be related to the two para-substituted rings of 4,4'-DDS compared to one of the p-TGAP.

It was illustrated in Chapter IV that direct comparisons of strain recovery in network isomers can be made by plotting the strain component plots as a fraction of the yield strain of the individual network. Comparison by this manner showed that differences in network deformation behavior were primarily controlled by the development of anelastic strain. In order to conduct the same analysis on the four networks discussed in this chapter, an accurate yield strain had to be determined for each network. In the stress-strain curves (Figure 71), only the 33mAP network showed a clear yield point. Therefore, yield points for the four isomer networks were determined by extrapolation of a best-fit line of the 150°C residual strain data to the x-axis. The point at which this line intersected with the x-axis was defined as the network yield strain. This method has previously been employed for the determination of yield points of polymers.[10,19] The extrapolated yield points, along with the slopes of the fitted lines can be seen in Table 21. The extrapolated yield points refer to the onset of plastic strain development for the isomer networks, and the slopes of the fitted lines illustrate the rate of plastic strain development. The more rigid networks, those cured with 3,3'-DDS, displayed the lower yield strains while the 4,4'-DDS cured networks displayed the highest. The same trend was realized in the DGEBA cured networks. The rate of plastic strain development was the highest for the 33mAP network and lowest in the all para-substituted 44pAP network.

Table 21. Elevated Temperature Recovery Extrapolated Yield Points

Network	Extrapolated Yield	Slope
44pAP	17.24 %	0.400
33pAP	13.96 %	0.570
44mAP	14.75 %	0.650
33mAP	12.89 %	0.703

The extrapolated yield points were used to plot the strain component curves as a fraction of the yield strain. The resulting component curves showing strain development as a fraction of the yield can be seen for all networks in Figure 80. These curves reveal the same trend that was seen when comparing the isomer networks of 33A and 44A. Elastic and plastic strain components of the isomer networks tracked coordinately with one another while the anelastic strain components differed significantly. Thus, anealstic strain development in network isomers accounts for the deformation differences seen in Figure 71 with the more rigid networks (33pAP and 33mAP) developing less anelastic strain than the 44pAP and 44mAP networks. The higher amount of anelastic strain development in the 4,4'-DDS cured networks indicates that these networks were capable of storing more energy. The 3,3'-DDS cured networks were not capable of storing the same amount of strain due to a hindrance associated with the meta-linkages. The result was the development of more stress in the network, which ultimately lead to earlier yielding to dissipate the increased amount of stress.
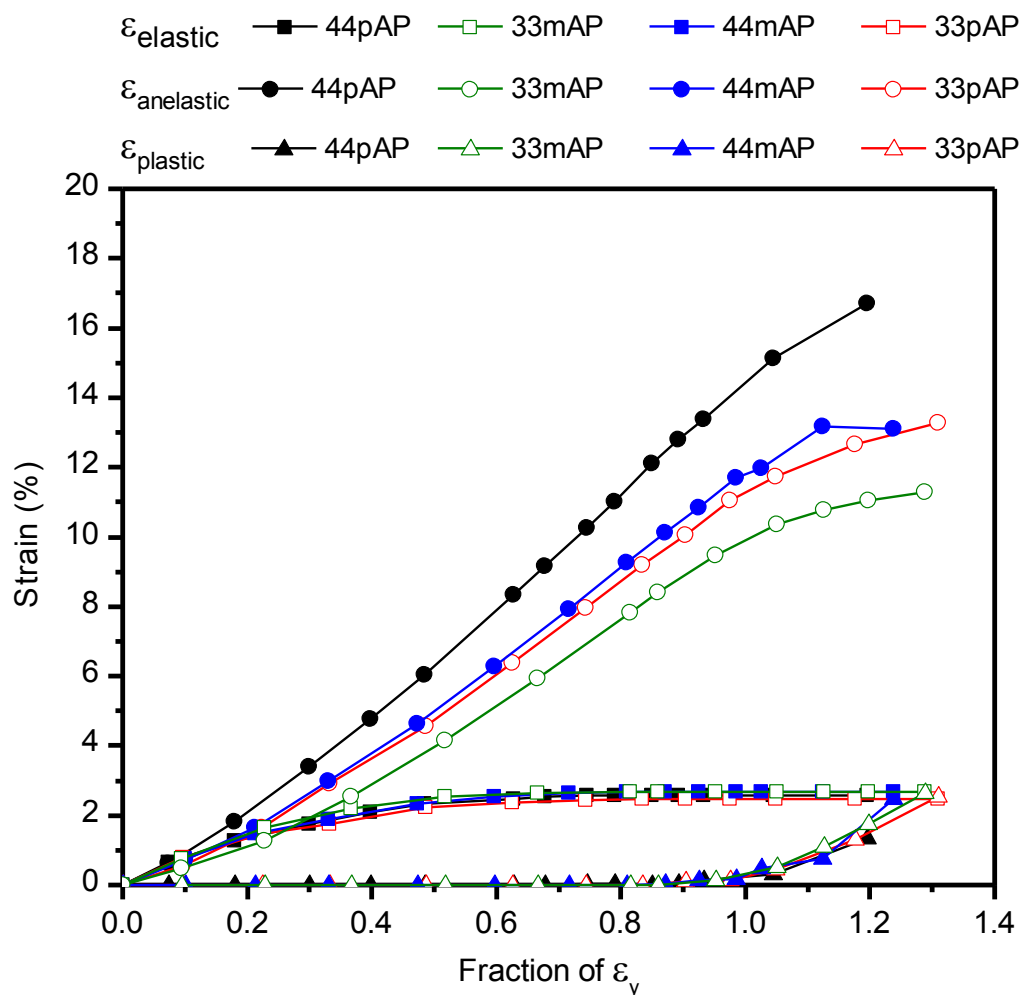
Figure 80. Component curves associated with complete anelastic recovery of the four isomer networks plotted as a function of the yield strain.

The component plots in Figure 80 indicate the importance that anelastic strain plays in the deformation of epoxy network glasses. After complete anelastic recovery it is evident that the delayed yielding seen in the 44pAP system was purely a product of the network's ability to develop more anelastic strain. Anelastic strain in this tightly crosslinked epoxy-amine system developed through the densification of available free volume of the network. Figure 81 shows the average hole size free volume (V_h) for two of the TGAP-DDS systems. The 44mAP system clearly showed a higher V_h over the 33mAP system, indicating that systems cured with 4,4'-DDS possess a larger amount of

frozen in free volume when compared to 3,3'-DDS. This result is consistent with results seen in the 33A and 44A systems discussed in the Chapter IV. Based on the larger V_h of 44mAP, it was assumed that a larger amount of compressible volume existed in the 4,4'-DDS cured networks. More available free volume resulted in a larger amount of stored energy through filling of this available volume through densification of the network. This increased amount of energy storage accounts for the decreased rate of stress development and increased strain at yield in the 4,4,-DDS networks.
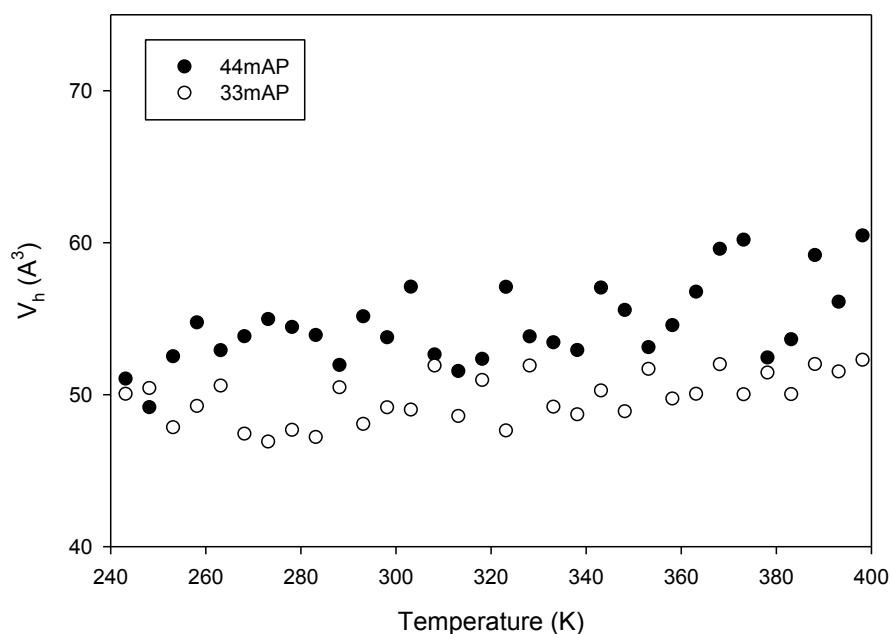
Figure 81. Hole size free volume of trifunctional epoxy systems.

The para-substitution of 4,4'DDS resulted in an increase in the V_h of the final cured network. This increase in free volume is a result of the increase in dynamic volume induced by a higher level of molecular motion in the networks. As shown in Chapter IV, increased cooperative motion is obtained through the ability of the para-substituted amines to rotate along the axis-of-symmetry created by the linearity of the segment. A similar result can be expected of the p-TGAP segments as the molecule displays a clear axis for phenyl ring rotations to occur (Figure 82). Like 3,3'-DDS, the

m-TGAP segments do not display an axis of symmetry. The restriction of phenyl ring rotations in the meta-substituted segments results in ring librations being the only available phenyl ring motion.
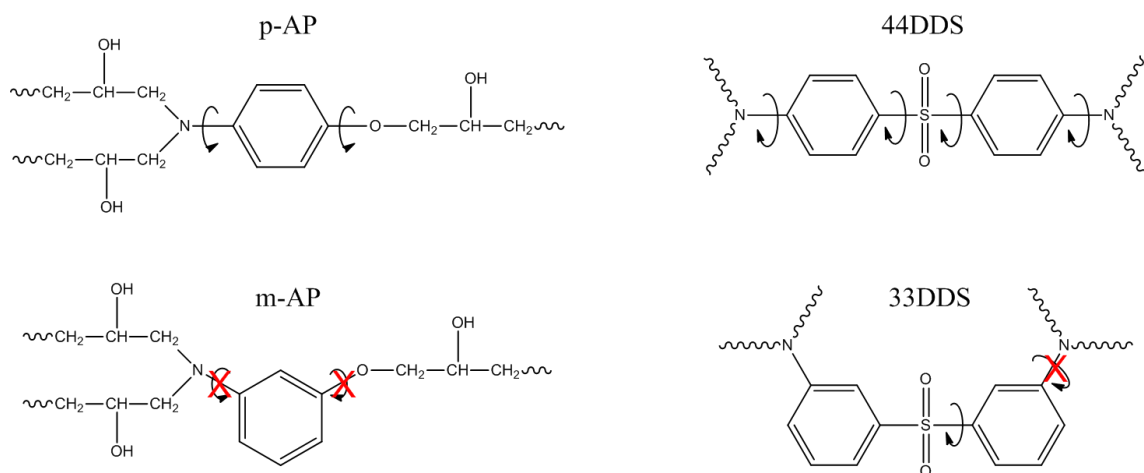
Figure 82. Availability of phenyl ring flips in monomer segments.

The reduced free volume in the meta-substituted systems is a product of the restricted dynamic motions, discussed above, and the more conformations that can be obtained when cooling from the liquid (rubbery) to glassy state. This increased conformation ability for 3,3'-DDS was discussed in Chapter IV as a cis- or trans-configuration of the amine substitution can be obtained, resulting in a tighter packing density. The m-TGAP epoxy also possesses an increased packing ability as the directionality of the kink can change depending on the orientation of the phenyl ring with respect to neighboring chain segments. The combination of meta-substitutions of the amine and epoxy resulted in the lowest free volume and highest rigidity displayed by the 33mAP system, as it is not able to store as much energy through anelastic strain.

While discussing the different available motions in the glassy state, it is important to revisit the DMA Tan δ curves. The β-transition, seen from $^{-}120$-$^{+}50^{o}$C, was identical on the low temperature side for all four networks with the high temperature side of the

peak only differing in the 44pAP network. Recall that the 4,4'-DDS cured networks do not go to complete conversion as indicated by the DSC traces seen in Figure 73. Residual functionality within the network results in an increase in the molecular weight between crosslinks of the cured network. M_c was calculated from DMA rubbery modulus values and was shown in Table 16. Variances in M_c were associated with different cure extents arising from varying reactivity, vitrification points, and steric hindrances of the networks. The 44pAP network displayed the lowest calculated M_c, suggesting the lowest overall conversion and highest residual functionality. The residual functionality played a major role in the increased molecular mobility indicated by the DMA sub-T_g transition and strain component plots. However, variances of M_c appeared in the other 3 networks as well but did not result in a change in the breadth or magnitude of this transition. This discrepancy in behavior suggests that some other variance in cooperative motions existed in the 44pAP network.

Figure 83 illustrates the effect that incomplete cure will have on molecular structure of the cured network where residual epoxy monomers will create dangling chain ends and residual secondary amine will create longer linear segments between junction points. The 44pAP network possess the ability for more cooperative motion due to the linearity of the under cured segments. All networks contained some residual functionality, which varied from network to network as shown by the calculated M_c values. However, the β-transition for the 33pAP, 44mAP, and 33mAP networks were almost identical, indicating that residual functionality within these networks did not create a measureable difference in mobility. The 44pAP network displayed a clear difference in β-transition with a broader, bimodal peak. The additional breadth was associated with the increased cooperative capabilities of undercured segments in the all

para-substituted network. The highest M_c value of this network suggests even more

cooperative nature as the presence of consecutive groups containing residual functionality

creates even longer linear segments for cooperative motion to occur. The net result was a

more labile network that was capable of storing more energy and thereby resisting the

onset of yield.
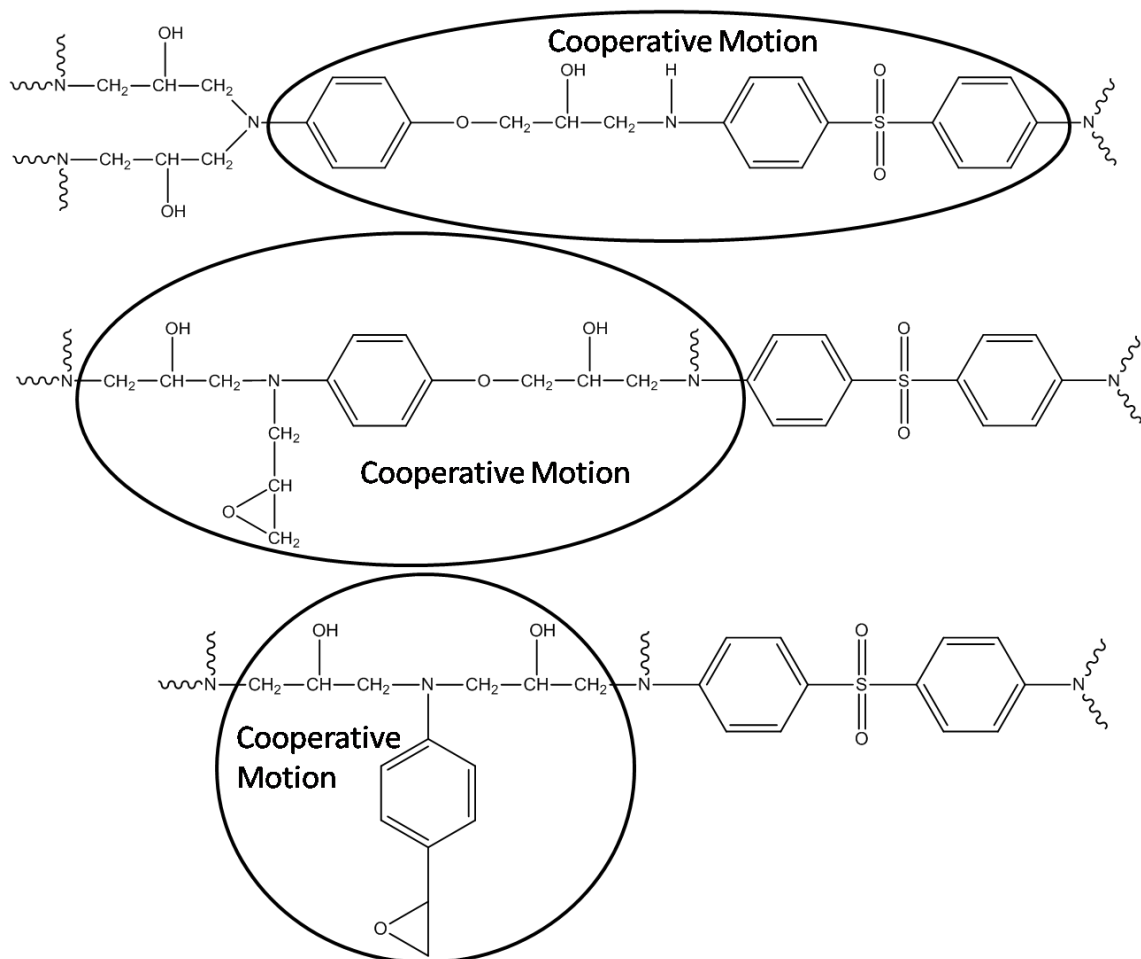
Figure 83. Availability of cooperative motion from undercuring within networks.

Post-yield behavior. The fully para-substituted epoxy network displayed an

increased ability to store energy through anelastic strain prior to yield. However, the all

meta-substituted network displayed an increased amount of stress dissipation post-yield.

The increased energy dissipation is indicated by the strain softening seen in the stress-

strain curves of Figure 71. At yield, large segmental rearrangements occur within the

network in order to dissipate stress. The meta-substituted rings, while unable to rotate pre-yield, are now capable of flipping in large scale network rearrangements. Figure 84 shows the capable rearrangements, which occur as a product of large α-type motions within the network by conversion of the 3,3'-DDS segment from cis- to trans-configuration (or vice-versa) or by flipping of the meta-substituted aminophenol. These α-type motions are a product of segmental flow and are not available in this form in the para-substituted counterparts, providing an explanation as to why the 44pAP system displayed no strain softening while the 33mAP system displayed a significant amount. The 44mAP and 33pAP network displayed very similar stress-strain behaviors. However, upon close examination it appears that the 44mAP network displayed a small amount of strain softening while the 33pAP network did not. This would indicate that the rearrangement associated with the flipping of the meta-substituted aminophenol segment dissipates more energy than the configuration change of the 3,3'-DDS segment.
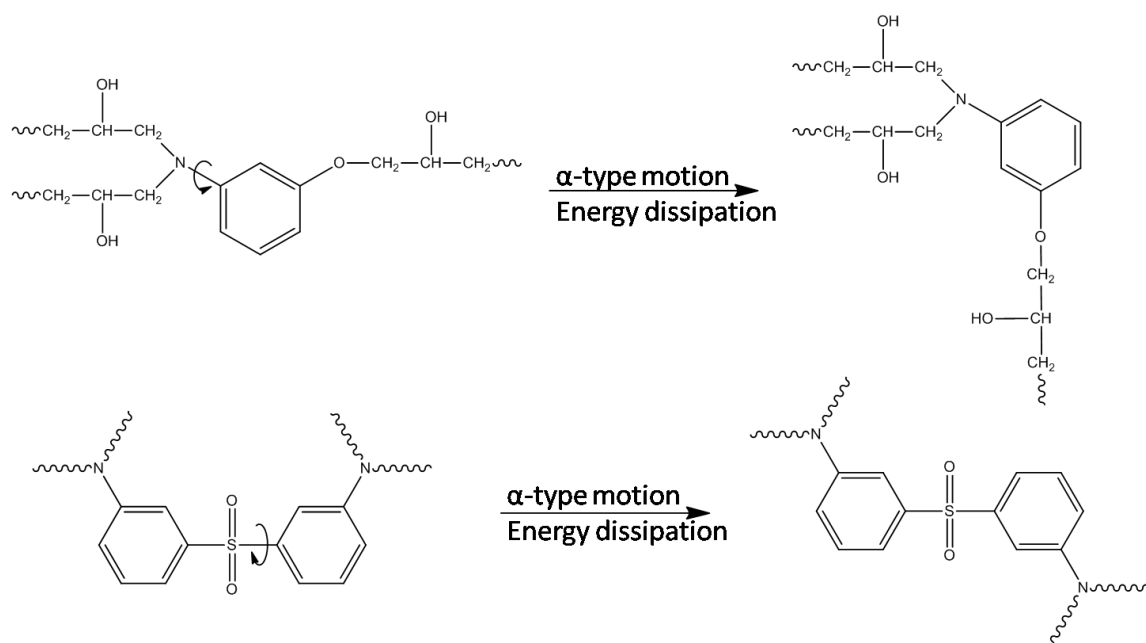
Figure 84. α-type motions of meta-substituted network segments.

Comparisons to Linear Epoxies

The deformation differences associated with network isomerism have been explained thoroughly. However, comparisons of the TGAP based networks to the results of DGEBA networks have not been fully explored. Figure 85 shows a comparison of the stress-strain behavior of the TGAP based and DGEBA based networks. The most glaring difference is the increased magnitude of stress achieved in the tighter bound TGAP networks prior to yielding. The TGAP based networks (with the exception of 44pAP) possess a significantly higher modulus, yield stress, and yield strain values to the DGEBA networks. Table 22 provides a numerical comparison of network properties.
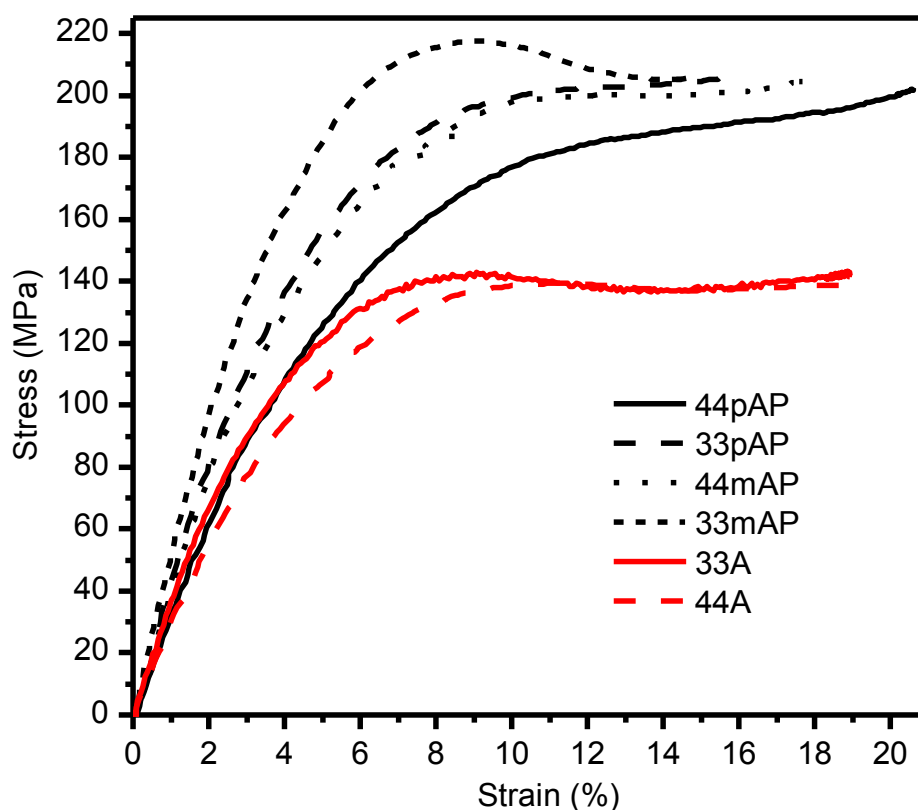
Figure 85. Comparison of stress-strain behavior of aminophenol-based networks to those based on DGEBA.

Table 22. Comparison of DGEBA and TGAP Networks

	Modulus (MPa)	Yield Stress (MPa)	Yield Strain (%)	Density (g/ml)	$M_{c, exp}$ (g)
33A	3914	142.2	9.07	1.237	394.1
44A	3691	139.7	11.51	1.239	297.3
44pAP	3385	~190	17.24	1.3196	680.1
44mAP	4369	~200	14.75	1.3250	364.6
33pAP	4977	~203	13.96	1.3288	328.2
33mAP	5540	217.5	12.89	1.3242	420.0

The increased modulus in three of the TGAP networks is associated with the tighter chain packing as indicated by the higher density and lower free volume of these networks. The decreased modulus of the 44pAP network compared to 44A network is attributed to the increased M_c value of 44pAP relative to the other TGAP networks and the increased cooperative motions from the all para-substitution. Theoretically, this network should have a higher crosslink density. However, for various reasons (rapid vitrification, decreases reactivity, increased steric hindrance due to linearity of structural units) discussed previously, the M_c did not approach its theoretical value resulting in a looser bound network with a large amount of cooperative motions. The achievement of higher stress and yield strain values in the TGAP networks is attributed to their decreased linear nature. The linear DGEBA segments require less stress to induce large segmental flow within the network.

Analysis of the post-yield behavior provides insights into the segmental flow capabilities of the networks. For the linear based DGEBA networks, once segmental flow began large strain localization was seen within the yielded region of the cylinder. Figure 86 shows a strain map and plot displaying strain along the y-axis with increasing time for the 44pAP network at ~21% total strain. Recall from Chapter V, the 33A

network displayed a large amount of strain localization while the EW540-33 network

contained even more. The results shown in Figure 86 reveal only a small amount of

strain localization for the all para-substituted TGAP based network, indicated by no

prevalent shear banding on the specimen surface, a low gradient of strain along the y-

axis, and the smaller distribution of strains shown by the histogram connected to the

specimen legend. This strain localization behavior, or lack thereof, indicates that the

TGAP based networks are not capable of undergoing the same degree of local flow as the

DGEBA based networks.
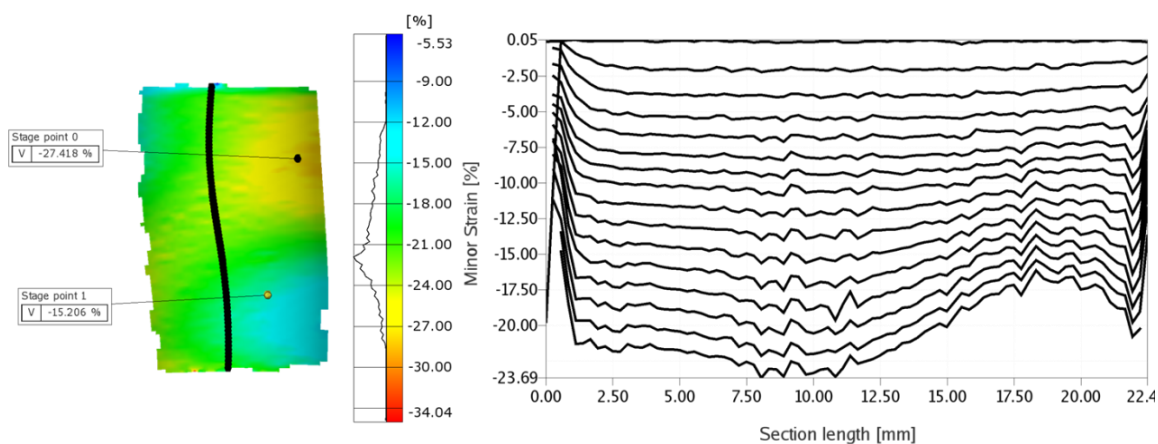
Figure 86. Strain localization in the 44pAP network.

The 44pAP network results seen in Figure 86 are for the TGAP network that

displayed no strain softening. Figure 87 shows the same information for the 33mAP

network, which showed a significant amount of strain softening. Relative to the 44pAP

network, the 33mAP network showed a more prominent shear band and a slightly larger

amount of strain localization. However, the degree of localization was still significantly

less than what was seen in the DGEBA based networks.
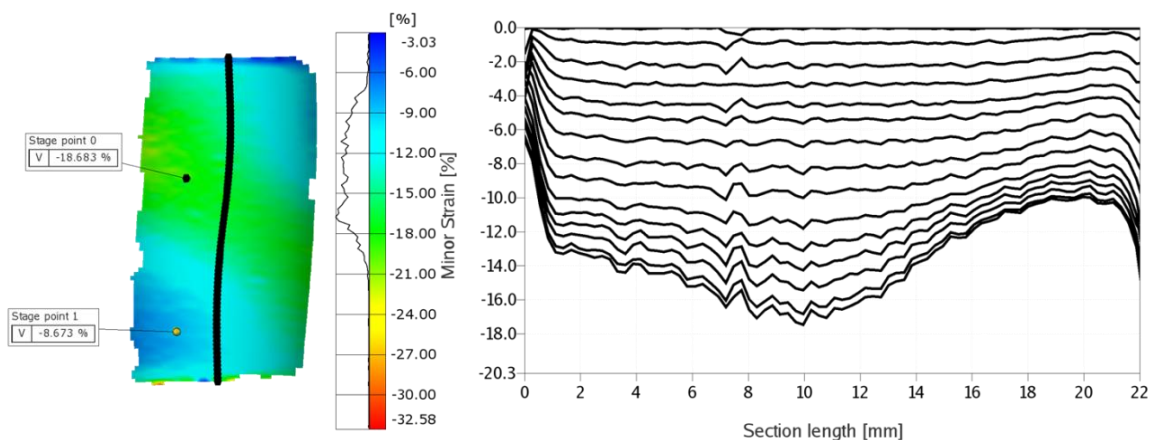
Figure 87. Strain localization in the 33mAP network.

The degree of strain localization is indicative of the segmental flow characteristics of the crosslinked networks. The TGAP networks displayed average M_c values with comparable values to that of the DGEBA networks. However, as described earlier, the experimental M_c values are likely a representation of the weakest domain and not a true representation of the average. The segmental flow behavior can be better explained by the theoretical M_c values, which are significantly lower for the TGAP networks suggesting less segmental mobility. Yield occurs when the stress on the network reaches a critical value to cause large segmental rearrangements within the weakest domain of the network. Once a region yields, flow continues in this region until the chains have been extended to their maximum length; after which, neighboring regions (already strained to near their anelastic capacity) yield, allowing for more flow. Yield progresses in this manner until all chains become fully extended and until subsequent energy placed on the system induces bond breakage and macro scale fracture. The ability of the DGEBA networks to experience large strain localization is due to the decreased frequency of junction points. Figure 88 shows structural units for the TGAP and DGEBA networks where linear segments are highlighted in green and junctions are noted in red. It is evident that the larger linear segments of the DGEBA based networks allow for more

segmental flow, especially in networks containing higher degrees of polymerization (EW540).
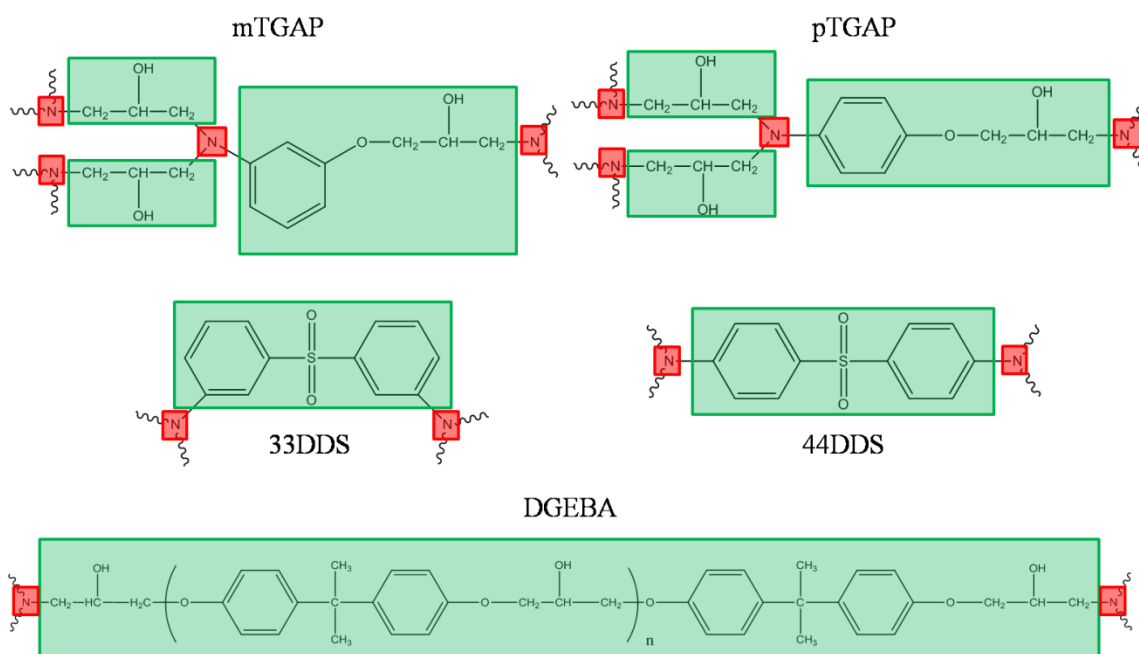
Figure 88. Comparison of mobile sections of structural units.

The above comparison of DGEBA and TGAP network behavior reveals the TGAP networks to possess a greater rigidity and stress bearing capacity due to increased packing density and crosslink density. The TGAP networks were capable of achieving larger amounts of stress and strain prior to yield, indicating an ability to store more energy through anelastic strain. Post-yield the TGAP networks displayed a less localized flow due to increased frequency of junction points, creating a more tightly bound network.

Conclusions

Chapter VI extended the study of isomerism to include the affects of isomerism within the epoxy resin by the use of para- and meta-substituted triglycidyl aminophenol epoxies. The results again indicated that para-substitution leads to a higher level of

energy storage due to increased sub-T_g molecular motion and increased free volume. The all para-substituted 44pAP network displayed the lowest modulus, lowest yield stress, and highest yield strain due to its ability to store energy through cooperative motions within the all para-substituted network, particularly in regions where residual functionality remained. The all meta-substituted 33mAP network displayed more rigid behavior due to the lack of cooperativity within the network, which resulted in decreased energy storage and earlier yield. However, post-yield the meta-substitution provided a pathway for increased energy dissipation through segmental rearrangements associated with cis- to trans- (or vice-versa) conformational change of the DDS curative or segmental flips from the meta-substituted TGAP. The result of these motions was increased strain softening and a slight increase in strain localization compared to the all para-network.

The use of the trifunctional epoxy also allowed for the comparison of a tightly crosslinked network with the looser bound DGEBA based networks of Chapters IV and V. Resulting comparisons revealed that TGAP based networks displayed a higher yield stress and strain due to their increased ability to resist large segmental flow. This resistance arises from the increased rigidity and tighter crosslink density of the networks. Post-yield the TGAP networks displayed decreased strain localization due to an increase in junction points and decreased linear segments. The result was a more uniformly deformed network that would ultimately reach failure prior to the DGEBA-based networks due to the inability to dissipate further applied stress.

References

1. Lin, Q.; Yee, A.F.; Sue, H.J.; Earls, J.D.; Hefner Jr, R.E. *J. Polym. Sci. Polym. Phys.* **1997,** *35*, 2363.
2. Ashok, L.C. *Macromolecules* **1984,** *17,* 11.
3. Chang, T.D.; Carr, S.H.; Brittain, J.O. *Polym. Eng. Sci.* **1982,** *22,* 1205.
4. Starkweather, H.W.J. *Polymer* **1991**, *32,* 2443.
5. Starkweather. H.W.J. *Macromolecules* **1990**, *23,* 328.
6. Ragosta, G.; Musto, P.; Abbate, M.; Scarinzi. G. *Polymer* **2009,** *50,* 5518-5532.
7. Becker, O.; Varley, R.; Simon, G. *Polymer* **2002,** *43,* 4365-4373.
8. Laupretre, F.; Eustache, R.P.; Monnerie, L. *Polymer* **1995,** *36*, 267-274.
9. Yurenko, N.A.; Yevtushenko, G.T.; Yermilova, Y.Y.; Shologon, I.M.; Rozenberg, B.A. *Polymer Science USSR* **1984,** *26,* 2867-2872.
10. Quinson, R; Perez, J; Rink, M; Pavan, A. *J. Mater. Sci.* **1996,** *31,* 4387-4394.
11. David, L.; Quinson, R.; Gauthier, C.; Perez, J. *Polym. Eng. Sci.* **1997,** *37,* 1633-1640.
12. Oleinik, E.F.; Rudnev, S.N.; Salamatina, O.B.; Shenogin, S.V.; Kotelyanskii, M.I.; Paramzina, T.V.; Nazarenko, S.I. *e-Polymers* **2006** no. 029.
13. Kawakami, H.; Yamanaka, H.; Nanzai, Y. *Polymer* **2005,** *46*, 11806-11813.
14. Oleynik, E. *Prog. Coll. Pol. Sci. S.* **1989,** *80,* 140-150.
15. Pegoretti, A.; Pandini, S.; Ricco, T. *Polymer* **2006,** *47,* 5862-5870.
16. Ricco, T.; Pegoretti, A. *J.Polym. Sci. Pol. Phys.* **2002,** *40,* 236-243.
17. Pegoretti, A.; Guardini, A.; Migliaresi, C.; Ricco, T. *Polymer* **2000,** *41,* 1857-1864.
18. Rinaldi, R.; Gaertner, R.; Chazeau, L.; Gauthier, C. *Int. J. Nonlin. Mech.* **2011,** *46,* 496-506.
19. Rose, J.; Duckett, R.A.; Ward, I.M. *J. Mater. Sci.* **1995,** *30,* 5328-5334.

CHAPTER VII

CONCLUSIONS AND FUTURE CONSIDERATIONS

The overall goal of this research was to further develop relationships between epoxy network structure and macro-scale performance. This dissertation presented the findings on the subject, focusing on the strain development in epoxy networks and relating variances in behavior to differences in molecular motions within the network. The purpose of this chapter is to review the findings divulged in this document and draw conclusions to how these findings further the understanding of the role the epoxy matrix in composite deformation and failure.

Summary of Results

The specific findings of this research were presented in the previous chapters with the following goals:

1. Introduce the digital image correlation techniques developed to study the strain behaviors of composite matrices under load.

2. Reveal findings of structural isomerism on mechanical properties and deformation of DGEBA based epoxies cured with 3,3'- or 4,4'-diamnodiphenyl sulfone.

3. Investigate the influence of matrix crosslink density and isomerism on mechanical properties and deformation through use of higher equivalent weight DGEBA resins cured with either 3,3'- or 4,4'-diamnodiphenyl sulfone.

4. Further study the influence of network isomerism on matrix deformation capability through the investigation of high crosslink density networks based on triglycidyl ether of meta- or para-aminophenol cured with 3,3'- or 4,4'-diaminodiphenyl sulfone.

Chapter III presented in detail the digital image correlation techniques used to study uniaxial deformation properties of glassy polymer networks. DIC methods were a vital part of this research as they provided a different perspective of mechanical deformation analysis. DIC provided a non-contact technique that was simple to use and advantageous to generate accurate/reproducible data for analyzing compression and tensile moduli, Poisson's ratio, and yield strain. Techniques provided a substantial increase in accuracy for measuring strain compared to LVDT and also allowed for simultaneous longitudinal and transverse strain measurements to calculate Poisson's ratio. DIC was particularly sensitive for measuring small strain compression modulus. An accurate yield strain was obtained using DIC, which clearly eliminated erroneous strain data associated with fixture and equipment compliance.

DIC techniques were also developed for studying the pre-yield, yield and post-yield behavior of glassy polymer solids. DIC was used to measure compressive strain recovery of epoxy glasses in order to provide useful insights into the deformation analysis of the epoxy networks by illustrating clear strain localization prior to macroscopic yielding. This strain localization was present in the center of the cylindrical specimens once the total strain of the test extended beyond the linear viscoelastic strain region. Strain localization was due to the development of anelastic strain in the form of shear micro domains, which eventually coalesce to create macroscopic yielding. The

developed methods were essential in the comparison of differing epoxy networks in subsequent chapters.

In Chapter IV, the viscoelastic deformation of DGEBA based isomers was compared using the DIC strain recovery procedures. The isomer networks of low molecular weight DGEBA cured with 3,3'-DDS or 4,4'-DDS displayed different mechanical performance while being identical in chemical composition. Comparisons of strain development in the isomer networks revealed similar elastic and plastic strain behavior but differing anelastic strain behavior. The similar elastic behavior was due to the common molecular interactions of the chemically identical networks. Likewise, the plastic behavior was the same due to identical chemical composition. Plastic strain occurs by α-type motions, or viscoplastic flow, removing any conformational effects from the different isomers. This left the discrepancy in strain behavior to be accounted for by anelastic strain. The 44A system developed anelastic strain at a significantly higher rate prior to yield as it was able to undergo more molecular motions as indicated by DMA tan δ curves of the two systems. The increased molecular mobility of the 44A network arises from the increased para-substitution and the availability of an axis for phenyl-ring rotations in the 4,4'-DDS segments. The 33A network does not possess this axis of symmetry, displaying less energy storage capabilities. However, the 33A network did show increased energy dissipation post-yield due to segmental rearrangements associated with the 3,3'-DDS curative.

Further investigation of structure-property relationships of glassy polymer networks was presented in Chapter V through varying the equivalent weight of the DGEBA based epoxy network isomers. Compression experiments conducted on cylindrical specimens showed a clear step-down in the stress and strain at yield with

increasing epoxy equivalent weight for both 3,3'- and 4,4-DDS cured networks. The decrease in yield values was attributed to an increase in molecular weight between crosslinks, which created more cooperative glassy state mobility as seen in dynamic mechanical analysis. DMA Tan δ curves showed a decrease in temperature of the α-transition with increasing M_c, indicating the requirement of less energy to induce α-motions. A decrease in temperature was also seen for the β- transitions, along with an increase in area of the peaks, revealing the availability of more cooperative motions along the increased linear segments.

Additional analysis of network isomers revealed that increased DGEBA EW decreased the effect that curative isomer structure had on deformation. The EW540 isomers showed nearly identical stress-strain behavior with similar modulus, yield stress, and yield strain values. This behavior illustrated that deformation became controlled primarily by the long, linear DGEBA segments within the network. These segments have a decreased resistance to flow, indicated by the low yield stress, and are the primary component of the network as the maintenance of stoichiometric ratios decreased the overall amine segment concentration.

Strain recovery experiments were used to investigate strain development in the EW540 networks. These results showed an earlier onset and a more rapid development of plastic strain when compared to the EW175 networks discussed in Chapter IV. The increased rate of plastic strain development was accompanied with a decrease in anelastic strain post-yield. These differences in strain development were attributed to increased strain localization due to an increased molecular weight between crosslinks. More cooperative motions were available in the EW540 networks resulting in a lower resistance to yield. Once yield began, significant strain softening occurred as the stress

required to continue flow in the yielded region was lower than the stress required to initiate local flow.

Chapter VI extended the study of isomerism to include the effects of isomerism within the epoxy resin by the use of para- and meta-substituted triglycidyl aminophenol epoxies. The results again indicated that para-substitution leads to a higher level of energy storage due to increased sub-T_g molecular motion and increased free volume. The all para-substituted 44pAP network displayed the lowest modulus, lowest yield stress, and highest yield strain due to its ability to store energy through cooperative motions within the all para-substituted network, particularly in regions where residual functionality remained. The all meta-substituted 33mAP network displayed more rigid behavior due to the lack of cooperativity within the network, which resulted in decreased energy storage and earlier yield. However, post-yield the meta-substitution provided a pathway for increased energy dissipation through segmental rearrangements associated with cis- to trans- (or vice-versa) conformational change of the DDS curative or segmental flips from the meta-substituted TGAP. The result of these motions was increased strain softening and a slight increase in strain localization compared to the all para-network.

The use of the trifunctional epoxy also allowed for the comparison of a tightly crosslinked network with the looser bound DGEBA based networks of Chapters IV and V. Resulting comparisons revealed that TGAP based networks displayed a higher yield stress and strain due to their increased ability to resist large segmental flow. This resistance arises from the increased rigidity and tighter crosslink density of the networks. Post-yield the TGAP networks displayed decreased strain localization due to an increase in junction points and decreased linear segments. The result was a more uniformly

deformed network that would ultimately reach failure prior to the DGEBA based networks due to the inability to dissipate further applied stress.

Overall findings in this research revealed network isomerism to play an important role in deformation of epoxy network glasses. Networks containing meta-substituted monomers possessed higher modulus and yield stress values and lower yield strains. On the contrary, networks with para-substituted monomers displayed lower modulus and yield stress values, but increased ability to store energy through anelastic strain mechanisms, thereby, delaying the onset of yielding. The increased energy storage of these networks was related to sub-Tg molecular motions and the ability for para-substituted phenyl rings to rotate along an axis of symmetry creating more cooperative motion within the network. Insights into post-yield deformation of epoxy glasses were also gained where networks with meta-substitution were able to dissipate more stress post-yield through large segmental rearrangements. Crosslink density also played an important role on the influence of network isomerism. Higher crosslink density networks, such as those composed of TGAP/DDS, were influenced more by network isomerism. As crosslink density decreased, the effects of isomerism also decreased with network isomers composed of high molecular weight DGEBA showing little to no difference in deformation behavior.

<center>Relation to Composite Performance</center>

The findings of this research have led to a better understanding of the molecular mechanisms associated with neat epoxy network deformation. However, conclusions as to how these deformations characteristics affect composite performance have not been discussed. The complexity of composite deformation and failure was reviewed in the introduction in which the multi-axial stress state of the composite matrix was discussed.

The orientation of the fibers within the composite play an important role in determining how the polymer matrix will deform when loaded. Tests used to determine the critical dilational and distortional strain invariants discussed in the introduction are tensile tests of unidirectional composites of 90˚ and 10˚ off-axis fiber orientation. Figure 89 depicts these coupon tests alongside the polymer failure envelope. In the 90˚ coupon the stiffness of the fibers creates a biaxial stress state on the polymer matrix resulting in deformation by volume expansion, resulting in rapid cavitation and brittle failure. Deformation in the 90˚ coupon is of mode I type in the failure envelope where failure occurs the quickest. In the 10˚ coupon, the fibers act to re-orient the axial stress to induce a deviatoric loading where deformation occurs primarily through shear or distortional mechanisms. Both of these tests induce failure within the polymer matrix.
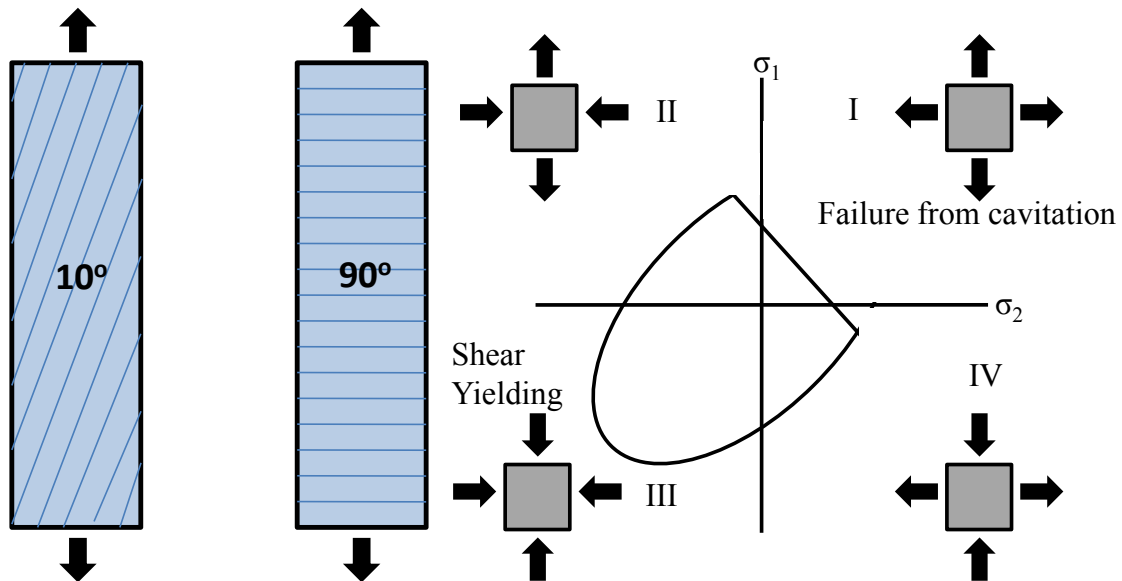
Figure 89. Tests used for determination of critical strain invariants.

The insights gained from network deformation characteristics established in this research can be used to theorize how network mobility will influence performance in these composite applications. Failure in a 90˚ coupon is primarily controlled by the

intermolecular cohesion between network chain segments. Networks that possess a high

amount of intermolecular forces will display a larger resistance to deformation in this

mode (i.e., will develop more stress). Of the networks discussed in this research, the high

crosslink density networks composed of TGAP possess the largest amount of

intermolecular cohesion as illustrated by their high modulus and high-yield stress.

However, once the intermolecular interactions are overcome, failure will occur rapidly as

the matrix will be unable to deform in a dilational manner due to the low molecular

weight between crosslinks of these networks. Alternatively the DGEBA based networks

will not possess the same amount of resistance to dilational deformation but will be able

to undergo more volume expansion prior to failure due to the linear DGEBA segments

(particularly in the higher EW networks).

The 10° coupon creates a more complex deformation scenario. The

deviatoric/shear type loading allows for increased strain prior to failure where

intramolecular interactions play an important role in this deformation process.

The strain recovery experiments conducted in this research provide insights into how

these matrices will deform in this scenario. For rigid networks, increased anelastic strain

capabilities will allow for more energy storage within the matrix and will delay failure.

Isomer networks with increased para-substitution displayed the ability to undergo more

anelastic strain, suggesting increased deformation in 10° coupon tests. However, ultimate

failure in these coupons still occurs in a brittle fashion, indicating that the ability to resist

brittle failure will delay this catastrophic event. In the introduction, matrix yield was

described as a method of offsetting composite failure as a means to dissipate stress. The

EW540 networks possess a low yield point and a large amount of strain softening post-

yield due to the ability to localize strain. In a 10˚ coupon this resin would likely have an increased resistance to dilational failure due to the ability to yield and deform plastically.

Future Research Considerations

Future research should seek to further develop the relationships between neat matrix performance and ultimate composite performance. The Wiggins Research Group has recently acquired the capabilities to produce aerospace quality unidirectional pre-preg materials. This capability will allow for further advancement of multi-scale research by allowing for production of unidirectional composites from select resin systems. The composite properties can then be compared to neat resin deformation characteristics learned by the techniques developed and presented in this dissertation. Figure 90 shows preliminary digital image correlation analysis of a 10˚ off-axis composite coupon, illustrating local strain development along the fibers that pass through the centroid of the test coupon. DIC will provide the ability to compare strain development within the composite coupons to strain development in neat resin.
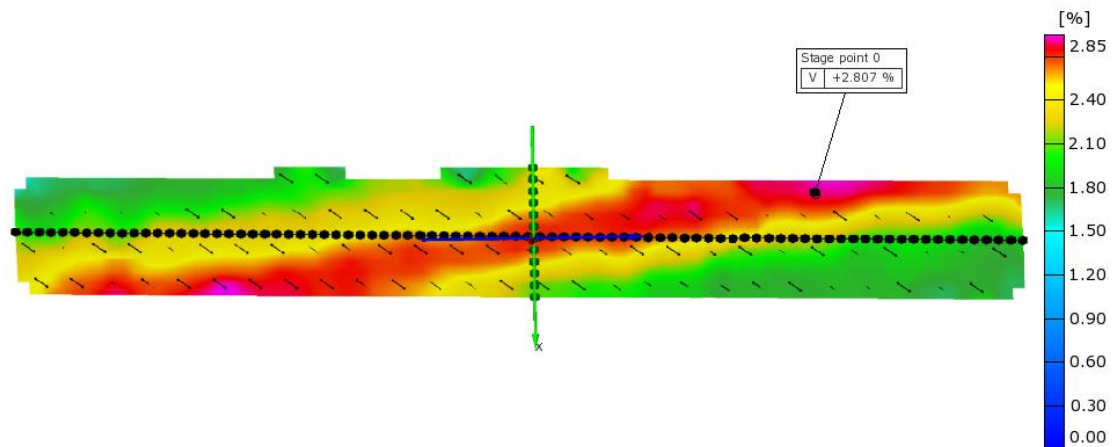
Figure 90. DIC analysis of 10˚ off-axis unidirectional composite coupon.

Further insights into strain development and failure in composite materials will lead to a better connection between molecular structure and macroscopic deformation.

These multi-scale relationships will ultimately lead to improved design criteria for composite materials, drastically reducing the time and cost for implementing new polymeric systems into composite structures.